2024-03

DEVELOPMENT OF A SMALL, SPACE-BASED TERAHERTZ-TO-INFRARED IMAGING SYSTEM

Stank, Matthew J.

Monterey, CA; Naval Postgraduate School

https://hdl.handle.net/10945/72765

NAVAL POSTGRADUATE SCHOOL

MONTEREY, CALIFORNIA

THESIS

DEVELOPMENT OF A SMALL, SPACE-BASED TERAHERTZ-TO-INFRARED IMAGING SYSTEM

by

Matthew J. Stank

March 2024

Thesis Advisor:	Fabio Durante Pereira Alves
Co-Advisor:	Wenschel D. Lan

THIS PAGE INTENTIONALLY LEFT BLANK

REPORT DOCUMENTATION PAGE

Form Approved OMB No. 0704–0188

1. AGENCY USE ONLY ***(Leave blank)***	**2. REPORT DATE** March 2024	**3. REPORT TYPE AND DATES COVERED** Master's thesis

4. TITLE AND SUBTITLE DEVELOPMENT OF A SMALL, SPACE-BASED TERAHERTZ-TO-INFRARED IMAGING SYSTEM	**5. FUNDING NUMBERS**
6. AUTHOR(S) Matthew J. Stank	
7. PERFORMING ORGANIZATION NAME(S) AND ADDRESS(ES) Naval Postgraduate School Monterey, CA 93943-5000	**8. PERFORMING ORGANIZATION REPORT NUMBER**
9. SPONSORING / MONITORING AGENCY NAME(S) AND ADDRESS(ES) N/A	**10. SPONSORING / MONITORING AGENCY REPORT NUMBER**

11. SUPPLEMENTARY NOTES The views expressed in this thesis are those of the author and do not reflect the official policy or position of the Department of Defense or the U.S. Government.

12a. DISTRIBUTION / AVAILABILITY STATEMENT Approved for public release. Distribution is unlimited.	**12b. DISTRIBUTION CODE** A

13. ABSTRACT (maximum 200 words)

Direct imaging of terahertz (THz) radiation has useful applications in space-based remote sensing of the upper ionosphere. Researchers at the Naval Postgraduate School have developed a terahertz-to-infrared band-converting metamaterial focal plane array (FPA) using micro-electromechanical systems (MEMS) fabrication techniques. The FPA is designed to absorb selective narrowband THz radiation at 2.06 THz and 4.75 THz, associated with atomic oxygen electron transitions, and convert it to long-wave infrared radiation (LWIR). The emitted LWIR can then be imaged by an uncooled microbolometer infrared camera. This effectively converts the THz emitting scene into an IR image that can be directly interpreted. In order for this technology to be tested in space, an optical system was designed, tested, and built to effectively utilize the band-converting capability of the FPA. The form factor of the resulting optical system, called the Terahertz Imaging Camera (TIC), is compatible with standard 6U CubeSat bus size, weight, and power requirements. The system is divided into two distinct sections, independent of each other due to separation by the FPA. The THz section focuses distant THz radiation onto the FPA via a 90°-fold parabolic mirror, while the IR section focuses the backside of the FPA onto the LWIR camera for imaging via two Ge meniscus lenses. The sensitivity of the system was found to be 1.0 K/µW, which translates to a 50 nW minimum detectable power by the LWIR camera.

14. SUBJECT TERMS terahertz, THz, infrared, IR, TIC, remote sensing, atomic oxygen, COTS, ozone, microbolometer, cubesat, smallsat, ionosphere, micro-electromechanical, MEMS, FPA, focal plane array, 2.06 THz, 4.75 THz	**15. NUMBER OF PAGES** 119
	16. PRICE CODE

17. SECURITY CLASSIFICATION OF REPORT Unclassified	**18. SECURITY CLASSIFICATION OF THIS PAGE** Unclassified	**19. SECURITY CLASSIFICATION OF ABSTRACT** Unclassified	**20. LIMITATION OF ABSTRACT** UU

NSN 7540–01-280-5500

Standard Form 298 (Rev. 2–89)
Prescribed by ANSI Std. 239–18

THIS PAGE INTENTIONALLY LEFT BLANK

DEVELOPMENT OF A SMALL, SPACE-BASED TERAHERTZ-TO-INFRARED IMAGING SYSTEM

Matthew J. Stank
Major, United States Air Force
BS, University of Hawai'i, Manoa, 2009
MS, Embry-Riddle Aeronautical University, Worldwide, 2017

Submitted in partial fulfillment of the
requirements for the degree of

MASTER OF SCIENCE IN SPACE SYSTEMS OPERATIONS

from the

NAVAL POSTGRADUATE SCHOOL
March 2024

Approved by: Fabio Durante Pereira Alves
Advisor

Wenschel D. Lan
Co-Advisor

James H. Newman
Chair, Space Systems Academic Group

THIS PAGE INTENTIONALLY LEFT BLANK

ABSTRACT

Direct imaging of terahertz (THz) radiation has useful applications in space-based remote sensing of the upper ionosphere. Researchers at the Naval Postgraduate School have developed a terahertz-to-infrared band-converting metamaterial focal plane array (FPA) using micro-electromechanical systems (MEMS) fabrication techniques. The FPA is designed to absorb selective narrowband THz radiation at 2.06 THz and 4.75 THz, associated with atomic oxygen electron transitions, and convert it to long-wave infrared radiation (LWIR). The emitted LWIR can then be imaged by an uncooled microbolometer infrared camera. This effectively converts the THz emitting scene into an IR image that can be directly interpreted. In order for this technology to be tested in space, an optical system was designed, tested, and built to effectively utilize the band-converting capability of the FPA. The form factor of the resulting optical system, called the Terahertz Imaging Camera (TIC), is compatible with standard 6U CubeSat bus size, weight, and power requirements. The system is divided into two distinct sections, independent of each other due to separation by the FPA. The THz section focuses distant THz radiation onto the FPA via a 90°-fold parabolic mirror, while the IR section focuses the backside of the FPA onto the LWIR camera for imaging via two Ge meniscus lenses. The sensitivity of the system was found to be 1.0 K/μW, which translates to a 50 nW minimum detectable power by the LWIR camera.

THIS PAGE INTENTIONALLY LEFT BLANK

TABLE OF CONTENTS

LIST OF FIGURES

THIS PAGE INTENTIONALLY LEFT BLANK

LIST OF TABLES

THIS PAGE INTENTIONALLY LEFT BLANK

LIST OF ACRONYMS AND ABBREVIATIONS

ACA	ALMA Compact Array
ACM	attitude control module
AFOV	angular field of view
ALMA	Atacama Large Millimeter/Submillimeter Array
BFL	back focal length
CAD	computer aided design
CI	neutral carbon
CII	singly ionized carbon
COBE	Cosmic Background Explorer
COTS	commercial off-the-shelf
CRISTA	Cryogenic Infrared Spectrometers and Telescopes for the Atmosphere
DFG	difference frequency generation
DLATGS	deuterated L-alanine doped triglycine sulfate
DLR	downwelling longwave infrared radiation
DPM	data processing module
EFL	effective focal length
EPS	electrical power subsystem
ESA	European Space Agency
FFT	fast Fourier transform
FIRMOS	Far-Infrared Radiation Mobile Observation System
FLIR	forward-looking infrared
FORUM	Far-infrared Outgoing Radiation Understanding and Monitoring
FOV	field of view
FPA	focal plane array
FSI	FORUM Sounding Instrument
FSI	Fourier transform spectrometer

FTS	Fourier transform spectrometer
FWHM	full-width half-max
GEVS	General Environmental Verification Standard
GREAT	German Receiver for Astronomy at Terahertz Frequencies
GUSTO	Galactic/Extragalactic Ultra-Long-Duration Balloon Spectroscopic/Stratospheric Terahertz Observatory
HDPE	high density polyethylene
HEAT	High Elevation Antarctic Terahertz Telescope
HFA	High-Frequency Array
IR	infrared
LEO	low Earth orbit
LFA	Low-Frequency Array
LMC	Large Magellanic Cloud
LWIR	longwave infrared
MC3	Mobile CubeSat Command and Control
MEMS	microelectromechanical systems
MSL	mean sea level
NETD	noise equivalent temperature difference
NII	singly ionized nitrogen
NPS	Naval Postgraduate School
NSF	National Science Foundation
OI	atomic oxygen
OLR	outgoing longwave infrared radiation
PET	polyethylene terephthalate
QCL	quantum cascade laser
REFIR-PAD	Radiation Explorer in the Far-Infrared–Prototype for Applications and Development
RIKEN	Institute of Physical and Chemical Research
SDR	software-defined radio

SEM	scanning electron microscope
SERB	Space Experiments Review Board
SOFIA	Stratospheric Observatory For Infrared Astronomy
SPAS	Shuttle Pallet System
SRL	Sensor Research Laboratory
SSAG	Space Systems Academic Group
SSL	Small Satellite Laboratory
SWaP	size, weight, and power
THz	terahertz
THz-to-IR	terahertz-to-infrared
TIC	Terahertz Imaging Camera
TPX	polymethyl pentene
TT&C	telemetry, tracking, and command

THIS PAGE INTENTIONALLY LEFT BLANK

ACKNOWLEDGMENTS

The work embodied in this document represents well over a thousand hours of rigorous research, study, discourse, and practical experimentation. Consequently, these were hours in which I was not at home helping with my family duties—and so I am first and foremost thankful to my wife, Gina, for not only being an incredible caretaker to our son, Rainier, but also for being an endless well of mental and emotional support, all while juggling her own full-time career and master's degree program. It would be an understatement to say that the quality of my work is a direct reflection of her efforts and steadfast dedication. Thank you.

Furthermore, I am indebted to my advisors, Dr. Fabio Alves and Dr. Wenschel Lan, whose guidance and tutelage steered me through unfamiliar realms of research. They provided me with insights and course corrections where needed and, perhaps more importantly, fostered an environment conducive to growth, allowing me to navigate through challenges and eventual triumphs. As Dr. Alves aptly says, "Optics is a pain in the glass," a sentiment I have come to appreciate through firsthand experience. Additionally, I extend heartfelt gratitude to Ph.D. candidate Will Guimaraes Melos, who worked tirelessly alongside me in the laboratory, testing countless iterations of the optical system. He provided invaluable insights, guidance, and thoughtful ideas that helped shape the final product of this thesis: a spaceflight-worthy payload.

Most importantly, I am profoundly grateful to God for giving me the opportunity to grow and develop as a better follower of Christ. The guidance and grace afforded to me have been my constant companions, shaping my academic journey and spiritual growth.

THIS PAGE INTENTIONALLY LEFT BLANK

I. INTRODUCTION

The work of this thesis furthers ongoing research being conducted by the Naval Postgraduate School (NPS) Sensor Research Laboratory (SRL) and Small Satellite Laboratory (SSL) into the viability, applicability, and use of small form factor passive terahertz (THz) imagers in low Earth orbit (LEO). THz imaging research, as a whole, has undergone an expansion in the last three decades due, in large part, to the development of viable and commercially available THz sources and detectors. The development of these sources and detectors has contributed to a better understanding of THz radiation interactions with matter and developing applications in medical sciences, security screening, non-destructive evaluation of materials, atmospheric sciences, and remote sensing. The latter of these applications are of interest to the Naval Postgraduate School.

Until recently, imaging systems operating in the THz waveband required complex sensors, components, electronics, active cooling systems, or active THz sources to produce interpretable images. These systems tend to be large and expensive, relying on custom-made components and time-consuming fabrication processes. Researchers at the NPS Sensor Research Laboratory have developed a compact terahertz-to-infrared focal plane array (THz-to-IR FPA) that converts THz radiation to longwave infrared radiation (LWIR) without the need for active cooling. The THz-to-IR FPA absorbs select frequencies of THz radiation on one side of the focal plane array, which is converted into heat, and emits broadband blackbody radiation on the backside of the focal plane array (FPA). The LWIR band from the emitted blackbody radiation can then be focused on an uncooled, commercial off-the-shelf (COTS) LWIR camera, effectively creating an infrared radiation (IR) image of a THz scene. The THz-to-IR FPA enables simple designs, fast production, and coupling of commercially available components for relatively low-cost and agile employment aboard a standard CubeSat.

An additional benefit to utilizing the THz-to-IR FPA is that it can be custom-fabricated to selectively absorb specific frequencies of THz radiation by varying the dimensions and materials of the sensor constituents. This allows the ability to isolate THz frequencies associated with phenomena of interest without complex electronics and signal processing techniques. One such phenomenon of interest is the emission of THz radiation by atomic oxygen (OI) electron transitions. Two prominent OI electron transitions emit photons at 2.06 THz and 4.75 THz. A single THz-to-IR FPA can be fabricated to absorb both of these frequencies by controlling the dimensions of the absorbing resonators within each pixel of the FPA. Emissions at these frequencies can be used to map upper-atmospheric densities and winds, which impact satellite communications as radio waves pass through turbulence caused by these perturbations. With accurate mapping, communications waveform properties can be adjusted to compensate for the turbulence, resulting in more efficiency in communications links [1]. Various human-induced sources also stimulate emissions at these frequencies, including hypersonic activity and spacecraft reentry into the atmosphere, which causes the dissociation of molecular oxygen into OI at the superheated laminar flow boundary layer [2].

The radiation band emitted by the back side of the THz-to-IR FPA is independent of the incident THz radiation. Therefore, uncoupled optics can be used in each portion of the imager. THz optics (lenses or mirrors) can be used to focus distant THz radiation to the front side of the sensor, whereas IR optics (lenses or mirrors) can be used to focus the backside of the THz-to-IR FPA onto the LWIR camera FPA. This allows the use of different THz-to-IR FPAs tuned to various emission phenomena, without changing the optics.

Upon deployment aboard a satellite, the imager will target in the nadir direction from a planned operational altitude of 500 km to detect THz emitting phenomena in the upper ionosphere, which also coincides with the mid-thermosphere. The ionosphere extends from approximately 60 km to 300 km, with the thermosphere extending from 80 km to 700 km [3]. Imaging the upper ionosphere in the THz spectrum can only be achieved from above a significant portion of the atmosphere as polar molecules, such as water, cause extreme attenuation of THz radiation due to their rotational transitions. The percent of atmospheric transmission of radiation of varying wavelengths originating at sea level is shown in Figure 1. High levels of water vapor in the atmosphere at lower altitudes make THz imaging of the upper ionosphere from the ground impractical. Therefore, deploying imagers from LEO is an attractive solution to achieve passive THz imaging of the upper atmosphere.

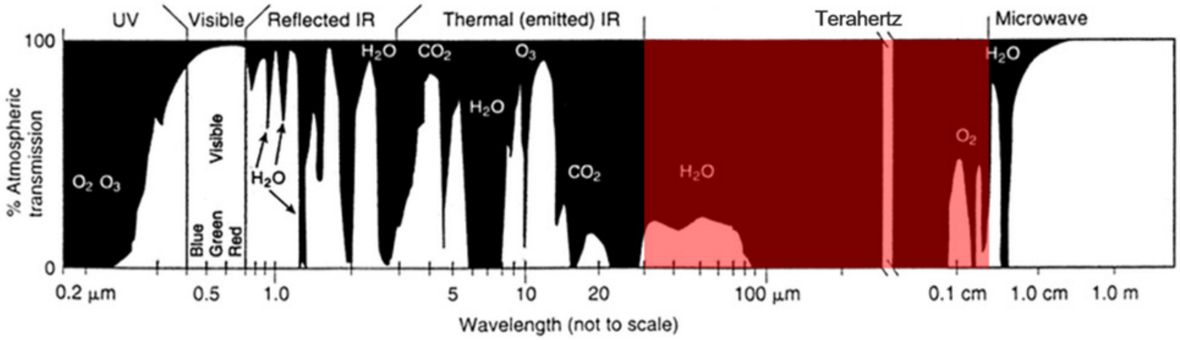

The THz spectrum is highlighted in red. The discontinuity area denotes 0 percent transmission in those wavelengths.

Figure 1. Atmospheric transmission for varying wavelengths. Adapted from [4].

As of the writing of this thesis document, one iteration of the THz imager has been built, tested, and integrated into a 6U CubeSat, named Mola, developed by the NPS Space Systems Academic Group (SSAG) Small Satellite Laboratory. It is currently awaiting launch aboard a Rocket Lab Electron launch vehicle. The previous version of the imager utilizes a 2-inch aperture lens-based optical design and an early version of the THz-to-IR FPA, designed to detect a very broad THz band.

The imager presented in this research sought to improve upon the design of the previous iteration in several ways. First, significant advancements have been made in the fabrication process of the THz-to-IR FPA. Advancements have allowed researchers to fabricate various configurations and types of FPAs, many of which are designed to absorb only select narrowband THz frequencies. Characterization of several of these newer iterations of THz-to-IR FPAs has been conducted in tandem with this research, one of which will be selected to be integrated into the imaging system for spaceflight. Second, a larger aperture was used in this application, increasing the aperture from 2-inches to 3-inches—a 225% increase in light-gathering area. Third, more payload volume space was allocated for the imaging system in the planned CubeSat bus. This allowed for designs with longer focal length optical components than previously used, reducing aberration and distortion. Additionally, the increased volume allowance permitted the use of mirror-based designs, which exhibit increased reflectivity in the THz spectrum when compared to refractive optics.

The research conducted in this thesis aims to contribute to the overall project goal of testing of a small form factor, low-cost Terahertz Imaging Camera (TIC) in LEO to prove the concept and evaluate its viability in imaging THz scenes in the upper ionosphere. This iteration of the THz imager will yield data that informs researchers on future research and development cycles to further optimize the imaging system. Sensor performance and survivability, optical performance, and image collection data will feed further development cycles with the ultimate goal of enabling important Department of Defense missions by mapping THz emissions in the upper ionosphere through a proliferated network of imagers.

A. THE TERAHERTZ RADIATION SPECTRUM

The THz spectrum resides within the electromagnetic radiation spectrum from approximately 0.1 THz (3 mm) to 10 THz (30 μm), encompassing the waveband between the far IR spectrum and the microwave spectrum [5]. In the 1980s, a combination of research and technological developments helped close what has been coined the "terahertz gap." The terahertz gap is a product of the inherent difficulties associated with THz production and detection, as neither efficient detectors nor capable emitters were available to bridge this gap until recently. This is as opposed to the IR and microwave spectra surrounding the THz spectrum, both of which have had wide-ranging applications for many decades. More recently, advances in THz emission and detection technologies have contributed to several practical applications of THz imaging in the fields of sub-millimeter wave astronomy, security screening and imaging, nondestructive evaluation of materials, medical imaging, and environmental and atmospheric sciences.

1. Terahertz Sources

Natural THz emissions are common and varied in their sources and emission methods. The entirety of the universe is bathed in THz radiation as a byproduct of the energy produced by the Big Bang, which has had billions of years to cool to the relatively uniform background temperature of space of 2.725 K [6]. The cosmic background radiation's peak intensity occurs at a frequency of 0.160 THz, which resides in the overlap of the shortwave millimeter spectrum and longwave THz spectrum. The sun is also a THz emitter, though at significantly lower power levels than the Sun's peak emissions in the visible spectrum. This is because the Sun acts loosely as a blackbody, which, according to Plank's quantum theory, emits radiation at all frequencies. Wien's Displacement Law is a derivation of Plank's blackbody radiation function and gives the peak emission frequency as inversely proportional to the observed temperature of the object, as shown in Equation 1 [7].

$$\lambda_{max} = \frac{a}{T} \tag{1}$$

where λ_{max} is the peak emission wavelength in µm, a is Wien's constant and has a value of 2898 µm·K, and T is the average observed temperature of the object in K. Solving Wien's Law for temperature and using the standard definition of the THz band (3 mm to 30 µm) shows that objects emit most prominently in THz frequencies between 0.966 K and 96.6 K. This means that THz imagers are ideal for imaging objects between these temperatures, such as space debris that are too cold to be imaged by IR detectors.

THz radiation can also be emitted from atoms and molecules through electron energy level transitions or changes in molecular thermal, bending, or rotational states. Electron transitions from higher to lower energy levels cause atoms to emit radiation in specific frequencies, or line emissions, which correspond to the energy lost as the electron transitions to a lower energy state. Atomic oxygen emits THz radiation in two prominent frequencies: 2.06 THz associated with the OI($^3P_0$) to OI($^3P_1$) transition, and 4.75 THz associated with the OI($^3P_1$) to OI($^3P_2$) transition [8]. Both the 2.06 THz and 4.75 THz emissions are the brightest line emissions in the upper ionosphere when measured by photon flux (number of photons per unit area per unit time) [9]. They are, therefore, ideal candidates for imaging THz emissions in the upper ionosphere.

There are also several methods in which THz radiation can be produced artificially. These methods include optically pumped short-pulse lasers, difference frequency generation (DFG) using CO_2-lasers or nonlinear crystal optical lasers, optically pumped THz lasers, P-germanium (P-Ge) THz lasers, and quantum cascade lasers (QCL) [10]. The latter was used to characterize the THz-to-IR FPA and THz portion of the TIC's optical system. The NPS Sensor Research Lab's 4.7 THz QCL was used as the primary illumination source to characterize THz-to-IR FPA sensitivities and optical focalization. This is further discussed in Chapter IV.

2. Terahertz Remote Sensing

THz detection is distinctly classified into two detection techniques: coherent and noncoherent. Coherent detection involves the measurement of both the amplitude and phase of the electromagnetic field, while noncoherent detection involves only measuring the intensity of the electromagnetic field. Remote sensing of THz radiation is also classified into active and passive detection. Active detection requires an active radiation source, or sources, in which an image is formed by detecting the reflected or back-scattered radiation off a target. Active detection allows for control over the characteristics of the emitted beam, e.g., intensity, direction of propagation, frequency, and beam shape.

Passive detection utilizes sources produced externally to the imager setup—most often natural sources. The external source can be imaged directly, as in the case of imaging OI in the atmosphere. Additionally, the source can be used to illuminate a target and detect the reflected or back-scattered radiation, as in imaging a satellite as it reflects radiation from the sun. Control of the emission source characteristics in passive detection is not possible. Therefore, passive detection requires sensors that are carefully designed and are extremely sensitive, as natural THz sources are generally weaker and more diffuse than active sources.

To overcome the obstacles associated with passive detection, nearly all existing passive THz imagers use superconducting sensors that require active cooling to cryogenic temperatures ($< 10K$) to reduce thermal noise. One principal advantage of using the THz-to-IR FPA, described in this thesis, is that it does not require complex thermal controls, even though the detection technique utilized is passive detection of non-coherent THz radiation from natural sources.

B. THZ-TO-IR FOCAL PLANE ARRAY

The key technology that enables the TIC is the THz-to-IR FPA, without which the key design requirements of low-cost, low-power, and small form factor would not be possible. Research, development, and fabrication of uncooled microelectromechanical systems (MEMS) band-converting focal plane arrays have been the focus of the NPS Sensor Research Lab since 2012. These band-converting arrays are designed to absorb select THz frequencies on a metamaterial-based pixel comprised of multiple absorbing resonators. The absorbed THz radiation heats the pixel front side and emits LWIR radiation on the backside [11]. Fabrication of these arrays is made possible through standard MEMS microfabrication techniques employed at the class 1000 clean room at NPS and are described in detail in [12], [13], [14], and [15]. Several iterations of the THz-to-IR FPA have been produced to date and have demonstrated both effective absorption in the THz spectrum and emission in the LWIR spectrum. These focal plane arrays have also demonstrated sufficiently small thermal time constants to allow for real-time imaging applications [12], [15].

The THz-to-IR FPAs utilized in this research were developed and fabricated by a team of NPS faculty and students and present novel pixel designs. A recently fabricated FPA that was used in portions of this thesis research is shown in Figure 2. Previous versions of the THz-to-IR FPA have used square or rectangular resonators that can be tuned to absorb select THz frequencies by varying the material properties of the metamaterial pixels and geometry of individual resonators [12]. Square and rectangular resonators are advantageous for use in focal plane arrays as they maximize the usage of the pixel's surface area. However, their design presents difficulties in fabrication due to their sharp corners [16]. A representative square resonator design is shown in Figures 3 and 4.

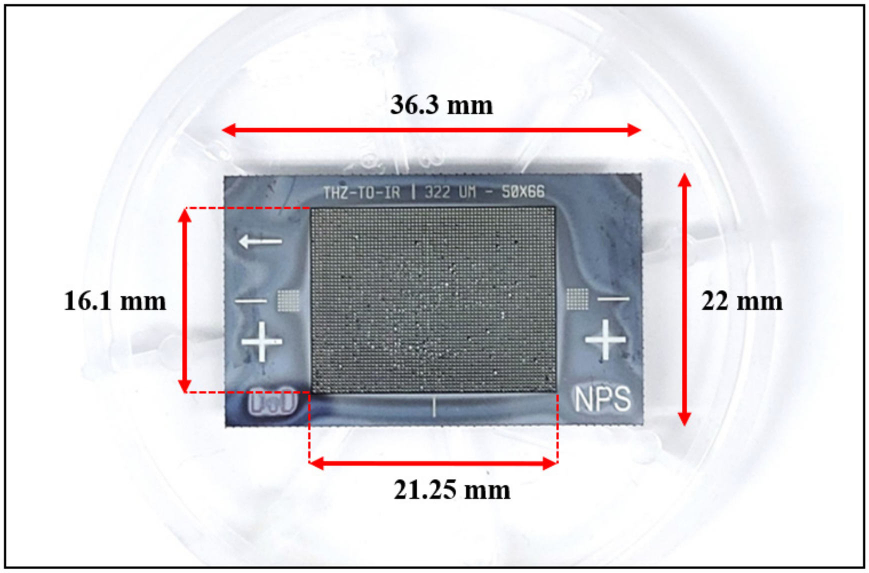

Figure 2. Fully fabricated THz-to-IR FPA dimensions.

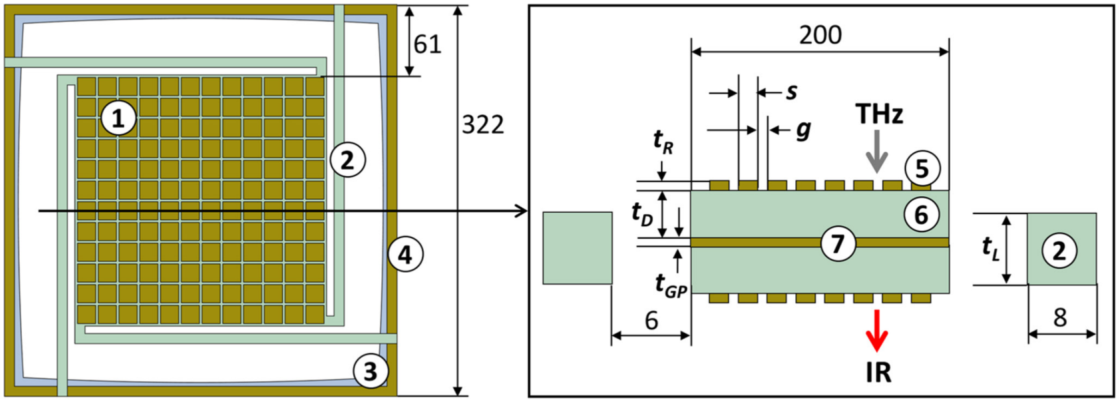

(a) (b)

"(a) Top-view layout of a single pixel device showing the planar metamaterial absorber (1), held in place by four symmetric thermal insulating beams (2) connected to the substrate frame (3). An aluminum frame (4) acts as a heatsink. In a focal plane array, this pixel repeats in a 2D fashion. (b) Cross-sectional layout of the sensor depicted in (a) showing two identical planar metamaterial structures mirrored around the ground plane, where the aluminum resonators (5) are sitting on a dielectric spacer (6). The ground plane (7) works for both metamaterial structures. All dimensions are in µm, and t_D, t_R, t_{GP}, t_L are the thicknesses of the dielectric, resonators, ground plane, and thermal insulating beams, respectively. The resonator's size and gap between them are represented by *s* and *g*, respectively." Source: [12]

Figure 3. Metamaterial-based MEMS THz-to-IR band converter. Source: [12].

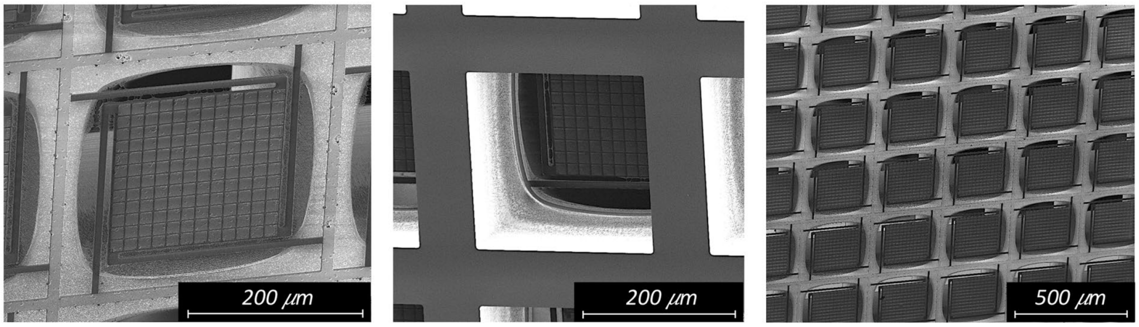

(a) (b) (c)

“SEM micrographs of fabricated sensor B (a) front side, (b) backside, and (c) a section of the focal plane array. Images were made using beam excitation of 2 kV and magnification of 700X, 650X, and 400X, respectively.” Source: [12]

Figure 4. MEMS metamaterial-based THz-to-IR sensor SEM micrographs. Source: [12].

The THz-to-IR FPAs used in this research are based on a circular resonator design. The frequency of THz absorption is controlled by the material selection of the metamaterial pixels and varying the diameter of each resonator within the pixels. Two different circular resonator diameters were selected to allow for independent absorption of 2.06 THz and 4.75 THz radiation. The first THz-to-IR FPA is designed with interspersed 2.06 THz and 4.75 THz sensitive resonators within each pixel across the entire focal plane array, as shown in Figure 5. This design allows for both 2.06 THz and 4.75 THz scenes to be imaged simultaneously over the entire focal plane array but does not allow for distinction between images produced by 2.06 THz, 4.75 THz, or a combination of both.

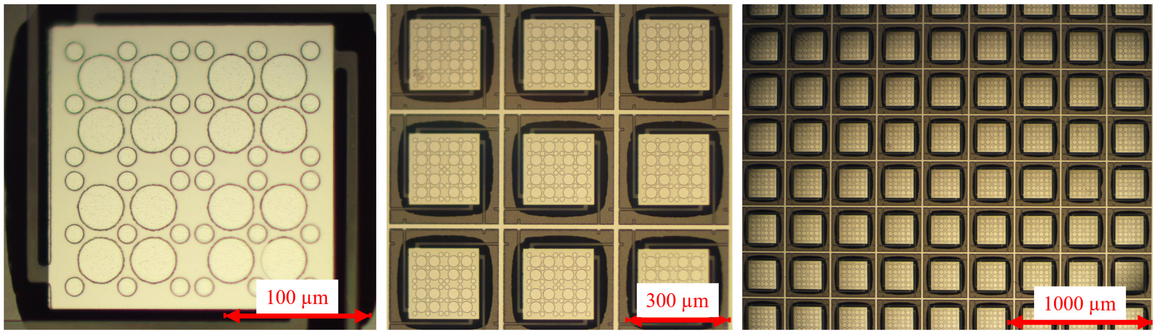

Images taken with a scanning electron microscope (SEM).

Figure 5. THz-to-IR FPA with interspersed resonators sensitive to 2.06 THz and 4.75 THz. Source: [15].

The second design is configured with one-half of the focal plane array containing only 2.06 THz resonators and the other half containing only 4.75 THz resonators, as shown in Figure 6. This design distinguishes which target frequency produces the resultant LWIR image but also effectively reduces the horizontal field of view (FOV) to half of the entire focal plane array. Relevant characterization data for the THz-to-IR FPA is included in Chapter IV and was measured concurrently with the design of the TIC's optical system. Both designs measure 21.25 mm by 16.1 mm and achieve an array of 66×50 pixels for a total pixel count of 3,300.

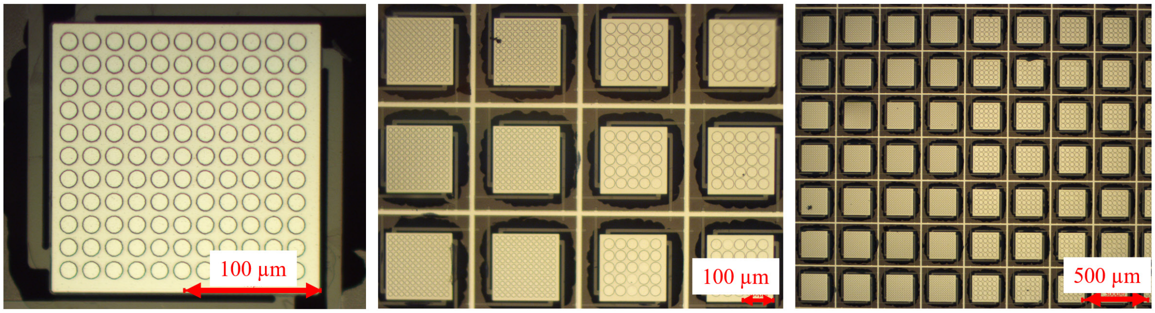

Images taken with a SEM.

Figure 6. THz-to-IR FPA with the left half containing 2.06 THz sensitive resonators and the right half containing 4.75 THz sensitive resonators. Source: [15].

C. OBJECTIVES

This thesis work aimed to develop the optical system for a small form factor, low-cost THz imager for space applications. This development included the designing, building, and characterizing of a frequency-independent focalization system for integration into a 6U CubeSat. The primary objective was to develop an optical system that displays the best optical characteristics possible using almost exclusively COTS components given the size, weight, and power (SWaP) constraints of a 6U CubeSat bus. The optical system that stayed within the SWaP constraints, exhibited acceptable focus, magnification, and field of view requirements, maximized THz and LWIR transmission, and minimized aberrations was chosen as the final design. Both lens and mirror designs were evaluated in this research.

The optical system is classified into two sections: THz and IR. The THz section consists of an optical element that is refractive or reflective in THz frequencies, an IR filter (for the reflective optics), and terminates at the THz-to-IR FPA. The THz optical element's function is to focus collimated radiation from a far distant source onto the THz-to-IR FPA. Filtering is necessary as IR incident on the THz-to-IR FPA heats the array, yielding an inaccurate image captured by the LWIR camera. The IR section consists of optical elements that are transmissible or reflective in LWIR wavelengths specific to those emitted by the back side of the THz-to-IR FPA. Therefore, the radiation spectrum emitted by the THz-to-IR FPA was considered when choosing these elements. The function of the IR optical components is to demagnify and focus the back of the THz-to-IR FPA onto the focal plane array of the LWIR camera used for imaging. The images produced by the LWIR camera are output in video format for image processing.

This thesis focused on the optical design rather than the THz-to-IR FPA, which was the work of other NPS Physics Department faculty and students. However, close coordination and integrated work was conducted with the NPS Physics Department and those working on the THz-to-IR FPA to finalize the design of the TIC. This research did not include the integration of the TIC into a CubeSat bus and its associated subsystems. However, it did consider the SWaP constraints imposed by integration into a 6U CubeSat bus.

D. RESEARCH QUESTIONS

There are two primary research questions that this thesis work aspired to answer:

1. What minimum performance and attributes (FOV, resolution, aberration characteristics) are achievable for imaging the upper ionosphere from an altitude of 500 km using a 3-inch aperture optical system constrained to a 6U CubeSat?

2. What is the optimal system design of a 3-inch aperture THz imager that stays within the size, weight, and power constraints of a 6U CubeSat bus: lens-based, mirror-based, or hybrid?

E. ORGANIZATION OF THESIS

This thesis document is organized to aid the reader in following the research, experimentation, and results of the work that spanned over a year. Chapter II provides a thorough literature review of previous work relevant to the efforts of the NPS Sensor Research Lab and Small Satellite Laboratory on passive THz remote sensing and imaging. This thesis continues previous work by other students at NPS. Accordingly, their efforts are also reviewed in this chapter. Chapter III is a description of the optical system's design. The design constraints are also presented as required by a notional 6U CubeSat bus and include size, weight, and power considerations. The configuration of the optical system and its alternatives are offered along with their respective analytical models as provided by modeling and raytracing software. Chapter IV presents the experimental setup, results, and final optical system selected for spaceflight. This chapter also includes select THz-to-IR FPA characterization data using a 4.7 THz QCL, which were measured in conjunction with the design of the optical system as captured in this thesis. Chapter V summarizes the optical system design, experimental setup, and results and compares these with comparable systems as discussed in the Literature Review. Chapter V also presents the TIC's impact to the defense community and recommendations for future research.

II. LITERATURE REVIEW

Numerous ground, air, and space-based instruments have detected emissions in the THz frequency spectrum (0.1–10 THz) over the last 70 years. These instruments have predominantly been designed and utilized for atmospheric monitoring, Earth remote sensing, or astronomic observations. The naming conventions of the electromagnetic radiation spectra to which these instruments are sensitive are unique and differ from the THz spectra described in Chapter I. This is due to the overlap of THz wavelengths with the radio, microwave, and IR spectra. Many of the collection spectra of instruments are further defined as millimeter, submillimeter, or far-infrared, all of which overlap the THz spectrum [5], [17], [18], [19]. These naming conventions are commonly accepted lexicon in their respective scientific fields and predate practical applications in THz remote sensing. The most common definitions of these spectra are shown in Table 1.

Table 1. Common definitions of spectra that overlap the THz spectrum. Adapted from [5], [17], [18], [19].

Spectrum	Frequency	Wavelength
Millimeter	0.03–0.3 THz	996 µm–10 mm
Submillimeter/Microwave	0.3–1 THz	300 µm–1 mm
THz	0.1–10 THz	30 µm–3 mm
Far-Infrared	1–20 THz	15 µm–1 mm

Several instruments that are sensitive to these varied spectra are described in this chapter. Focus is placed on those instruments and spectra directly overlapping the THz spectrum. Rather than classify existing or planned instruments by their respective spectral bands, instruments are classified within this chapter by the medium in which they are/were designed to operate, i.e., ground, air, or space. Some general characteristics, strengths, and weaknesses can be attributed to each of these operation regimes and are described in their respective sections. The previous iteration of the NPS-designed TIC is also presented in this chapter.

A. GROUND-BASED INSTRUMENTS

Observations of THz radiation originating from atmospheric and astronomic sources from ground-based instruments are the most challenging to observe due to strong absorption by atmospheric water vapor, as described in Chapter I. Ground-based instruments are particularly affected by atmospheric and weather phenomena, of which moisture and precipitation play the most significant role. For this reason, ground-based instruments designed to sense in the millimeter, sub-millimeter, and low-THz frequency ranges (< 2 THz) are strategically located in regions of high elevation and low humidity. Ground-based instruments have the benefit of fewer restrictions in size, weight, and power requirements when compared to analogous airborne and space-based instruments. This allows for fielding extremely large apertures and arrays and their associated size, weight, and power requirements. An additional benefit of ground-based instruments is the ability to repair, replace, and upgrade system components at will, as observatories are easily accessible.

1. Atacama Large Millimeter/Sub-Millimeter Array

The Atacama Large Millimeter/Sub-Millimeter Array (ALMA) is a very large radio-telescope array located at an altitude of 5 km on the Chajnantor Plateau in the Chilean Andes [20]. This location is one of the driest on Earth and benefits from infrequent weather conditions that impact trans-atmospheric observations. The observatory began operations in 2011 following a $1.4-billion construction cost and continues operations to date with yearly management and operations costs of approximately $100-million [21]. ALMA was constructed to probe the coldest regions of the universe by imaging and analyzing the spectral features of extremely red-shifted cosmic phenomena, including early galaxies and stellar formations. The array detects in the millimeter and submillimeter spectra spanning 35 GHz–0.950 THz, separated into ten customized bands within atmospheric transmission windows, as shown in Figure 7 [20]. The observation bands were selected to coincide with favorable atmospheric transmission windows. Figure 7 shows that transmission generally decreases as frequency increases, and several frequency bands of zero or near-zero transmission are associated with water vapor absorption.

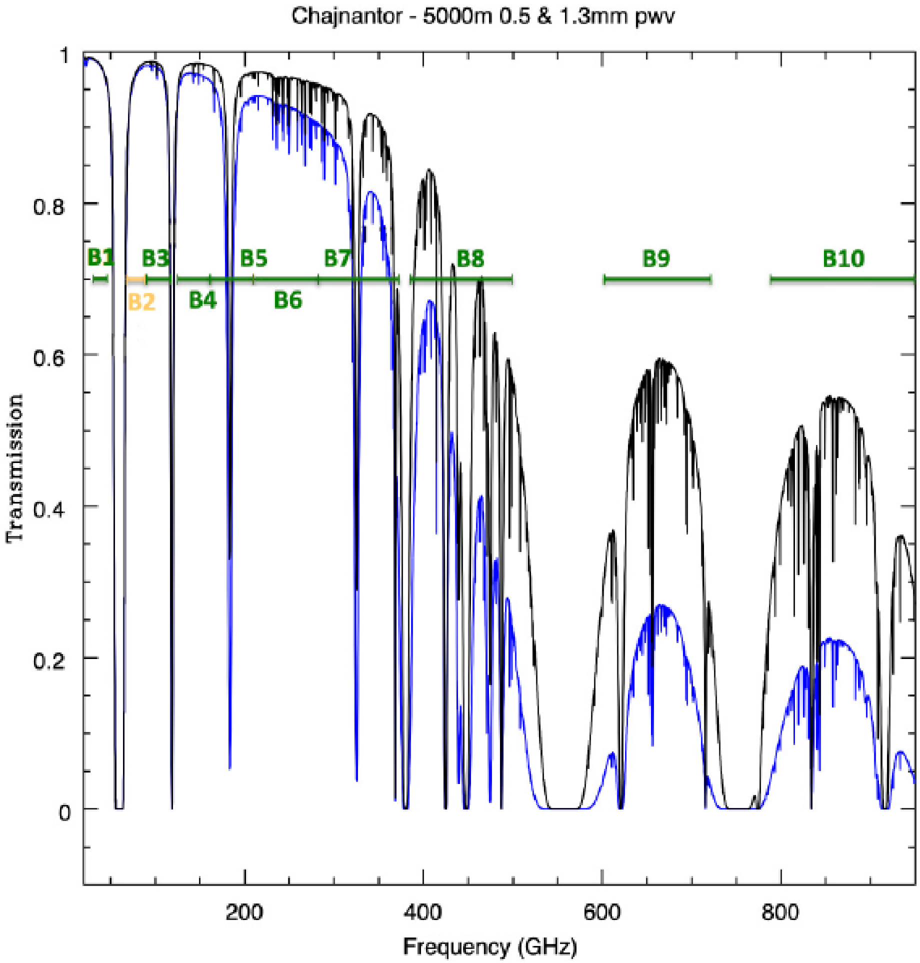

ALMA detection bands B1–B10 are shown in the image (green and yellow). Blue and black lines represent transmission with 1.3 mm and 0.5 mm precipitable water vapor (PWV) columns, respectively. 1.3 mm and 0.5 mm PWV represent historical atmospheric column water vapor conditions at the 55th and 25th percentile, respectively, averaged throughout one year.

Figure 7. Atmospheric transmission windows for observations at ALMA. Source: [20].

As the name implies, ALMA is a telescope array comprised of a network of antennas. ALMA encompasses two independent arrays, the 12-m Array and the ALMA Compact Array (ACA). The 12-m Array is a collection of fifty 12-m antennas, while the ACA is made up of twelve 7-m antennas and four 12-m antennas [20]. Each antenna points at the same field of interest during observations, collecting electromagnetic radiation in a single band of interest [22]. Rather than form images directly from observations (as an FPA does), ALMA's array functions as an interferometer between baseline pairs of each antenna. The energy received at each antenna is cross-correlated between each of its baseline pairs, and a Fourier transform is conducted to create an image from the raw data. The approximate time from initial collection to fully formed images is 24 hours. Because the angular field of view and resolution are dependent on the distance between a baseline pair, a wide range of fields of view and resolution can be produced from the array. The distance between the closest and most distant baseline pairs ranges from 150 m to 16 km [20]. ALMA's specifications and performance figures are shown in Table 2.

Table 2. ALMA 12-m array specifications and figures of performance. Adapted from [20], [22].

Specification	Figure of Performance
Full Spectral Range	350 GHz–0.95 THz
Spectral Resolution	3.8 kHz–15.6 MHz
Angular Field of View (FWHM)	6.1–117 arcsec
Angular Resolution	0.01–7.1 arcsec

2. Far-Infrared Radiation Mobile Observation System

The Far-Infrared Radiation Mobile Observation System (FIRMOS) conducted operations in winter 2018 from atop Mount Zugspitze in Germany [23]. FIRMOS was located adjacent to the Zugspitze Observatory at an altitude of 2.96 km, a relatively low altitude for a far-infrared receiver. However, a lower altitude environment did not hinder its collection as it was designed to detect down-emitted far-infrared radiation from the lower atmosphere. FIRMOS was conceived as a technology, instrument, and methodology demonstrator for the Far-infrared Outgoing Radiation Understanding and Monitoring (FORUM) satellite mission scheduled for launch in 2027 [24]. During its two-month operational period in 2018, FIRMOS validated the instruments and collection techniques that will be employed on FORUM. FIRMOS's Fourier transform spectroradiometer (FTS) measured downwelling longwave infrared radiation (DLR) from the atmosphere in the 3–30 THz (10–100 μm) range [23]. DLR measurements were used to spectrographically resolve water vapor and carbon dioxide absorption lines, informing researchers on radiative transfer within the atmosphere. This data, coupled with anticipated measurements from FORUM, will be used to better understand the radiative balance between the Earth, its atmosphere, and surrounding space, leading to more accurate climate models [25].

FIRMOS was also purposefully designed to be compact. It measured 85 × 95 × 50 cm and weighed 80 kg [23], [25]. Its compact size also necessitated a modest 60 W power requirement. The primary aperture of the system was a 76.2 mm (3 inches) germanium-coated polyethylene terephthalate (PET) lens, and its detector was a room temperature 2 mm single-pixel deuterated L-alanine doped triglycine sulfate (DLATGS) pyroelectric detector. FIRMOS was not an image-producing instrument due to its single-pixel design and, therefore, does not have a corresponding spatial resolution. Further specifications and figures of performance are shown in Table 3. FIRMOS funding and project costs were not available in the public domain at the time of this writing.

Table 3. FIRMOS specifications and performance figures. Adapted from [23], [25].

Specification	Figure of Performance
Full Spectral Range	3–30 THz
Spectral Resolution	9 GHz
Angular Field of View	1.26°
Angular Resolution	N/A
DLATGS Sensor Temperature Accuracy	30 mK

3. High Elevation Antarctic Terahertz Telescope

The High Elevation Antarctic Terahertz Telescope (HEAT) is a remotely operated astronomic observation instrument located at the Dome A plateau, approximately 80° south latitude on the Antarctic continent [26]. HEAT began operations in January 2012 as a joint effort between the National Science Foundation (NSF), the University of Arizona, the Australian University of New South Wales, and the Chinese government, who founded the research station at Dome A [27], [28]. As of 2014, the NSF has obligated $1.76-million to the HEAT observatory. No information concerning the University of New South Wales's monetary contributions was available during this writing.

Dome A is perhaps the most ideal location on Earth's surface to observe astronomic phenomena at THz frequencies [26]. This is due to Dome A's 4.1 km elevation and, more importantly, the site's extremely cold and dry atmospheric conditions. These characteristics result in atmospheric THz transmissions comparable to those of the Stratospheric Observatory for Infrared Astronomy (discussed later in this chapter), an airborne observatory that operated at 41,000 ft (12.5 km). Figure 8 shows the transmission of THz frequencies through the atmosphere above Dome A and compares it to transmission at the South Pole. Much like Figure 7, Figure 8 shows that transmission generally decreases with increased frequency in its spectral range and the presence of several zero-transmission bands.

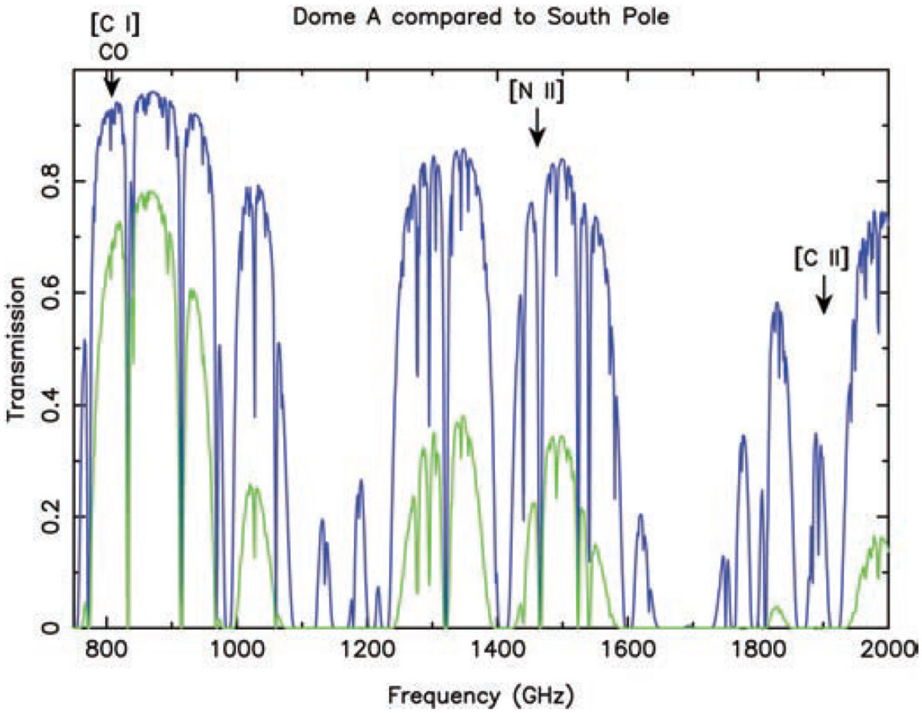

The depicted transmission windows are for 25th percentile conditions at Dome A (blue line) compared to 25th percentile conditions at the South Pole (green line) using measured weather data and atmospheric models.

Figure 8. THz atmospheric transmissions at Dome A and the South Pole. Source: [26].

The observatory continues operations as of this writing, observing the life cycle of interstellar clouds and galactic star formation rates at THz frequencies between 0.5 and 2 THz (150–600 µm). HEAT employs a 61 cm off-axis parabolic mirror focused on heterodyne receivers cryogenically cooled to 50 K [29]. The heterodyne receivers are tuned to detect electron transitions of neutral carbon (CI), singly ionized carbon (CII), and neutral carbon monoxide (CO). The primary science goal of HEAT is to make spectroscopic observations of interstellar atomic and molecular clouds as they form into stars to better understand the evolution of our own Milky Way galaxy [26]. These observations are used to model the galactic evolution of the Milky Way and can be used as a baseline for modeling the evolution of other galaxies. In addition to modeling galactic evolution, HEAT is an ideal "finder-scope" for larger, more sensitive instruments, like ALMA. HEAT can find objects of interest using its wider field of view and inform researchers at larger facilities to begin observations for the collection of more exquisite data [27]. The specifications and figures of performance for HEAT's optics and sensors are shown in Table 4. The spectral resolution of HEAT's heterodyne receivers is given in velocity units in [26] due to measuring astronomic phenomena with doppler-shifted frequencies. The velocity units are translated into frequency units for comparison to other instruments by Equation 2 [22].

$$R_{frequency} = \frac{\left(f_{center}\right) \times \left(R_{velocity}\right)}{c} \tag{2}$$

where $R_{frequency}$ is the spectral resolution in frequency units, f_{center} is the center frequency of the measurement, $R_{velocity}$ is the spectral resolution in velocity units, and c is the speed of light. The reported best velocity resolution of HEAT for the CI emission line centered at ~809 GHz is 0.4 km/s [26], [30]. This gives a spectral resolution of 1.08 GHz.

Table 4. HEAT specifications and figures of performance. Adapted from [26], [30].

Specification	Figure of Performance
Full Spectral Range	0.5–2 THz
Spectral Resolution	1.08 GHz
Angular Field of View	1.0°
Angular Resolution	1.0–2.5 arcmin

B. AIRBORNE INSTRUMENTS

Airborne instruments are typically deployed on either balloon or aircraft platforms to reduce the effects of water vapor absorption in the lower atmosphere. At an altitude of 41,000 ft, instruments are above 99% of total atmospheric water vapor [31]. This results in less attenuation of certain spectral bands in the 1–1000 μm range compared to ground-based instruments. However, certain spectral bands are particularly affected by water molecule vibrational and rotational states, resulting in transmission of these frequencies at or near 0%, even at higher altitudes [31]. This necessitates the careful selection of detection wavelengths that reside within the narrow bands of favorable atmospheric transmission. Figure 9 compares varying wavelength transmissions through the atmosphere from a ground-based observatory at Mauna Kea, Hawaii, at 13,800 ft (4.2 km), and an airborne observatory at 41,000 ft (12.5 km).

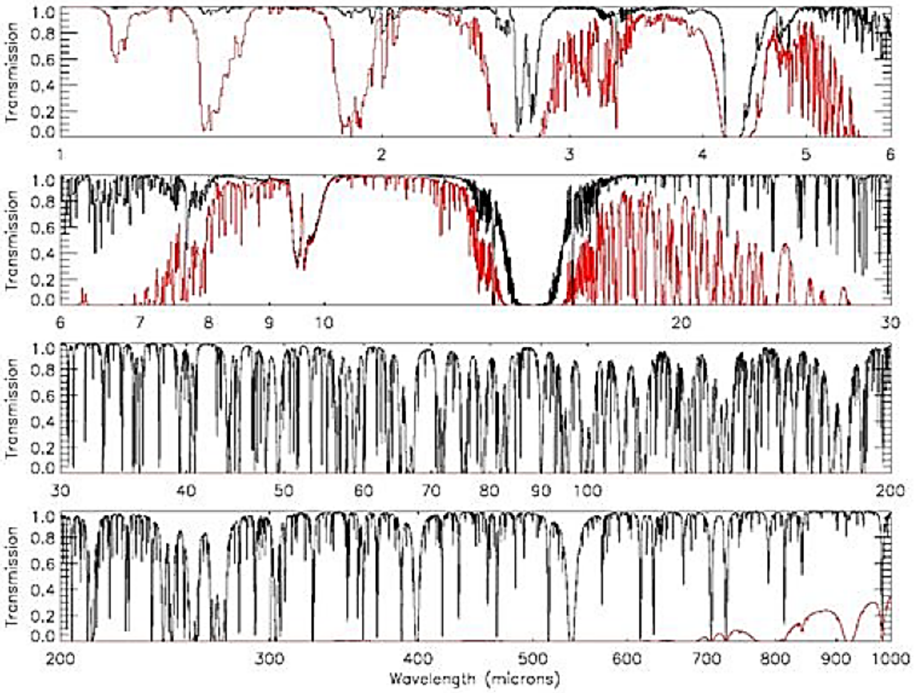

The black line represents the atmospheric transmission of an airborne instrument at 41,000 ft compared to the red line, which represents a ground-based instrument at 13,800 ft. Transmission windows were calculated using ATRAN code. The ground-based transmission is at or near zero from approximately 28.5–680 µm (0.44–10.5 THz).

Figure 9. Atmospheric transmission for an airborne instrument compared to a ground-based instrument. Source: [31].

As expected, airborne instruments are more restricted in their SWaP when compared to ground-based instruments; however, they are less constrained than comparable space-based instruments. This is primarily because airborne instruments are significantly cheaper to deploy than space-based instruments on a per-kilogram basis. However, as aircraft-mounted instruments cannot fly continuously like their space-based counterparts, the cost per observation-hour can far exceed those of space-based instruments [32]. Additionally, the ability to repair, retrofit, and replace airborne instruments is retained as these systems are often designed to be recovered and redeployed.

1. Stratospheric Observatory for Infrared Astronomy

The Stratospheric Observatory for Infrared Astronomy (SOFIA) was a premiere airborne platform for IR and millimeter observations that operated from 2014 to 2022 [33].

The platform was based on a Boeing 747 airframe specially modified for joint NASA and German Space Agency remote sensing and observations programs. SOFIA carried numerous instruments and experiments throughout its eight-year lifetime and is estimated to have cost \$3-billion throughout its life cycle with an \$83-million per year operational cost [32]. SOFIA operated in annual cycles and was a platform for scientists and researchers to conduct atmospheric and astronomic observations for independent research. SOFIA provided a unique environment for observations in the THz spectrum, capable of cruising at altitudes between 37,000–45,000 ft. It carried a 2.7 m reflecting telescope designed to operate in the 0.3–1600 μm range and featured mounts for independent measurements by six instruments. Of the many instruments that SOFIA carried throughout its lifetime, three made observations primarily in THz frequencies.

One of these instruments was the German Receiver for Astronomy at Terahertz Frequencies (GREAT). GREAT was composed of three heterodyne sub-instruments sensitive to different frequency bands within the THz spectrum. A quantum cascade laser was used as a local oscillator—a necessary component of heterodyne receivers. Both the heterodyne receivers and QCL required cryogenic cooling to < 4.5 K and 30 K, respectively [34], [35]. In total, the GREAT instrument weighed approximately 500 kg. The three sub-instruments consisted of the High-Frequency Array (HFA), Low-Frequency Array (LFA), and 4GREAT.

The HFA was a 7-pixel hexagonal array tuned to the 4.75 THz (63 μm) $OI(^3P_1)$ to $OI(^3P_2)$ transition [31], [36]. One notable experiment that utilized HFA measurements was conducted by [36] to map OI concentrations in the mesosphere and lower thermosphere. This SOFIA flight facilitated measurements from 130–175 km altitudes above the Pacific Ocean from off the coast of northern Mexico, extending to Southern Canada. The GREAT OI concentration measurements agree with atmospheric models derived from satellite observations [36]. Another notable experiment conducted using GREAT measurements successfully observed OI emissions in Mars's atmosphere.

The LFA was a 14-pixel array comprised of two smaller arrays of 7-pixels, each arranged in hexagonal patterns. The LFA was sensitive to the 1.835–2.007 THz range with an additional detection band from 2.060–2.065 THz, which corresponds to the $OI(^3P_0)$ to

OI($^3P_1$) transition [31]. The third heterodyne instrument was the 4GREAT, comprised of four pixels, each of which was sensitive to unique frequency ranges: 0.491–0.635 THz, 0.890–1.092 THz, 1.240–1.525 THz, and 2.490–2.590 THz. Each of the three sub-instruments was paired to a Fast Fourier Transform (FFT) spectrometer and featured a total bandwidth of 4 GHz across 16,384 channels. This yielded a spectral resolution of 244 kHz [31]. The combined figures of performance for SOFIA equipped with the GREAT instrument are shown in Table 5.

Table 5. SOFIA/GREAT specifications and figures of performance. Adapted from [31], [36].

Specification	Figure of Performance
Full Spectral Range	0.890–4.75 THz
Spectral Resolution	244 kHz
Angular Field of View (FWHM)	HFA: 6.3 arcsec LFA: 14.1 arcsec 4GREAT: 10.5–52 arcsec
Angular Resolution	~6 arcsec
Noise Equivalent Power	3 × 10–20 W

2. Galactic/Extragalactic Ultra-Long-Duration Balloon Spectroscopic/ Stratospheric Terahertz Observatory (GUSTO)

The Galactic/Extragalactic Ultra-Long-Duration Balloon Spectroscopic/ Stratospheric Terahertz Observatory (GUSTO) is a NASA Explorers mission designed to make observations and spectroscopic measurements of the emission lines of OI, CII, and singly ionized nitrogen (NII) within the Milky Way and Large Magellanic Cloud (LMC) [37]. These measurements will be used to construct large-scale maps of interstellar cloud structures, thus informing scientists of the life cycle of star formation and the evolution of galactic structures. GUSTO was launched aboard a high-altitude balloon from McMurdo Station, Antarctica, on December 31, 2023. The balloon is designed to fly at an altitude of 128,000 ft (39 km) for a minimum duration of 55 days, giving GUSTO the best terrestrial-based observation window available, short of spaceflight [38]. The fully mounted instrument measures 24.5 × 15.5 × 21.5 ft with a 1,459 kg mass and is powered by a photovoltaic array and Li-Ion battery-based electrical power subsystem capable of generating 1.7 kW of electricity [39]. The average power usage of GUSTO is projected to be 1 kW during its 100% duty cycle observation period. As of 2012, the total project cost was $36.7-million.

GUSTO is equipped with a 0.9 m on-axis Cassegrain reflector telescope that focuses THz radiation on three eight-pixel arrays of heterodyne detectors [39]. The detectors utilize a QCL local oscillator and must be cooled to 4 K using a liquid helium cryostat. Each array detects one each of the OI, CII, and NII lines at 63 µm (4.75 THz), 158 µm (1.9 THz), and 205 µm (1.46 THz), respectively [37]. GUSTO's figures of performance are shown in Table 6. Equation 2 was used to solve for spectral resolution in frequency units from the given velocity units.

Table 6. GUSTO specifications and figures of performance. Source: [37].

Specification	Figure of Performance
Full Spectral Range	1.46, 1.9, 4.75 THz
Spectral Resolution	6.35–15.9 MHz
Angular Field of View (FWHM)	1 arcmin
Angular Resolution	0.65–0.9 arcmin

C. SPACE-BASED INSTRUMENTS

Space-based instruments operate in the harshest conditions of the three environments presented. Vacuum, extreme heating and cooling cycles, and radiation exposure all contribute to increased difficulties in designing and operating space systems. The requirement to launch instruments into stable orbits outside of the bulk effect of atmospheric drag and the need for instruments to be self-contained for power, propulsion, navigation, and attitude control contribute to increased costs compared to previously discussed environments. Additionally, the vast majority of spacecraft cannot be serviced once launched; therefore, the consequences of instrument or system failure are more severe. The lack of serviceability can be countered by employing redundant systems and rigorous ground-based testing of spacecraft components to various environmental conditions, contributing to increased system costs, as described in [40]. Finally, data collected by modern space-based instruments require transmission to ground stations, necessitating communications payloads aboard spacecraft. The communications architecture, originating from the spacecraft, passing through compatible ground stations, and terminating at the end user, further contributes to system and operational costs.

Despite this, space is the ideal environment for remote sensing of upper atmospheric and astronomic phenomena due to the absence of atmospheric absorption, scattering, and distortion [7]. Additionally, spacecraft have access to observations of the entire night sky and Earth, including the upper atmosphere, depending on their orbital characteristics. Spacecraft also have the unique capability of observing remote or denied areas of Earth otherwise inaccessible to ground-based and airborne systems. As a result of these advantages, there are many more space-based instruments designed to observe THz radiation than ground-based or airborne instruments. This is despite the associated increase in cost and complexity. Only Earth and atmospheric remote sensing instruments are further described as they are comparatively more relevant to the work of this thesis than the large number of astronomic observatories, like the Cosmic Background Explorer (COBE), Planck Observatory, and the Herschel Observatory.

1. Cryogenic Infrared Spectrometers and Telescopes for the Atmosphere

The Cryogenic Infrared Spectrometers and Telescopes for the Atmosphere (CRISTA) were a two-part space experiment that accomplished the first global measurements of OI concentrations in the mesosphere and lower thermosphere in the 63 μm (4.75 THz) fine line [41]. CRISTA-1 was attached to the Shuttle Pallet System (SPAS) and was deployed in 1994 from the Space Shuttle, whereafter it orbited for approximately one week in-trail of the Shuttle [42]. Following the conclusion of its mission, it was retrieved by the Space Shuttle and returned to Earth for data retrieval and processing. CRISTA-2 followed a similar mission profile in 1997, conducting a 9-day mission before Space Shuttle retrieval. Both instruments measured similar spectral ranges from approximately 4.2–75 THz. This frequency range covers emission lines from various molecules and atoms fundamental to atmospheric processes. These missions contributed to a better understanding of atmospheric dynamics, especially in the mid-altitudes from 11–185 km, and contributed to more accurate models of the atmosphere [43].

Both instruments were designed to take measurements of the atmospheric limb at various altitudes to construct a vertical profile of the atmosphere. The primary parabolic mirror aperture was 120 mm in diameter and optimized for mid-to-far-infrared reflectivity [44]. The far-infrared sensors employed on CRISTA were gallium-doped germanium (Ga-Ge) crystals, which fed a grating spectrometer. A liquid helium cryostat maintained all optical components, sensors, and spectrometers at <15K for thermal noise reduction. The complete GUSTO-SPAS spacecraft drew 76 W of average power, measured 2.98 × 1.38 × 1.38 m, and weighed approximately 1350 kg. The total cost of development and operations of each GUSTO satellite was not available at the time of writing, but as a comparison, each Shuttle flight is estimated to have cost $400-million [45]. GUSTO-2's figures of performance are shown in Table 7.

Table 7. CRISTA-2 specifications and figures of performance. Source: [43].

Specification	Figure of Performance
Full Spectral Range	4.21–74.8 THz
Spectral Resolution	~1.64 GHz
Angular Field of View	29 × 3 arcmin
Angular Resolution	3 arcmin

2. Far-infrared Outgoing Radiation Understanding and Monitoring

The Far-infrared Outgoing Radiation Understanding and Monitoring (FORUM) satellite is a future LEO instrument that will measure Earth's outgoing longwave infrared radiation (OLR) with high spectral resolution and radiometric accuracy for the first time [46]. This European Space Agency (ESA) Earth Explorer mission aims to provide a dataset enabling more accurate modeling of climate system dynamics driven by the radiative processes in the mid to upper atmosphere. In 2022, Airbus was awarded a 160-million euros ($169-million) contract to construct the FORUM satellite for a projected 2027 launch

[24]. The satellite is expected to weigh approximately 883 kg and will be inserted into an 830 km polar orbit for whole Earth coverage.

Two proposed instruments will be integrated into the FORUM satellite. The first is a traditional thermal imager sensitive to 10.5 µm (28.5 THz). The second is the primary instrument called the FORUM Sounding Instrument (FSI). FSI will be based on the Radiation Explorer in the Far-Infrared–Prototype for Applications and Development (REFIR-PAD) instrument. REFIR-PAD is a Fourier transform spectroradiometer that made multiple high-altitude balloon flights from 2005 to 2007 to measure Earth's downwelling longwave infrared radiation, similar to FIRMOS's detector and observation objectives [47]. Like FIRMOS, FORUM will employ an uncooled DLATGS pyroelectric detector sensitive to a spectral range of 6.25–100 µm (3–47.8 THz) paired to an FTS [46], [47]. Unlike FIRMOS, FORUM will employ a Mach-Zehnder interferometer with two input and output ports, one dedicated to the observation window and one to a blackbody calibration source. This scheme will allow FORUM to minimize radiometric alignment errors and optimize calibration accuracy throughout its observations to obtain very accurate radiometric measurements at high spectral resolutions [46]. The relatively complex REFIR-PAD optical path and mechanical layout, similar to FORUM's planned instrument, is shown in Figure 10. FORUM's predicted performance figures, based primarily on REFIR-PAD's performance, are shown in Table 8.

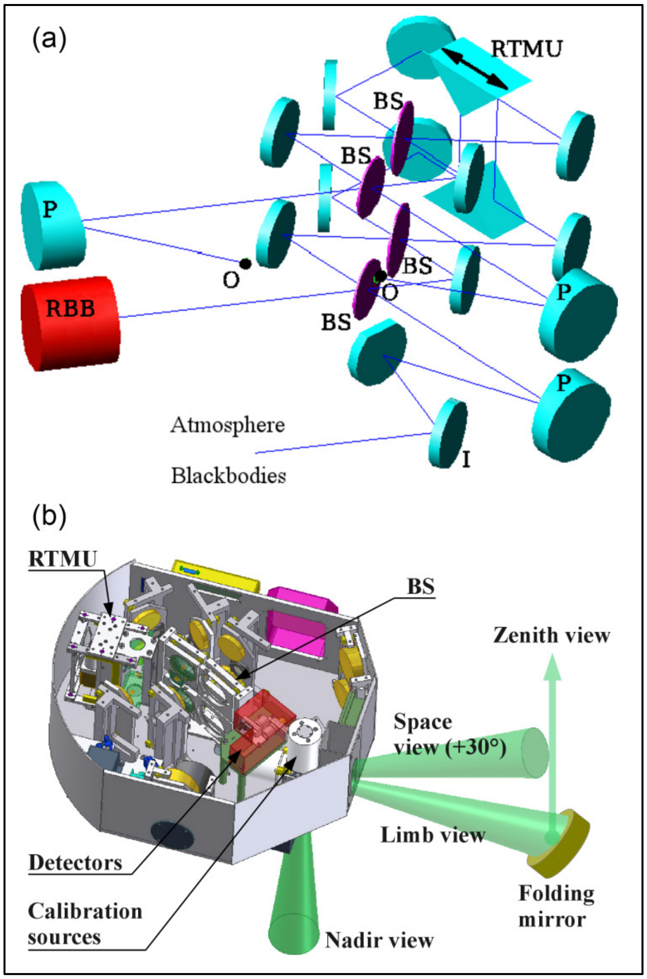

Figure 10. Depiction of REFIR-PAD’s optical (a) mechanical (b) layout. Source: [47].

Table 8. FORUM specifications and figures of performance. Adapted from [46], [47].

Specification	Figure of Performance
Full Spectral Range	3.0–47.8 THz
Spectral Resolution	150 MHz
Angular Field of View	31.1 arcmin
Angular Resolution	1.24 arcmin

D. PREVIOUS TERAHERTZ IMAGING CAMERA ITERATION

The preceding version of the TIC was developed by Naval Postgraduate School researchers and students associated with the Physics Department and Space Systems Academic Group for spaceflight aboard an Astro Digital Corvus-6U bus as part of the Mola mission. It is awaiting launch to a 500 km sun-synchronous orbit at the time of writing. The Mola TIC aims to demonstrate the application of inexpensive, simple, and low-risk 2-inch aperture THz imaging in various concept-proving Earth remote sensing and astronomic observations [48]. It aims to accomplish these objectives by utilizing a broadband THz-to-IR FPA to convert incident THz radiation to LWIR radiation. A custom video processor and computing stack will transmit captured still images via an X-Band software-defined radio (SDR) to the Mobile CubeSat Command and Control (MC3) ground station network for analysis at the NPS SSAG. The NPS SRL developed the broadband THz-to-IR FPA and a majority COTS components were utilized in the remainder of the TIC's construction, much like the current iteration documented in this thesis.

Mola was designed to carry four payloads in its 3U payload volume. This restricted the size, weight, and power allocated to the TIC. These constraints required the Mola TIC to remain within a volume defined by 10 × 68 × 170 mm dimensions. This proved to be the most significant challenge for the optical design due to the aberration characteristics inherent in short focal length optical systems [48]. Additionally, the system's total weight was required to be less than 1.11 kg due to the weight contributions of the other payloads. The power requirements of the Mola TIC are 5.5 W during use and 5 W during standby, well below the maximum continuous power of 7 W supplied by the satellite electrical power subsystem (EPS). However, due to the demanding power requirements of the X-Band SDR payload during transmission, the TIC must be powered off after every image capture sequence to allocate power to the SDR [48].

The Mola TIC's design consisted of three parts: the THz optics, the THz-to-IR FPA, and the IR optics and camera. The final design and CubeSat integration schematic are shown in Figure 11. A 2-inch polymethyl pentene (TPX$^{\text{TM}}$) aspheric lens was selected to focus broadband THz radiation on the THZ-to-IR FPA. Due to the length restrictions along the optical axis, a 35 mm back focal length (BFL) lens was selected [48]. TPX^{TM} exhibits excellent optical and mechanical properties similar to Tsurupica^{TM} (discussed further in Chapter III); however, TPX^{TM} was ultimately selected due to a lack of commercial availability of Tsurupica^{TM} in the required aperture size.

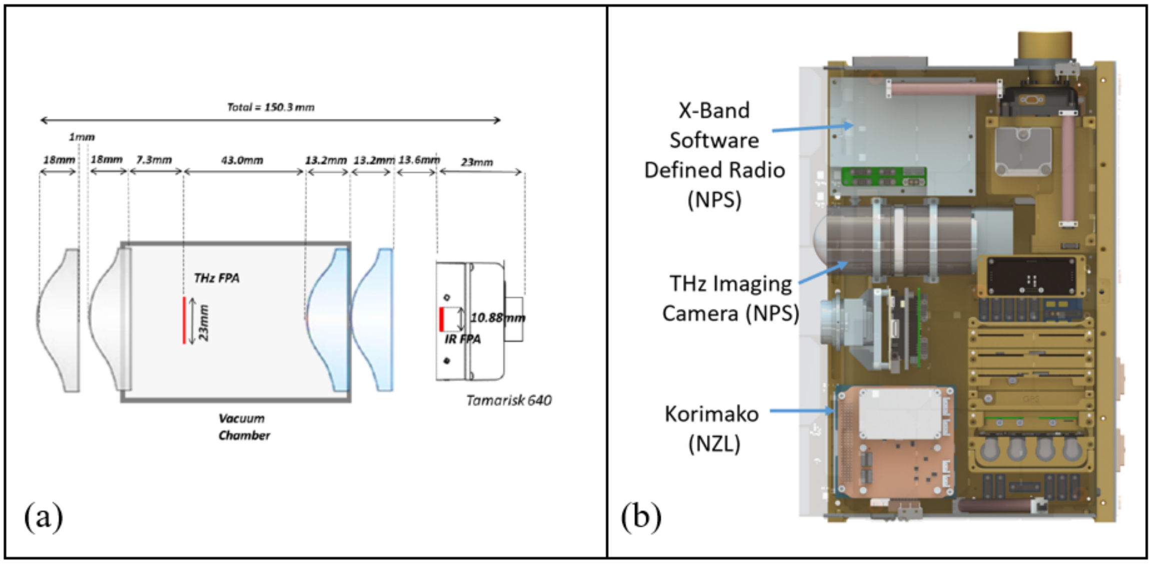

Figure 11. Final design of Mola TIC (a) and layout within Mola (b). Adapted from [48], [49].

The THz-to-IR FPA utilized in the Mola TIC is of a different design than the FPA used in this research. A broadband THz absorber was desired for the Mola mission, necessitating the use of an FPA with uniform chromium nano-film absorbing pixels. This is opposed to the current design that utilizes metamaterial THz absorbers for narrowband detection in select frequencies. The sensitivity of the broadband THz-to-IR FPA was measured to be 1.5 K/µW using temperature measurements from a FLIR SC8200 camera and power measurements from a pyroelectric THz radiation detector [48].

The IR portion of the system presented the most obvious repercussions of the compact length constraint. Two 25 mm effective focal length (EFL) germanium aspheric meniscus lenses were selected to demagnify the back of the THz-to-IR FPA onto the LWIR camera FPA at a magnification factor of –0.473. The LWIR camera used in this iteration was the Tamarisk® 640, which is sensitive to wavelengths between 8 µm and 14 µm. Winlens-3D's raytracing software was used to model the double 25 mm EFL configuration, and the spherical aberration was calculated to be 56.8 within the IR section [48]. Additional performance specifications are shown in Table 9.

Table 9. Mola TIC specifications and figures of performance. Source: [48].

Specification	Figure of Performance
Full Spectral Range	1–10 THz
Spectral Resolution	N/A
Angular Field of View (FWHM)	27° × 21°
Angular Resolution	25 arcmin
Noise Equivalent Irradiance	1.3 × 10–11 W/ cm2

E. SUMMARY

The instruments presented in this chapter are far-ranging in their complexities, detector sensitivities, spectral collection bands, sizes, weights, and costs. The single unifying factor is their overlap of collection in the THz spectrum, whether by spectroscopy or direct imaging. However, the Mola TIC stands apart in its simplicity. The use of predominantly COTS components, zero moving parts, and the lack of necessity of an active cooling mechanism and a local oscillator make it a cost-effective solution for space-based THz imaging. Chapter III presents the design of an updated and optically improved TIC driven by the requirements and constraints of a larger payload volume afforded for the project.

THIS PAGE INTENTIONALLY LEFT BLANK

III. OPTICAL SYSTEM DESIGN

A. SYSTEM DESIGN REQUIREMENTS

Requirements drive the design of systems aiming to fulfill specific mission objectives. The primary mission objective of the TIC is to demonstrate the viability of a small form factor, low-cost THz imager in low Earth orbit to identify specific emissions in the upper ionosphere with narrowband emission frequencies between 2 THz and 20 THz. Additionally, the TIC will transmit those images to a ground processing center via the NPS MC3 or other compatible ground station network. System requirements were established from the mission objective were considered in all design phases in order to realize a suitable flight unit. According to the *New SMAD* [40], system requirements quantify the approach for which the mission objective will be met. For the TIC, these include the physical characteristics of the optics and focal plane arrays, which are the topics of this thesis. The FPAs must be capable of capturing phenomena of interest in their emitted electromagnetic frequencies, whereas the optical characteristics must meet the field of view, focus, magnification, and aberration requirements. System requirements also take into account constraints imposed by the size, weight, and power limitations of the spacecraft, as well as the environmental conditions of launch and low Earth orbit [40]. The environmental conditions include operation in vacuum, thermal swing, vibration, and gravitational load tolerance. As the THz imager is part of a proof-of-concept mission, many of the specific mission requirements are broadly defined. This results in flexible system and design requirements that achieve the broader mission requirements.

This thesis focused on the optical design of the TIC and therefore, the mission and system requirements applicable to the optical design and overall configuration were considered. Environmental factors were not explicitly considered in the design requirements; however, many of the components and design principles used in the design of this iteration are common to the Mola TIC, which has successfully passed thermal, vacuum, and vibration testing to NASA General Environmental Verification Standards (GEVS) [48]. Usage of common components and design principles gives a reasonable expectation that this iteration will also meet environmental-factors driven requirements. Nevertheless, testing will be required to NASA GEVS prior to launch into orbit.

B. OPTICAL SYSTEM DESIGN

The design of the TIC is split into two distinct sections: the THz section and the IR section. The THz section was designed to collect radiation from targets of interest sufficiently far away to act as an infinite source. The parallel light rays are then focused by either a lens or a mirror onto the THz-to-IR FPA. While refractive optics exhibit a high transmittance in the THz range of interest (>60%), reflective optics should exhibit a significantly higher reflectance in the same range (>99%). Upon focalization by the lens or mirror, THz radiation incident on the FPA is absorbed and converted to heat. The THz section must also filter or block any infrared radiation from entering the TIC as this will heat the THz-to-IR FPA, introducing thermal noise into the system. A representative illustration of a lens and a mirror design are shown in Figures 12 and 13, respectively.

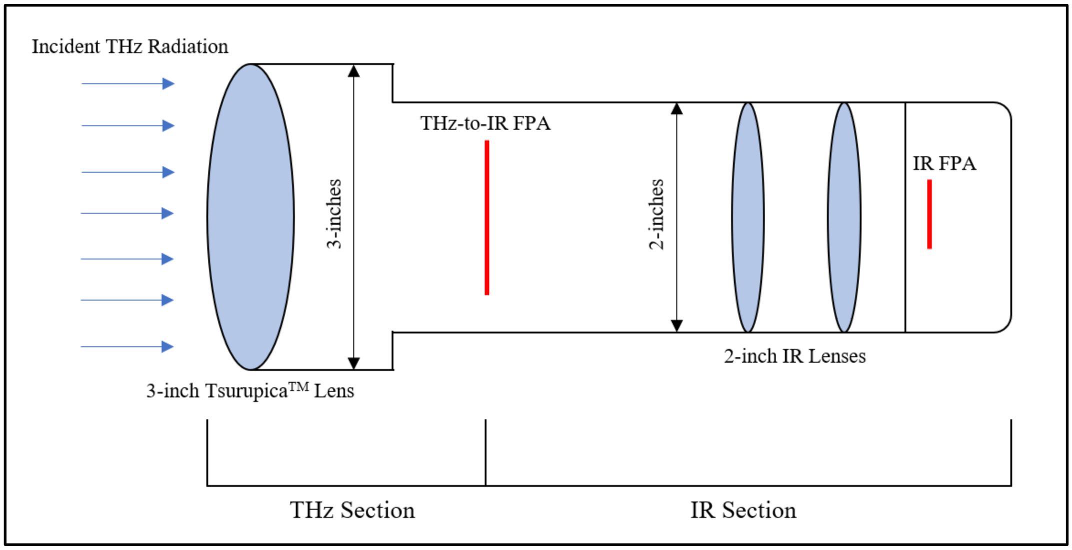

This representative design utilizes a 3-inch primary lens to focus incident THz radiation on the THz-to-IR FPA and two 2-inch lenses to focus the back of the THz FPA onto the IR FPA. The delineation between the THz section and IR section are shown.

Figure 12. Representative lens design.

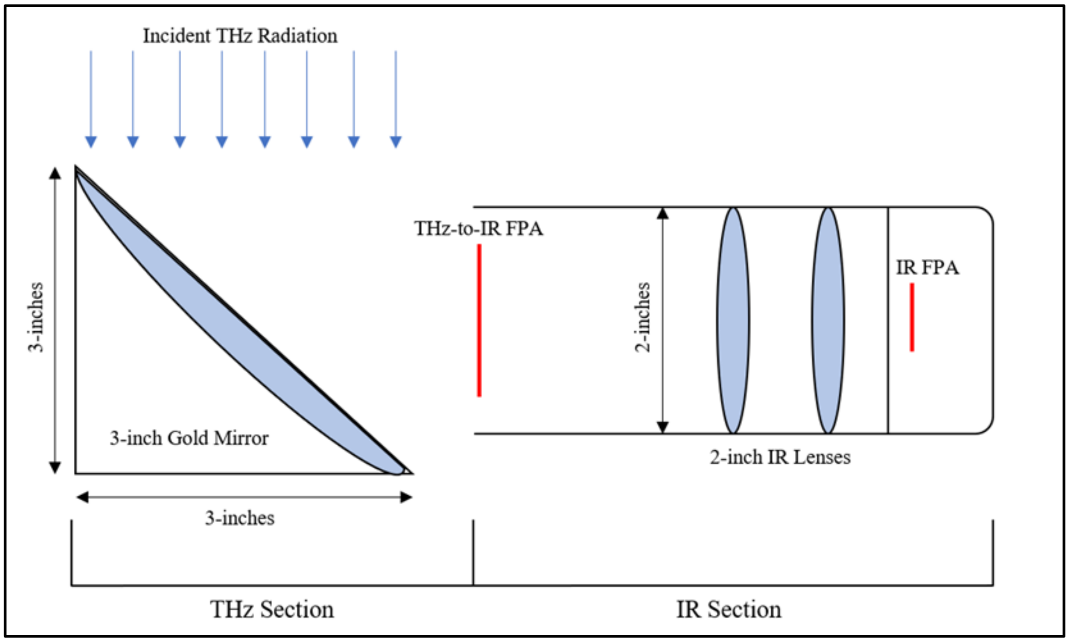

This representative design utilizes a 3-inch primary mirror to focus incident THz radiation on the THz-to-IR FPA. The representative IR section remains unchanged from Figure 12.

Figure 13. Representative mirror design.

The IR section was designed to focus the backside of the THz-to-IR FPA onto a COTS LWIR camera. Because the THz-to-IR FPA is, in this particular case, larger than the LWIR camera FPA, the IR optics should demagnify the image of the THz-to-IR FPA to fit onto the LWIR camera FPA. The LWIR camera must also be sensitive to the prominent output frequency range of the THz-to-IR FPA. Research on the emission frequencies of the THz-to-IR FPA conducted by [12] and [13] has shown that peak emission occurs between approximately 7 µm and 20 µm, and 7 µm and 14 µm, respectively. The differences in these frequency bands were due to variations in the materials used in the fabrication of the THz-to-IR FPA.

C. TERAHERTZ OPTICAL DESIGN

The THz section of the imager consists of a 3-inch primary aperture. 3-inches is a standard commercially available aperture diameter in which a variety of lenses and mirrors are available. Additionally, 3-inches is the maximum diameter that fits within the 6U form factor, accounting for additional volume for mounts. Increasing the aperture from the 2-

inch diameter employed in the Mola TIC to 3-inches increases the light gathering area by 225%. Both lenses and mirrors were considered for the primary optics.

1. Materials

Several candidate materials were considered for the THz optics based on their transmissibility or reflectivity in THz frequencies and availability for purchase on the commercial market. It was also critical that either the primary optics itself, or a filter, prevent infrared radiation from reaching the THz-to-IR FPA. The candidate materials and their applicable properties are summarized in Table 10.

Table 10. Candidate optics types, materials, geometry, and properties. Adapted from [50], [51], [52].

Material	Optics Type	Surface Geometry	Properties
Tsurupica^{TM}/ Picarin	Lens	Plano Convex	High transmissibility in THz and visible frequencies. Opaque in IR wavelengths.
High-Density Polyethylene (HDPE)	Lens	Plano Convex	Moderate transmissibility in THz and IR frequencies.
Gold Plated Aluminum	Mirror	90°-Fold Parabolic	Highly reflective in all wavelengths greater than 2μm. Does not filter IR.

Tsurupica^{TM}, also known as Picarin, is a proprietary optical material developed by the Japanese research institute, RIKEN. It is highly transmissible in THz and visible spectra and highly opaque in the IR spectrum [50]. The refractive indices for both THz and visible spectra are nearly identical at 1.52 [5]. This polymer-based material is also mechanically strong enough to withstand polishing, aiding in the transmission of visible light, which allows the use of visible light or lasers to position and align the lenses. 3-inch diameter 50 mm EFL aspheric plano-convex Tsurupica^{TM} lenses were procured from RIKEN for use in the THz section of the imager [50]. Both sides of the lens are rough polished to allow for minimal distortion of transmitted visible wavelengths. Surface polishing does not affect THz transmissibility [50].

High-Density Polyethylene (HDPE) is a polymer that is commercially available in a variety of lens sizes and focal lengths. The refractive index in THz frequencies is 1.53, similar to that of Tsurupica^{TM}; however, HDPE exhibits lower transmissibility than Tsurupica^{TM} in THz frequencies of interest, as shown in Figure 14. In addition, HDPE has a strong absorption lattice mode at 2.2 ± 0.2 THz, making it more difficult to use for applications at those frequencies [5]. A single 2-inch 35 mm back focal length HDPE lens was available for tests in the THz section.

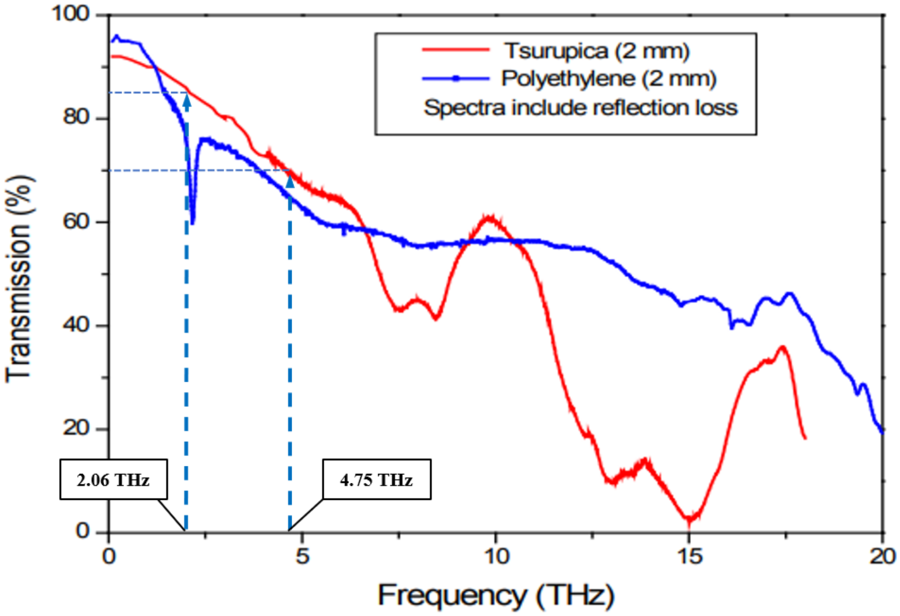

Percent transmission of radiation from 0–20 THz through 2 mm of Tsurupica^{TM} (red) and polyethylene (blue). Polyethylene lattice mode absorption at 2.2 THz is shown.

Figure 14. Transmission of THz frequencies through 2 mm of material. Adapted from [51].

A protected gold-plated aluminum mirror was also considered for the primary aperture optics. The reflectivity of gold plating is above 99% in the frequencies of interest, making it an ideal candidate for THz remote sensing applications [52]. "Protected" coatings refer to the application of a thin layer of SiO_2, and provides resistance to corrosion and abrasion. A parabolic mirror was preferred and a variety are commercially available in 3-inch diameters and varying focal lengths. A parabolic mirror is ideal for focusing collimated light from a far distant source to a point. However, for traditional parabolic mirrors the focal point is along the optical axis. This necessitates the use of a sensor or secondary mirror along the optical axis, which blocks a portion of the incident light. Therefore, a 90°-fold parabolic mirror was considered. This design creates a 90° bend in the optical axis of the system, which was taken into account when fitting the system in a 6U CubeSat bus. The procured 3-inch mirror, manufactured by Edmund Optics Inc., has an EFL of 50.8 mm. It measures 83.82 mm along its longest axis, as shown in Figure 15, allowing it to fit within the most constraining axis of the 6U bus's payload compartment [53], [54]. Sizing considerations are further discussed later in this chapter.

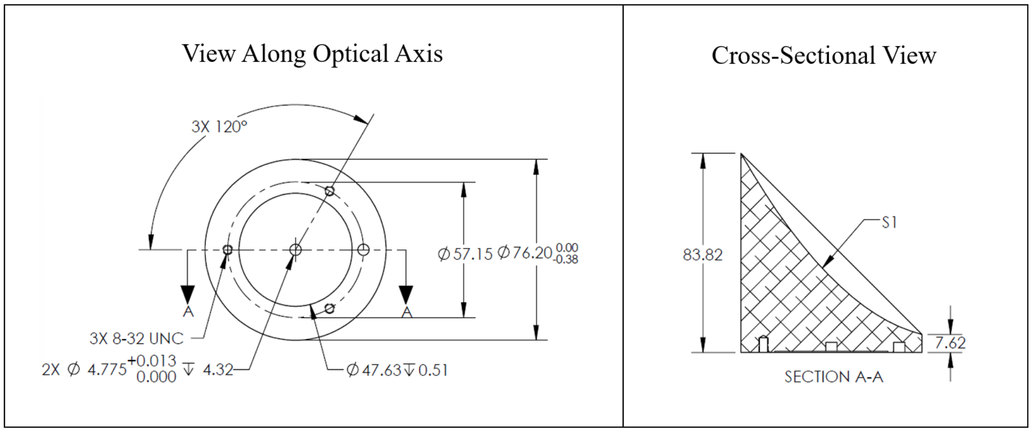
View Along Optical Axis

Cross-Sectional View

Left figure shows the face of the mirror and associated measurements (mm). The right figure shows the profile view and cross-sectional curvature of the mirror.

Figure 15. Gold-plated mirror diagram. Adapted from [53].

A consequence of utilizing a gold-coated mirror is the necessity of an IR filtering element due to its wideband reflectivity. According to Edmund Optics Inc. specifications [53], the reflectivity of the mirror in IR wavelengths is >98%; therefore, a filter was required to be placed in the optical path to prevent infrared radiation from being focused on the THz-to-IR FPA. Two filters were considered for this purpose. The first was a 2-inch diameter, 4 mm thick Tsurupica^{TM} window. Given the ~70% transmission per 2 mm of material (see Figure 14), approximately 50% of incident THz radiation and <4% of infrared radiation passes through the 4 mm window [50]. The second filter considered was a copper multi-mesh filter manufactured by QMC Instruments Ltd. This multi-mesh filter exhibits good transmission in THz frequencies (90% at 4.7 THz) and exceptional blocking of IR (< .1% transmission), as shown in Figure 16.

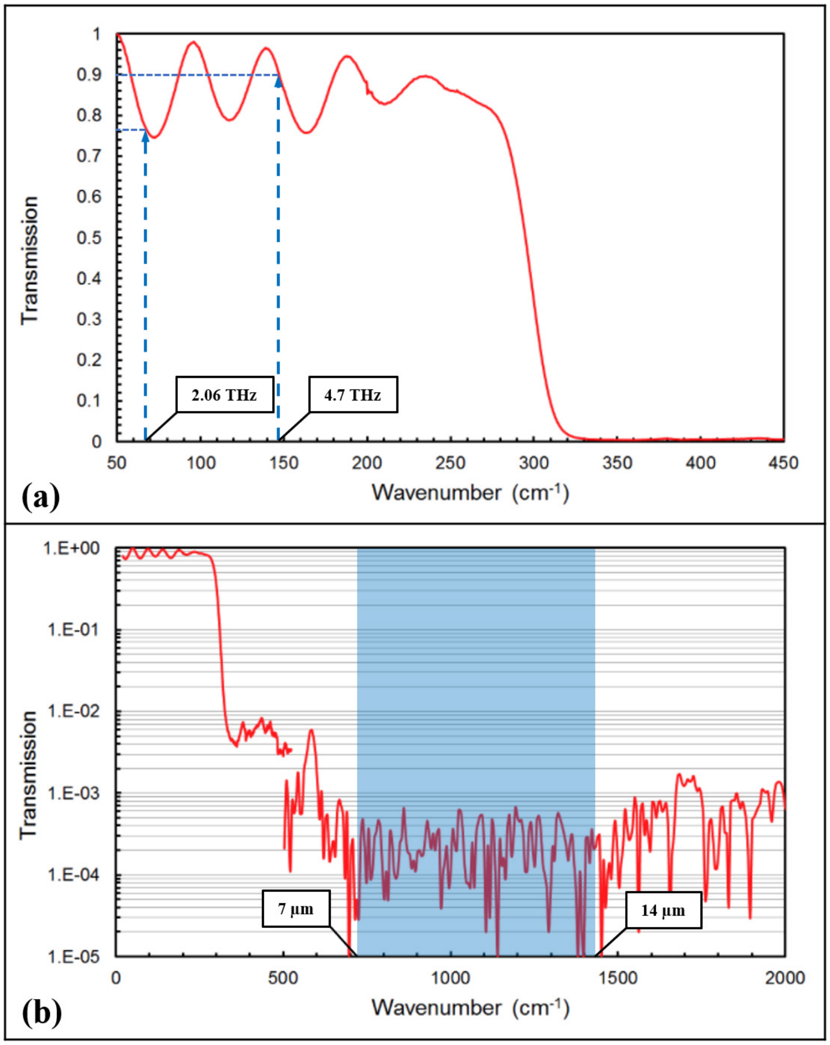

Transmission of THz radiation through a copper mesh filter are shown in (a). The blue lines indicate the frequencies corresponding to the absorption frequencies of the THz-to-IR FPA and emission frequency of the QCL. Transmission in the IR spectrum is shown in (b). The blue shaded area indicates the sensitivity waveband of the LWIR camera.

Figure 16. Transmission of THz and IR through a cooper mesh filter. Adapted from [55].

2. Field of View

The angular field of view (AFOV) of the TIC is the angular dimensions of the scene visible to the THz-to-IR FPA. The AFOV defines the extent of the atmosphere which can be viewed at an instantaneous moment, as shown in Figure 17, and is calculated using Equations 3 and 4.

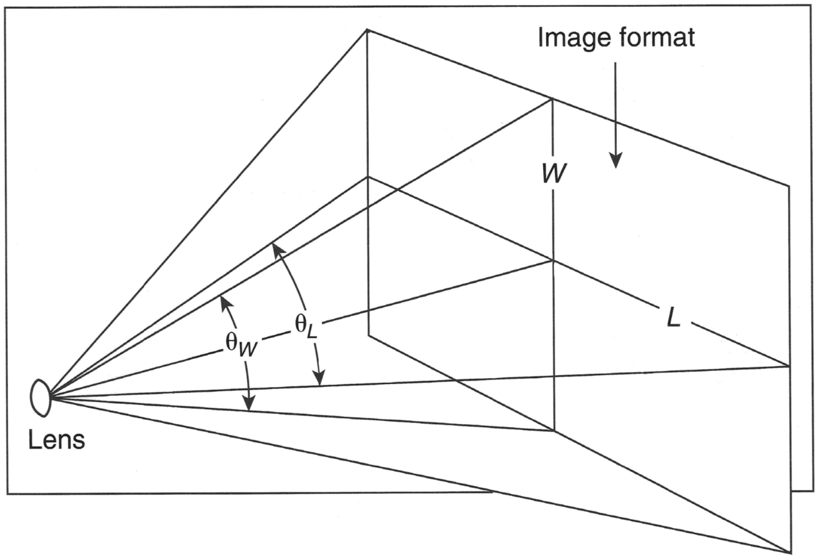

Figure 17. AFOV, θ_L and θ_W, of an FPA with dimensions L by W. Adapted from [4].

$$\theta_L = 2 \cdot \tan^{-1}\left(\frac{L}{2f}\right) \tag{3}$$

$$\theta_W = 2 \cdot \tan^{-1}\left(\frac{W}{2f}\right) \tag{4}$$

where θ_L and θ_W are the angular fields of view along the corresponding axis of the image, L and W are the dimensions of the sensor, and f is the focal length of the primary lens or mirror. Using the dimensions of the THz-to-IR FPA (21.25 mm by 16.1 mm) and a 50.8 mm effective focal length for the primary aperture gives an angular field of view of 23.6° by 18.0°.

The AFOV can be used to find the physical dimensions of the scene when the distance from the object to be imaged is defined, as shown in Figure 18, and is calculated using Equations 5 and 6.

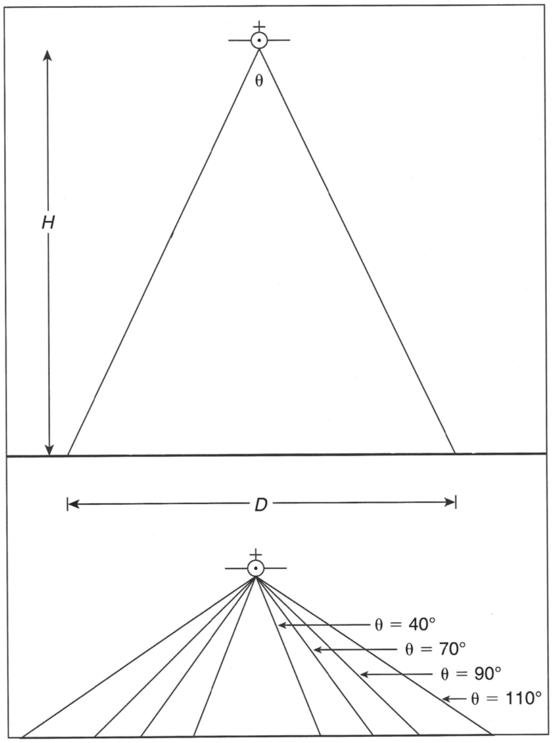

Figure 18. Physical scene dimension, *D*, corresponding to AFOV, *θ*, and height, *H*, above a target scene. Adapted from [4].

$$D_L = 2 \cdot H \cdot \tan\left(\frac{\theta_L}{2}\right) \tag{5}$$

$$D_W = 2 \cdot H \cdot \tan\left(\frac{\theta_W}{2}\right) \tag{6}$$

where D is the one-dimensional distance of the scene along the specified axis, H is the distance between the scene and imager, and θ is the angular field of view along the specified axis. The TIC will be flying at an altitude of 500 km from Earth's surface and will be targeting phenomena in the upper ionosphere, which extends from approximately

100 to 300 km altitude. Therefore, the distance from the TIC to the scene that will be imaged ranges from 200 km to 400 km. The target scene altitude limits are defined from 100 km to 400 km to demonstrate the extreme bounds of possible observations. The scene dimensions for various altitudes are shown in Table 11.

3. Resolution

The resolution is the distance between two separate points in an image which can be resolved to be distinct from one another. Resolution is the most common indicator of the level of detail contained in an image. Every imaging system has a theoretical maximum resolution it is capable of producing as dictated by the Rayleigh criterion for the diffraction limit. The diffraction limit can be solved for the angular limit or spatial limit, given by Equations 7 and 8, respectively [7].

$$\Delta \varphi_R = 1.22\left(\frac{\lambda}{d}\right) \tag{7}$$

$$\Delta x_R = 1.22\left(\frac{\lambda}{d}\right)H \tag{8}$$

where $\Delta\varphi_R$ is the minimum angle and Δx_R is the minimum distance between two separate objects which can be distinctly resolved, λ is the radiation wavelength, d is the diameter of the primary aperture, and H is the distance from the imager to the object. Using Equation 7, the angular diffraction limits for 2.06 THz and 4.75 THz frequencies using 3-inch optics are 8.37 arcsec and 3.63 arcsec, respectively. The spatial diffraction limit varies with distance from the object being imaged. These are shown for a variety of distances in Table 11.

The actual resolution of the imager is dependent on the number of pixels within the THz-to-IR FPA and the FPA's dimensions, and can be calculated for angular resolution and spatial resolution using Equations 9 and 10, respectively.

$$\Delta \varphi_A = \frac{\theta}{n} \tag{9}$$

$$\Delta x_A = \frac{D}{n} \tag{10}$$

where $\Delta\varphi_A$ is the angular resolution along a specified axis, θ is the angular dimension of the scene along the same axis, Δx_A is the spatial resolution along a specified axis, D is the linear dimension of the scene along the same axis, and n is the number of pixels the sensor contains along the same axis. The angular resolution of the TIC is 21.6 arcmin. The spatial resolution is dependent on the distance from the target and is shown in Table 11 for a variety of distances. A comparison of target scene dimensions, actual spatial resolution, and Rayleigh criterion diffraction-limited spatial resolution for various scene altitudes are shown in Table 11.

Table 11. Scene dimensions, spatial resolutions, and spatial diffraction limits.

Scene Altitude MSL	**Scene-to-Imager Distance**	**Scene Dimensions (km)**	**Spatial Resolution (km)**	**2.06 THz Diffraction Limit (km)**	**4.75 THz Diffraction Limit (km)**
100 km	400 km	167 × 127	2.5	0.93	0.40
150 km	350 km	146 × 111	2.2	0.81	0.35
200 km	300 km	125 × 95	1.9	0.70	0.30
250 km	250 km	104 × 79	1.6	0.58	0.25
300 km	200 km	83 × 63	1.3	0.47	0.20
350 km	150 km	63 × 48	0.9	0.35	0.15
400 km	100 km	42 × 32	0.6	0.23	0.10

According to these results, in no case does the actual resolution of the imager outperform the Rayleigh diffraction limit. For a frequency of 2.06 THz, the best achievable spatial resolution is 2.7 times larger than the spatial diffraction limit. For a frequency of 4.75 THz, the best achievable spatial resolution increases greatly to 6.3 times the spatial diffraction limit. In very well-designed systems, the actual resolution of the system matches the diffraction limit, as the optics of the system are performing at the peak of their theoretical capability [7]. In the case of the TIC, the use of a relatively short focal length, wide FOV, and limited number of pixels within the THz-to-IR FPA result in underperformance from the theoretical resolution limit.

D. INFRARED OPTICAL DESIGN

The IR portion of the TIC utilizes a 2-inch aperture based on standard 2-inch optical tubing widely available on the commercial market. 2-inch optics were chosen in the IR portion of the imager for several reasons. First, the previous iteration of the TIC utilized 2-inch aperture optics in which several custom fabricated pieces were produced. The custom fabricated pieces consisted of the bracket to house the THz-to-IR FPA and a shortened mount for the COTS LWIR camera, discussed later in this section. Second, 2-inch aperture IR optics are more commercially available in a variety of substrate materials and focal lengths. Third, due to the necessity of the short focal lengths involved, a larger aperture does not offer any benefits, as the light gathering ability of larger optics would come at the expense of an increase in aberration and distortion for a fixed focal length.

1. Materials

Anti-reflective coated germanium (Ge) aspheric meniscus lenses were chosen as the optical component for the IR section. Germanium substrate lenses layered with anti-reflective coatings exhibit high transmissibility in the LWIR wavelength band emitted by the THz-to-IR FPA, as shown in Figure 19.

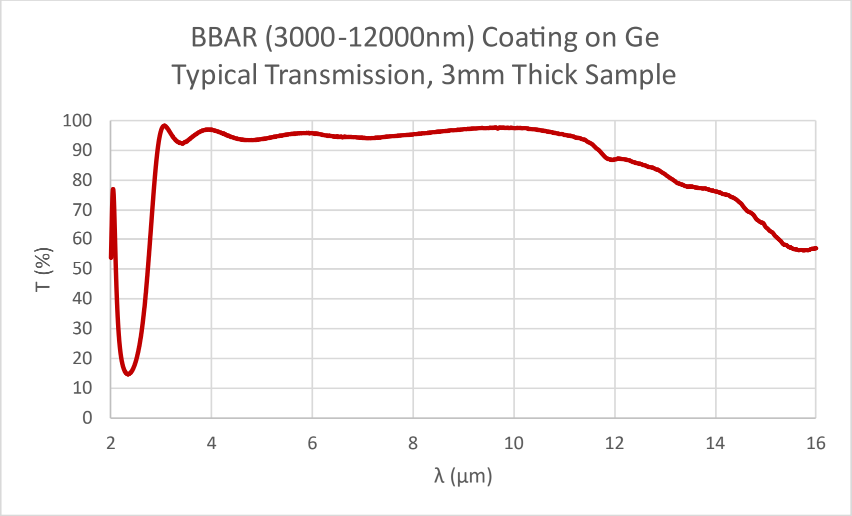

Figure 19. Optical transmission of 2–16 µm infrared radiation through 3 mm coated Ge Lens. Source: [56].

Additionally, a meniscus design is ideal for germanium substrates, as it allows for shaping both surfaces of the lens with aspheric curves. This reduces spherical aberration caused by the high index of refraction of germanium of 4.003 [57]. One disadvantage of utilizing germanium substates is that the index of refraction changes with variations in temperature more than other substrate materials (e.g., zinc selenide). The change in refractive index with temperature for germanium is 396×10^{-6} °C^{-1} [57]. For zinc selenide, this change in refractive index is 61×10^{-6} °C^{-1}. Brave [48] modeled a thermal analysis for the Mola TIC in a 500 km sun-synchronous orbit and found the range of internal temperatures would likely be between 33 and 88 °C. This equates to a change in index of refraction of 0.02178 for the most extreme temperature gradient, a 0.05% difference from the baseline index of 4.003. This small change will likely not cause any distortion in the IR images.

2. Focus and Demagnification

Due to the difference in physical dimensions between the THz-to-IR FPA and LWIR camera's FPA, a demagnification of the THz-to-IR FPA was necessary to project it in the correct size onto the LWIR camera's FPA. The amount of magnification depends on the size of the object, in this case the THz-to-IR FPA, and the image, in this case the LWIR camera's FPA. The magnification is the ratio of the image size to the object size and is calculated using Equation 9 [58].

$$M = \frac{r_{image}}{r_{object}} \tag{9}$$

where M is the magnification factor, r_{image} is the size of the image, and r_{object} is the size of the object. Given the dimensions of the THz-to-IR FPA of 21.25 mm by 16.1 mm, and the LWIR camera's FPA dimensions of 10.88 mm by 8.16 mm, the magnification factors are 0.512 and 0.507, respectively. A magnification of 0.507 was used in the modeling of the IR section as it is the most constraining magnification.

3. Camera

The Tamarisk® 640 is an uncooled LWIR VO_x microbolometer camera manufactured by Sierra-Olympia Technologies Inc., and was selected as the IR capturing device for the TIC.

This is the same camera that is used in the TIC developed for Mola [48]. A custom housing for the camera was fabricated as part of the development of the Mola TIC and was used in this iteration as well. The custom housing reduces the distance between the LWIR camera's FPA and lens tube threading, allowing for placement of lenses closer to the LWIR camera. In addition, the custom housing provides an interface with standard 2-inch optical tubing, which the IR section of the TIC was constructed of. The LWIR camera's commercially available mounting options do not include mating to standard 2-inch optical tubes. The custom housing is shown next to the manufacturer's housing in Figure 20. By requirement, the Tamarisk® 640 is sensitive to the wavelengths that the THz-to-IR FPA emits in. The THz-to-IR FPA emits LWIR radiation from 7 µm to 14 µm and according to Sierra-Olympia Technologies, Inc. [59], the LWIR camera's spectral band covers 8 µm to 14 µm, as shown in Figure 21. The Tamarisk® 640 is capable of detecting noise equivalent temperature differences (NETD) of less than 50 mK and is represented as a change in contrast in the grayscale video output [59].

Manufacturer's Mount **Custom Mount**

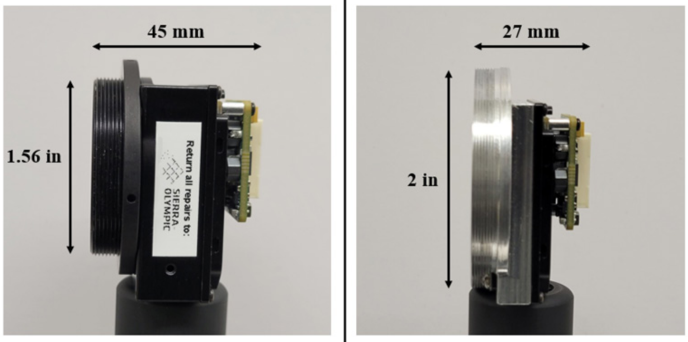

Manufacturer's Mount **Custom Mount**

Figure 20. Tamarisk® 640 LWIR camera with manufacturer's housing (left) and custom housing (right).

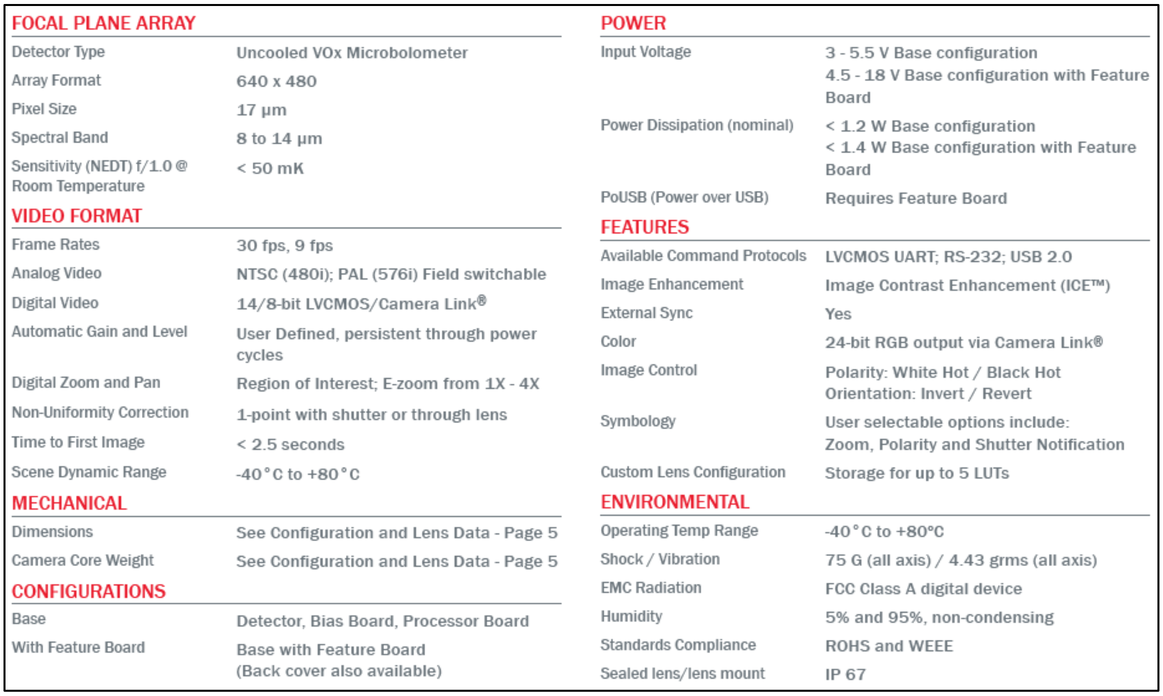

FOCAL PLANE ARRAY

Detector Type	Uncooled VOx Microbolometer
Array Format	640 x 480
Pixel Size	17 µm
Spectral Band	8 to 14 µm
Sensitivity (NEDT) f/1.0 @ Room Temperature	< 50 mK

VIDEO FORMAT

Frame Rates	30 fps, 9 fps
Analog Video	NTSC (480i); PAL (576i) Field switchable
Digital Video	14/8-bit LVCMOS/Camera Link®
Automatic Gain and Level	User Defined, persistent through power cycles
Digital Zoom and Pan	Region of Interest; E-zoom from 1X - 4X
Non-Uniformity Correction	1-point with shutter or through lens
Time to First Image	< 2.5 seconds
Scene Dynamic Range	-40 °C to +80 °C

MECHANICAL

Dimensions	See Configuration and Lens Data - Page 5
Camera Core Weight	See Configuration and Lens Data - Page 5

CONFIGURATIONS

Base	Detector, Bias Board, Processor Board
With Feature Board	Base with Feature Board (Back cover also available)

POWER

Input Voltage	3 - 5.5 V Base configuration 4.5 - 18 V Base configuration with Feature Board
Power Dissipation (nominal)	< 1.2 W Base configuration < 1.4 W Base configuration with Feature Board
PoUSB (Power over USB)	Requires Feature Board

FEATURES

Available Command Protocols	LVCMOS UART; RS-232; USB 2.0
Image Enhancement	Image Contrast Enhancement (ICE™)
External Sync	Yes
Color	24-bit RGB output via Camera Link®
Image Control	Polarity: White Hot / Black Hot Orientation: Invert / Revert
Symbology	User selectable options include: Zoom, Polarity and Shutter Notification
Custom Lens Configuration	Storage for up to 5 LUTs

ENVIRONMENTAL

Operating Temp Range	-40 °C to +80°C
Shock / Vibration	75 G (all axis) / 4.43 grms (all axis)
EMC Radiation	FCC Class A digital device
Humidity	5% and 95%, non-condensing
Standards Compliance	ROHS and WEEE
Sealed lens/lens mount	IP 67

Figure 21. Tamarisk® 640 system features. Source: [59].

There are three primary modes operation for the camera: auto gain control, image contrast enhancement, and manual. All three modes are selectable within the camera's proprietary control software developed by Leonardo DRS. The auto gain control mode dynamically adjusts the gain and level settings of the camera as the scene changes in order to display the maximum contrast, given the temperature range of the entire scene. The image contrast enhancement setting functions similarly to the auto gain setting, except that it creates localized areas within the image and independently adjusts the gain and level settings in those zones [60]. The manual gain and level mode allows the user to adjust both of these settings to much finer detail. In addition to the gain settings, zoom levels between 1x and 4x are available in 0.25x increments. When an image is zoomed to greater than 1x power, users have the ability to slew the output image to adjust the image boundaries.

4. Optical System Configurations

WinLens-3D raytracing software was utilized to model the IR section. WinLens-3D is a mathematics-based computer program that allows users to model various user-defined lenses and optical systems and evaluate their characteristics, including magnification, aberration, and distortion [61]. There are, however, limitations to the WinLens-3D program. Aberration and distortion results are only valid for systems that utilize a straight-line optical axis. This makes it non-ideal for modeling bending elements, like the 90°-fold parabolic mirror. Additionally, as the radius of curvature and aspheric coefficients of the 3-inch Tsurupica™ lens were not available, it could not be modeled within the program. Therefore, WinLens-3D was not used to model the THz section. Consequently, the design of the THz section was conducted with actual lens and mirror hardware in the Sensor Research Lab by experiment. The experimental design of the THz section is further discussed in Chapter IV. WinLens-3D did, however, provide valuable estimations of ideal lens placements, aberration, and distortion characteristics within the IR section. Optical bench testing was then performed using the modeled configurations before selecting the final IR section design, further discussed in Chapter IV.

A variety of configurations were modeled in WinLens-3D using both 25 and 50 mm EFL Ge lenses, manufactured by Edmund Optics Inc. These configurations included both single and double lens designs in a variety of placements and separations. Additionally, both forward and reverse concavity placements of each lens were modeled. For the single and double 50 mm EFL lenses, additional models were evaluated with an added 1.25x zoom factor. This is the lowest zoom setting the Tamarisk® 640 camera is capable of, using its propriety software. The 1.25x zoom factor was evaluated due to the likelihood that inexact machining and alignment of the IR optical system would produce off-centered images of the THz-to-IR FPA. Misalignment would result in segments of the THz-to-IR FPA being outside the bounds of the captured image at the 1x zoom setting. The ability to slew images to center the THz-to-IR FPA in the full field of view is attained when employing a zoom setting greater than 1x, should any misalignments occur.

Figures 22 – 27 show models of various configuration and their optical characteristics. The upper left quadrant shows a graphical representation of the object plane, lens configuration, and image plane. The entrance pupil, denoted with a red "E," was fixed at a 40 mm diameter for all configurations. The upper right quadrant shows the maximum and total aberration, coma, and distortion present in the system. The number(s) annotated above the bar graph show the contribution of individual lens elements to total system aberration, coma, and distortion. The lower right quadrant is a graphical depiction of the image distortion over the full plane of the image. The dotted square represents an ideal zero-distortion image and the solid line represents the actual distortion of the image due to the optical design. The lower left quadrant is a full-field spot diagram showing the effects of distortion, aberration, coma, and astigmatism on the image due to the optical design. An ideal optical system would show singular dots with a diameter of the airy disk in all blocks of the field. The data for each modeled configuration for IR section length (measured from the THz-to-IR FPA to the LWIR FPA), aberration, coma, and distortion are consolidated in Table 12.

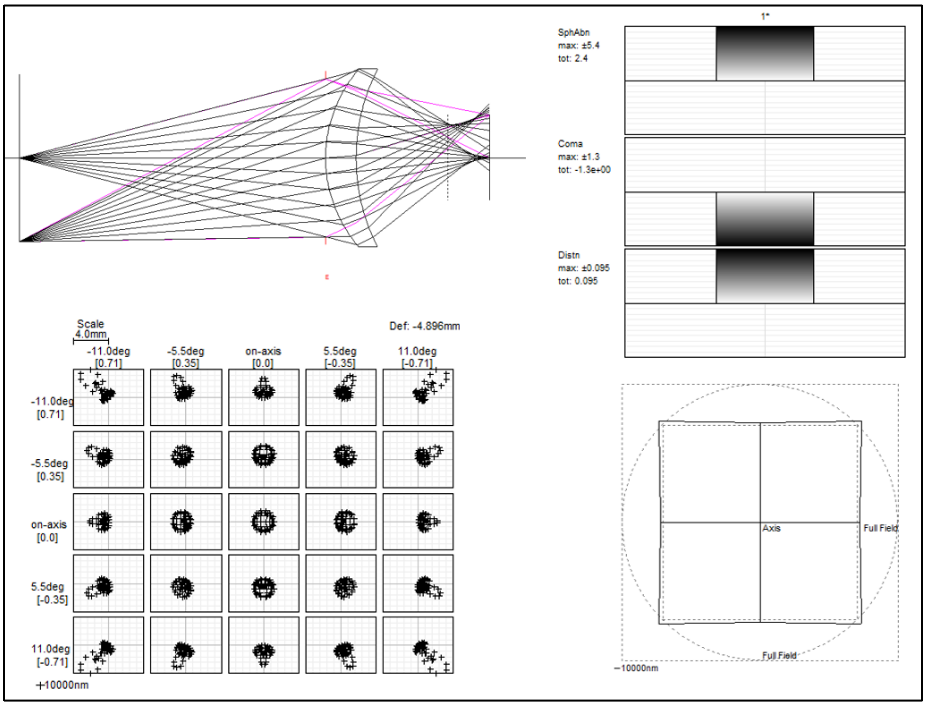

Figure 22. Single 2-inch 25 mm EFL lens.

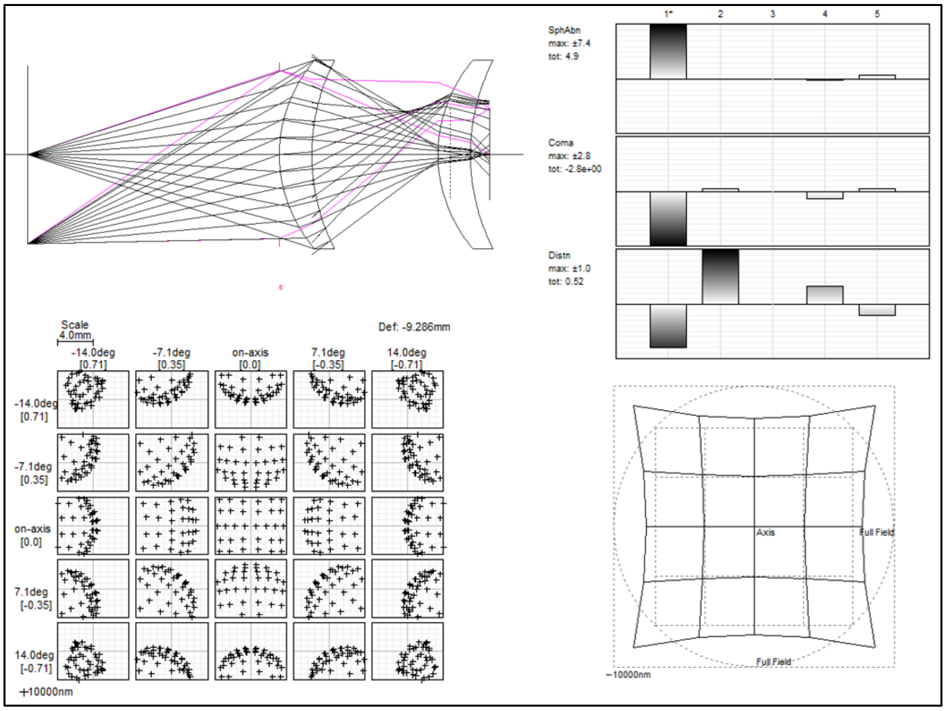

Figure 23. Double 2-inch 25 mm EFL lenses.

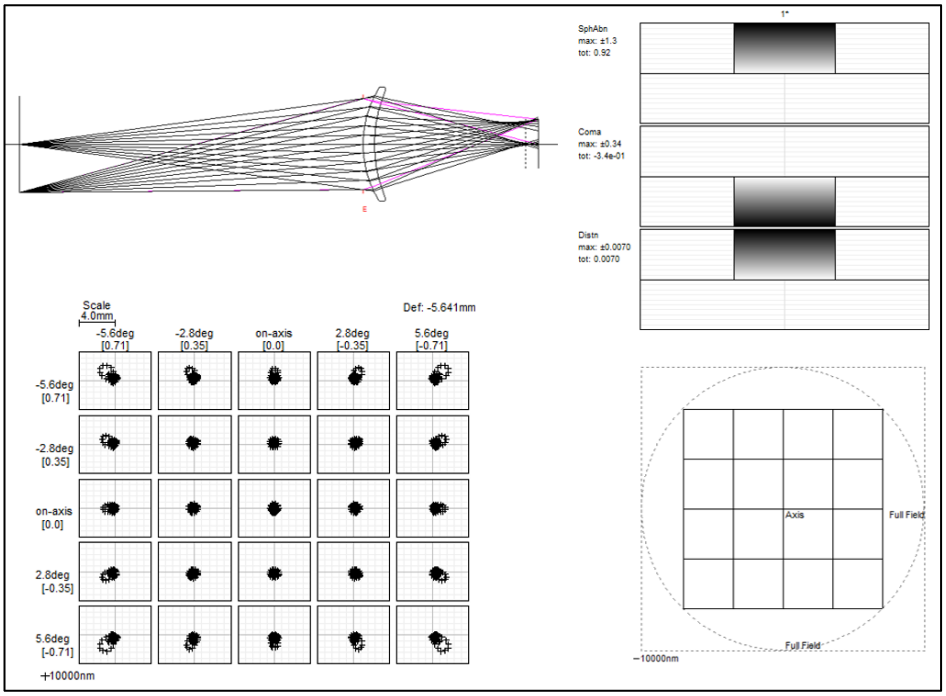

Figure 24. Single 2-inch 50 mm EFL lens.

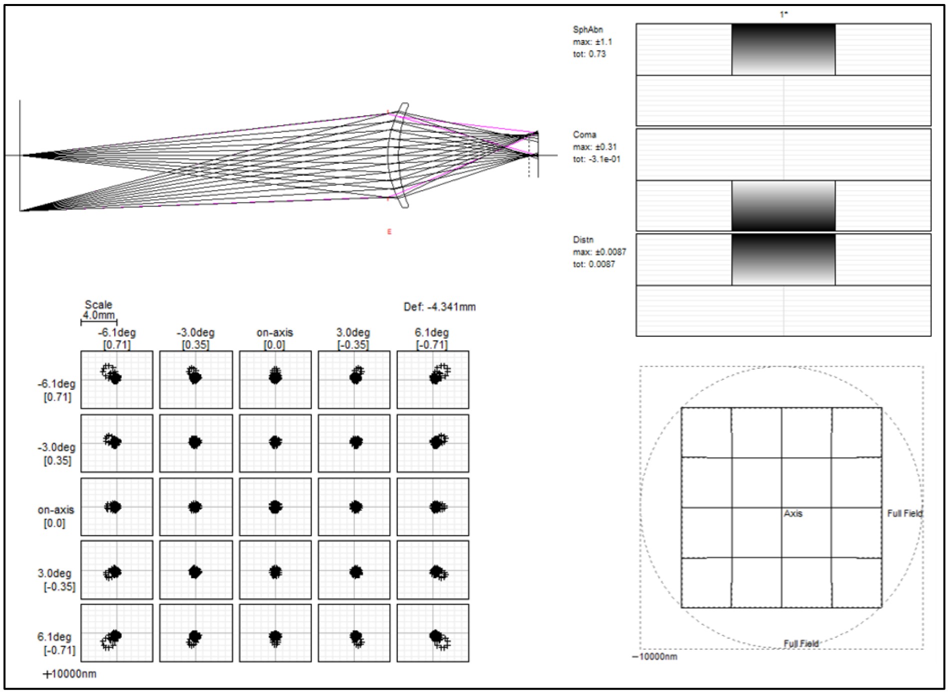

Figure 25. Single 2-inch 50 mm EFL lens at 1.25x zoom.

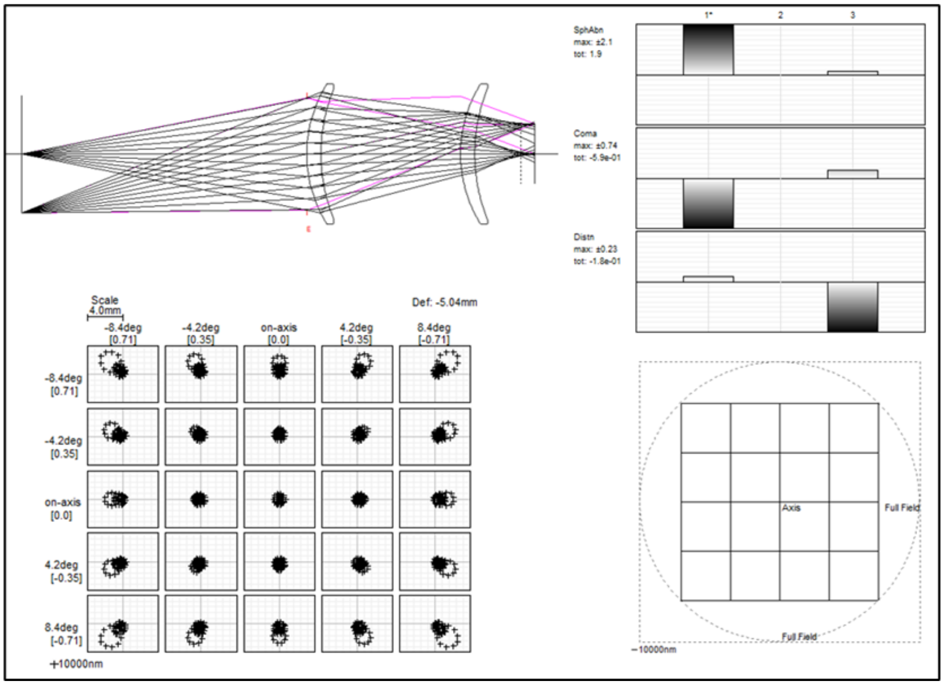

Figure 26. Double 2-inch 50mm EFL lenses.

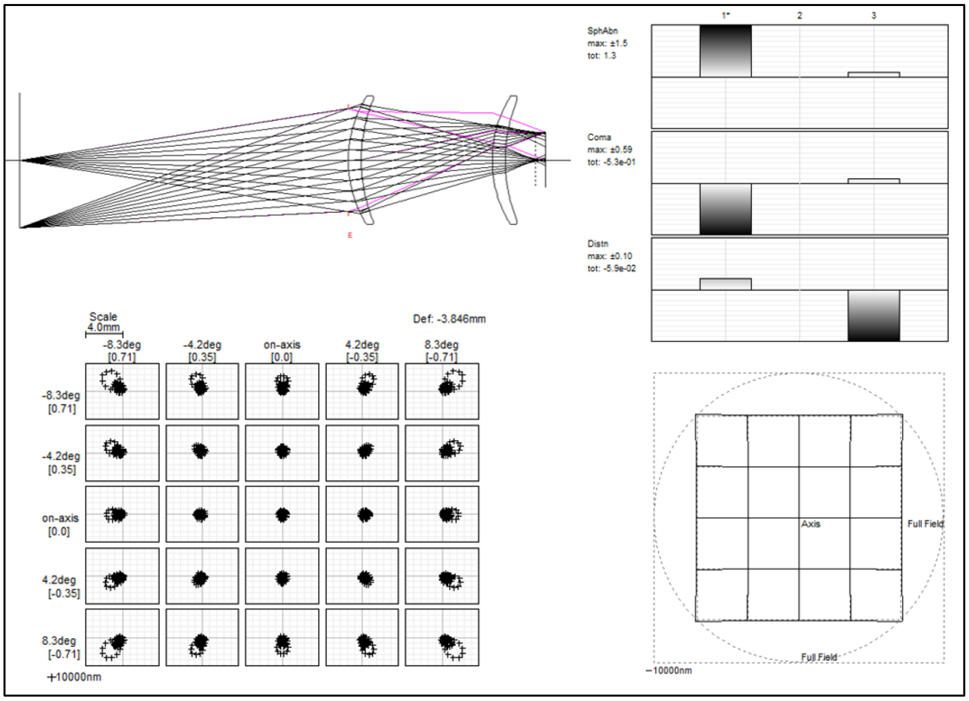

Figure 27. Double 2-inch 50mm EFL lenses at 1.25x zoom.

Table 12. Optical characteristics of design modeled in WinLens-3D.

Lens Configuration	Total Length of IR Section	Spherical Aberration	Coma	Distortion
Single 25 mm EFL	118.8 mm	2.4	-1.3	0.095
Double 25 mm EFL	94.6 mm	4.9	-2.8	0.52
Single 50 mm EFL	229.2 mm	0.92	-0.34	0.007
Single 50 mm EFL 1.25x zoom	248.4 mm	0.73	-0.31	0.0087
Double 50 mm EFL	183.7 mm	1.9	-0.59	-0.18
Double 50 mm EFL 1.25x zoom	205.0 mm	1.3	-0.53	-0.059

The single 50 mm EFL lens and double 50 mm EFL lens designs in the forward concavity orientation resulted in the lowest aberration, coma, and distortion characteristics. The designs incorporating the 25 mm EFL lens produced the worst results. The experimental results of each design shown are analyzed in Chapter IV.

E. CUBESAT PAYLOAD REQUIREMENTS

The TIC was required to be compatible with integration into a CubeSat. Therefore, size, weight, and power constraints of the selected CubeSat determined its design requirements. CubeSat bus design standards were established by the California Polytechnic State University of San Luis Obispo (Cal Poly) and Stanford University in 2004 in order to facilitate access to CubeSats by university students and other researchers for a fraction of the cost-of-launch compared to traditional launch providers [62]. CubeSat bus design standards have been continually updated since 2004 and are currently recognized and supported by hundreds of organizations, including NASA. Most critically, they are recognized by launch providers in order to provide standardization for launch dispenser integration. The standardized dimensions and axis conventions of a 6U CubeSat are shown in Figure 28.

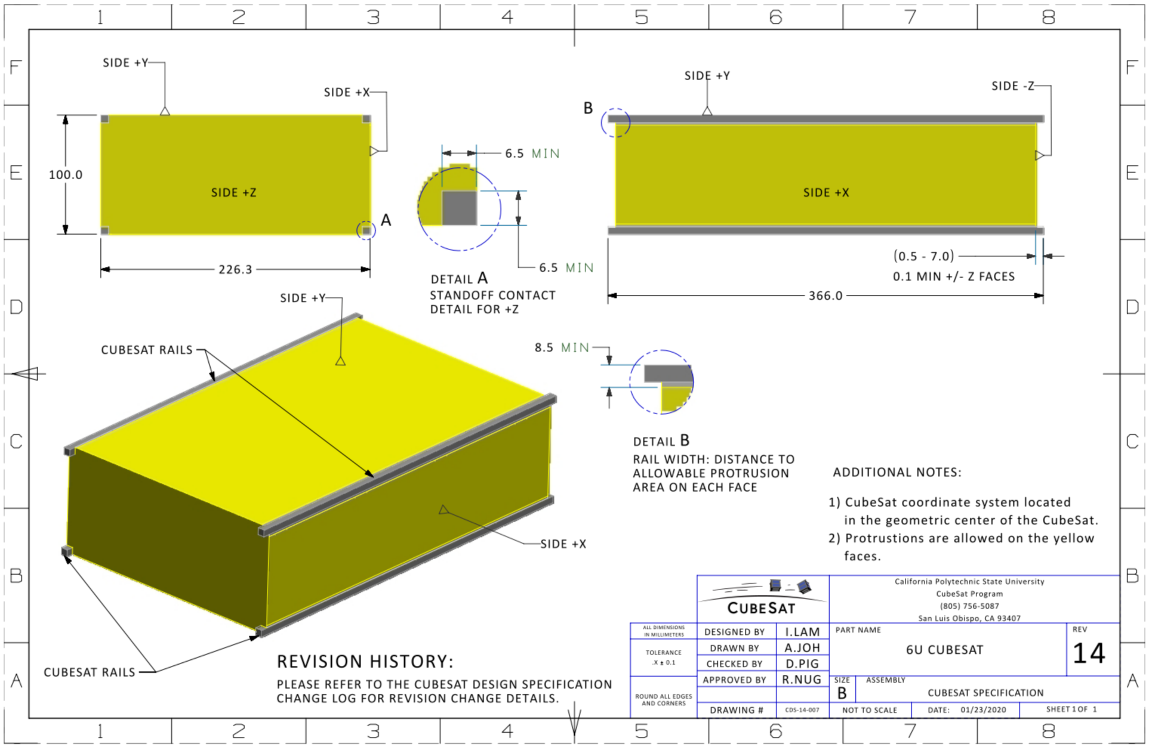

Figure 28. Dimensions and axes designation conventions of a standard 6U CubeSat bus. Source: [54].

For the purposes of this research, an Astro Digital Corvus 6U CubeSat was chosen as the hypothetic vehicle for the TIC. The Corvus 6U bus was selected by the Space Systems Academic Group Small Satellite Laboratory to host the previous version of the TIC and, therefore, it was reasonable to design this iteration to meet the same constraints. The Corvus 6U bus design follows the requirements of the CubeSat Design Specifications document [54]. A standard Corvus 6U CubeSat is shown in Figure 29.

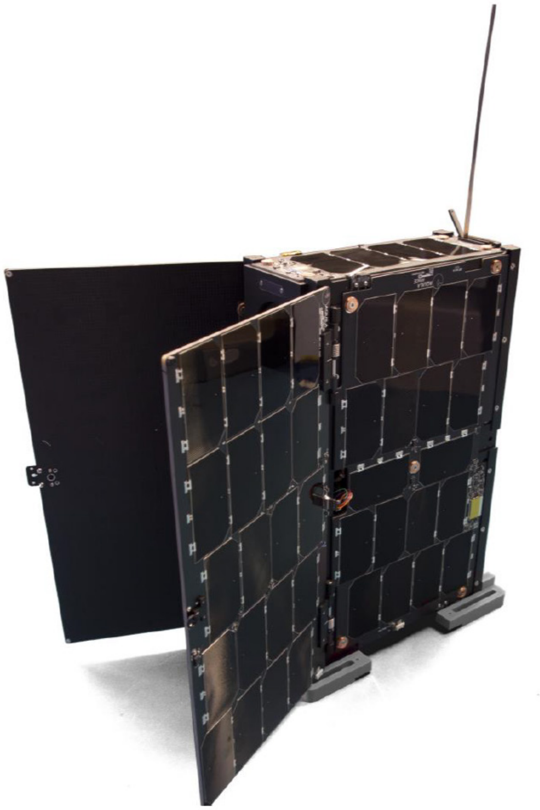

Figure 29. Integrated Corvus-BC spacecraft based on Corvus-6 6U bus. Source: [63].

1. Size

CubeSats are defined by the amount of internal volume available in the spacecraft structure, called units or "U." A 1U CubeSat is broadly defined with approximate external dimensions of 100 × 100 × 113.5 mm. The external dimensions of the deployment rails of a standard 6U CubeSat are required to be within 100 × 226.3 × 366 mm, equivalent to approximately six 1U CubeSats arranged in a rectangle [54]. The payload compartment accounts for half of the bus's total volume, as shown in Figure 30.

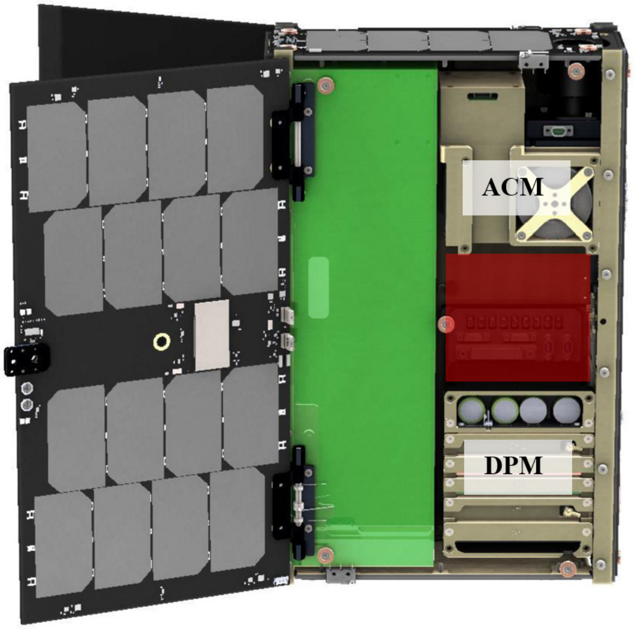

Normal available payload volume is highlighted in green. Additional payload volume, if available, is highlighted in red. This bus was used with the previous version of the TIC.

Figure 30. Astro Digital Corvus-6 6U CubeSat bus. Adapted from [63].

There is a small amount of additional payload volume available between the Attitude Control Module (ACM) and Data and Power Module (DPM) in the remaining 3U volume occupied by the spacecraft subsystems. If unused, this additional volume can be utilized for a small secondary payload or payload subsystem. The dimensions of the total interior and payload space of the Corvus 6U bus were measured using a computer-aided design (CAD) model and these measurements are shown in Table 13.

Table 13. Corvus 6U bus measurements.

Dimension/ Axis	**X (mm)**	**Y (mm)**	**Z (mm)**
Exterior	226.3	100.0	365.9
Interior	213.4	89.2	349.2
Payload	109.4	89.2	349.2

The payload compartment dimensions constrained the TIC to a length of 349.2 mm, a width of 89.2 mm, and a height of 109.4 mm. There are provisions which allow components of the TIC to extend outside of the spacecraft bus on the z-axis by up to 25.4 mm (1-inch), so in no cases shall the TIC's overall length exceed 374.6 mm [54], [64]. Allowances for exceeding the base dimensions of the CubeSat are dispenser dependent; therefore, primary effort was placed in complying with the dimensions listed in Table 13.

2. Weight

Maximum spacecraft mass is limited by specific CubeSat configuration and is shown in Table 14 [54]. These masses are the total allowable mass of the spacecraft. To calculate the maximum allowable payload mass, the bus mass must be subtracted from the total allowable mass. The mass of the Corvus 6U bus is 7.5 kg [63]. This results in a maximum payload mass of 5.5 kg and was considered a design constraint for the TIC.

Table 14. Maximum mass per CubeSat Configuration. Source: [54].

U Configuration	Mass [kg]
1U	2.00
1.5U	3.00
2U	4.00
3U	6.00
6U	12.00
12U	24.00

Each optical configuration mass was measured using a lab scale. This iteration of the TIC will utilize similar, if not identical, supporting electronics as the Mola TIC for conversion of output video format from the Tamarisk® 640 camera to a satellite communications compatible format. At the time of writing the final mounts for mating the TIC to the spacecraft have not been completed and their masses are unknown. However, a 50% mass margin was added to account for the mounting hardware in each configuration.

The masses of each optical system configuration remain below the design constraint of 5.5 kg and are shown in Table 15.

Table 15. Terahertz Imaging Camera Mass.

Component	Lens Design Mass (g)	Mirror Design Mass (g)
Optical Payload	650	860
Mounting (50% Payload Mass)	325	430
Raspberry Pi Stack [a]	90	90
Total Mass	1,065	1,380
Mass Budget Margin	+ 4,435	+ 4,120

Source: [a] [48].

3. Power

The peak payload power and maximum continuous payload power generated by a spacecraft are specific to each bus based on its electrical power subsystem and power generation capabilities. On CubeSats, power generation is accomplished by photovoltaic cells (solar panels) and power is stored with lithium-ion batteries. The Corvus 6U bus's electrical power subsystem is capable of generating 35 W peak power in sun-tracking mode and 10 W maximum continuous payload power at a 100% duty cycle [63]. It is desired for the TIC to collect imagery to the max extent possible throughout its lifetime and, therefore, its power consumption must remain below the maximum continuous payload power of 10 W, accounting for other subsystem power draws. The power requirements of the Tamarisk® 640 camera was measured by [65] and are listed in Table 16. The telemetry, tracking, and command (TT&C) subsystem consumes 0.2 W in receive mode and 10 W in transmit mode. Therefore, the TIC will likely not be able to collect imagery while the TT&C is transmitting. However, a more thorough analysis of the power budget should be conducted once a detailed concept of operations is developed and can be simulated and tested on flight-like hardware.

Table 16. Power Budget

Component	**TT&C Idle Power (W)**	**TT&C Receive Power (W)**	**TT&C Transmit Power (W)**
TT&C Uplink[a]	0	0.2	0
TT&C Downlink[a]	0	0	10
Tamarisk® 640[b]	1.2	1.2	1.2
Computing Stack[c]	2.6	2.6	2.6
Total Max Power Draw	3.8	4.0	13.8
Max Continuous Power	10	10	10
Power Margin	+ 6.2	+ 6.0	- 3.8
Percent Margin	163%	150%	- 38%

Sources: [a] [63], [b] [59], [c] [65].

THIS PAGE INTENTIONALLY LEFT BLANK

IV. EXPERIMENTAL SETUP AND RESULTS

Experimentation and characterization of the Terahertz Imaging Camera's optics were conducted in two phases. The first phase was the characterization and evaluation of the IR section involving the IR emitting backside of the THz-to-IR FPA, refractive optics, and Tamarisk® 640 LWIR camera. The second phase was the characterization and evaluation of the THz section involving a 4.7 THz quantum cascade laser, THz optics, and the THz-to-IR FPA. The final design selection of each section was determined independently with consideration of their respective sizes and their contribution to the total design dimensions. This is because the aggregate size is required to stay within the dimensional constraints of the CubeSat payload compartment, as presented in Chapter III. This chapter describes the design and characterization of each section and concludes with an analysis of the total system design.

A. INFRARED SECTION EXPERIMENTATION AND RESULTS

The modeled IR optical designs presented in Chapter III were built and tested on an optical bench, with the exception of the double 25 mm EFL Ge lens design. Experimental analysis of this design was not conducted, as the optimal spacing between the last lens element and the Tamarisk® 640 FPA was too short (~5 mm). Setup at this spacing was not possible because the distance between the Tamarisk® 640 FPA and the front of the custom housing is greater than 5 mm, preventing mounting of the lens at the required distance to the FPA. A double 25 mm design is used in the Mola TIC at lens spacing less than ideal for optimal focalization as calculated by Winlens-3D. This was a necessity given the size restrictions of the Mola TIC [48]. A further comparison of the Mola TIC and the final configuration presented in this chapter is given in Chapter V. The six remaining refractive and reflective designs were experimentally tested. These configurations, along with their apertures and effective focal lengths, are shown in Table 17.

Table 17. Refractive/Reflective optics tested in lab experimentation.

Configuration	Aperture (inches)	EFL (mm)
Single Lens	2	50
Single Lens (1.25x zoom)	2	50
Double Lens	2	50
Double Lens (1.25x zoom)	2	50
Single Lens	2	25
Single Mirror	3	50.8

1. Experimental Setup

Each of the configurations in Table 17 was built on an optical bench. The output video and images produced by the Tamarisk® 640 of the back of the THz-to-IR FPA were compared. A previously damaged and unusable THz-to-IR FPA was used to fine tune the focalization. The defects were mostly concentrated in the central area of the FPA and had no effect on the characterization of the IR optics. The FPA mount was fixed at one end of the optical bench, while the lens(es) and Tamarisk® 640 camera were installed at the same elevation but placed in moveable posts. This allowed independent adjustment of each component along the optical axis to find their ideal placement with respect to the THz-to-IR FPA. The ideal placement was the placement along the optical axis that yielded the correct demagnification factor (THz-to-IR FPA fills the full output video frame) and exhibited minimal visually detectable aberration and distortion. Figure 31 shows a representative optical bench setup of a double lens configuration. Experimentation showed that the ideal placement of lenses along the optical axis differed from Winlens-3D modeling results, particularly in the double-lens designs. In the most extreme case, the placement of the first lens in the double-lens configuration was 5.7 mm further from the THz-to-IR FPA than Winlens-3D predicted.

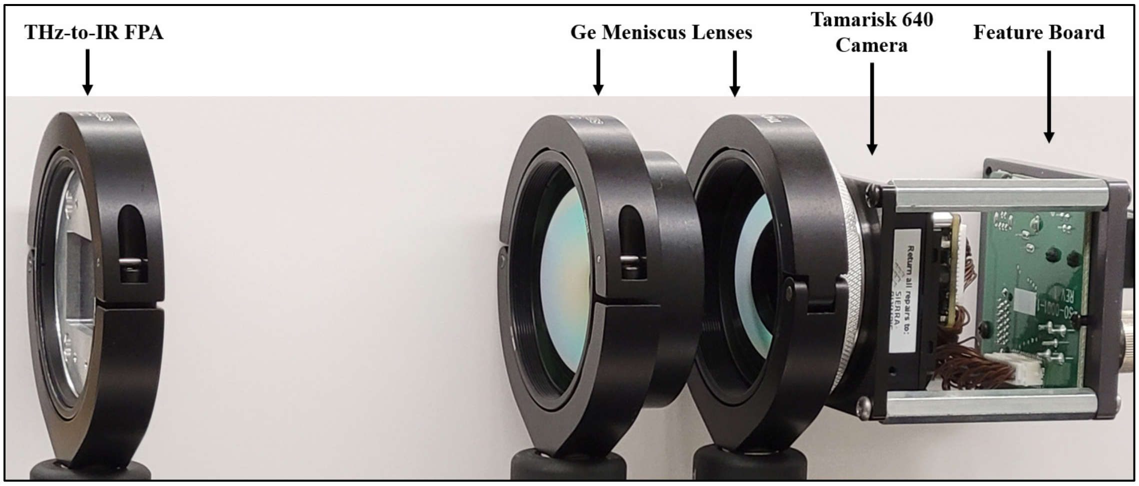

This image shows an example experimental setup for the IR section mounted on an optical bench. This setup is a double 50 mm EFL lens design. The THz-to-IR FPA, Ge meniscus lenses, Tamarisk® 640 LWIR camera, and Tamarisk® Feature Board are shown aligned with the optical axis.

Figure 31. Representative IR section experimental setup

2. Results

Characterization and evaluation of the IR section were conducted using the analog video output of the Tamarisk® 640 camera via the Feature Board. The Tamarisk® 640 Feature Board is a proprietary circuit board designed to input data from the Tamarisk® 640 camera and simultaneously output analog (via an RS-232 port) and digital video (via a Camera Link port). The feature board has a dedicated power plug and mini-USB port for power input and camera settings control through a proprietary computer program called DRS Camera Control Software. The RS-232 output video was displayed on a monitor and recorded using an analog-to-digital video capture card. Each configuration's video and image results were evaluated for visual signs of distortion and aberration and compared to each other. The image results from the most ideal placement of optical components in each configuration are shown in Figure 32.

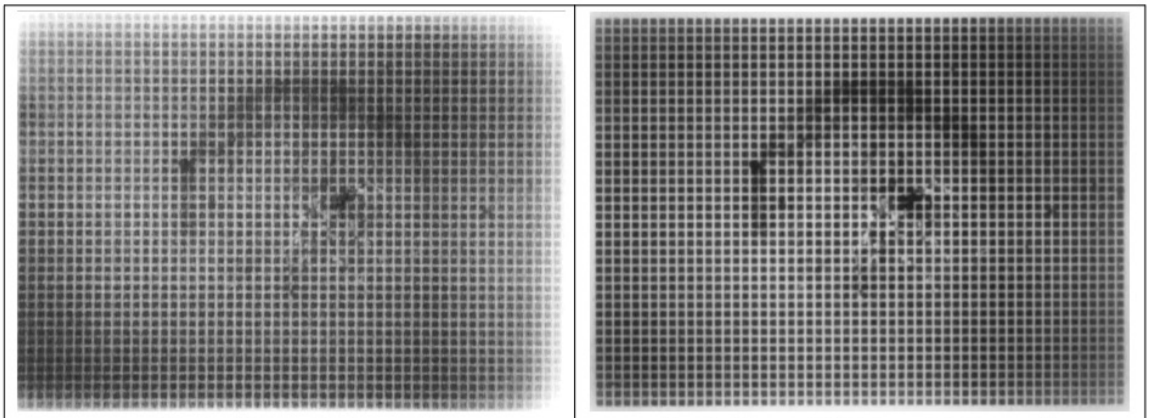

(a) **Single 50 mm EFL Lens**

(b) **Single 50 mm EFL Lens (1.25 zoom)**

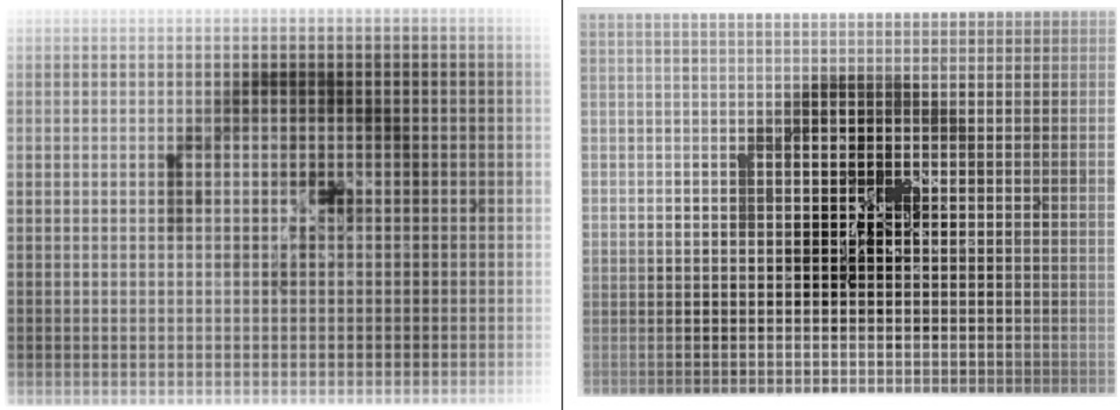

(c) **Double 50 mm EFL Lens**

(d) **Double 50 mm EFL Lens (1.25 zoom)**

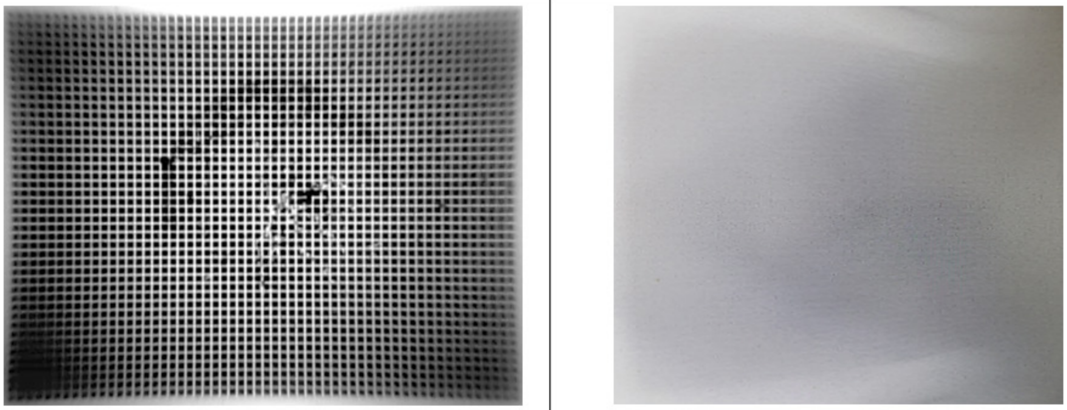

(e) **Single 25 mm EFL Lens**

(f) **Single 50.8 mm EFL Mirror**

These six panels show the IR section focalization of the THz-to-IR FPA for each configuration that was tested. Images were captured via analog video output from the Tamarisk® 640 camera and an analog-to-digital capture card.

Figure 32. IR section THz-to-IR FPA image results.

The images produced by the single 25 mm EFL lens and single 50.8 mm EFL mirror, shown in Figure 32 (e) and (f), were immediately ruled out due to the high levels of distortion and aberration evident in their images. The mirror design produced the worst results and the image of the THz-to-IR FPA is hardly recognizable due to substantial distortion and aberration. Additionally, the mirror design requires a 90° bend in the system, the dimensions of which were not compatible with the allowable payload volume. The single 25 mm EFL lens design also shows considerable aberration along the edges of the image, which manifests as blurring as the radial distance from the optical axis is increased. In addition, pincushion distortion is evident. These experimental results agree with the Winlens-3D modeling results presented in Chapter III.

The images produced by the single and double 50 mm EFL lens configurations, shown in Figure 32 (a) and (c), show mutually comparable results. Distortion is not recognizable in the images, as predicted by Winlens-3D modeling. However, both images show aberration artifacts in the four corners of the images, evidenced by washout and blurring in those areas. The single and double 50 mm EFL lens designs with a built-in 1.25x digital zoom (performed by the Tamarisk® 640 camera), shown in Figure 32 (b) and (d), yielded the most promising results. In both images, distortion and aberration are minimized and are not visually present. This increase in optical performance over the non-zoomed designs was due to the outer areas of the object plane being excluded from the image by the zoom factor. Visual aberration was present in the outer edges of these images (outside the boundaries of the FPA's pixels) when the Tamarisk® 640 zoom setting was set to 1x but was selectively omitted from the image by the zoom function.

3. Design Selection

The double 50 mm EFL design with 1.25x digital zoom was selected as the final IR configuration due to its shortened length compared to the single 50 mm EFL design with 1.25x zoom. The single lens 1.25x zoom design resulted in a length that did not allow sufficient space for the remainder of the TIC design, leaving only 80.6 mm for the THz section. The length of each IR configuration spanning the distance between the THz-to-IR FPA and Tamarisk® 640 FPA is shown in Table 18. The total IR section length is given by adding the distance between the LWIR FPA and back of the Tamarisk® 640 16-pin cable connector (17 mm) and is shown in the third column of Table 18.

Table 18. IR section configuration lengths.

Configuration	THz-to-IR FPA to LWIR FPA (mm)	Total IR Section Length (mm)
Single 50 mm EFL Lens	232.1	249.1
Single 50 mm EFL Lens (1.25x zoom)	251.6	268.6
Double 50 mm EFL Lens	193.5	210.5
Double 50 mm EFL Lens (1.25x zoom)	219	236
Single 25 mm EFL Lens	119.1	136.1
Single 50.8 EFL Mirror	183.6	200.6

B. TERAHERTZ SECTION EXPERIMENTATION AND RESULTS

Four optical configurations were built and tested with the aim of selecting the best performing as the final THz section design. A configuration utilizing a 3-inch gold-coated mirror was tested as the baseline configuration for analyzing and comparing the four designs considered for spaceflight. The protected gold-coated mirrors reflect and focus 99% of incident THz radiation and, therefore, are well-qualified to act as a baseline with which to compare other designs that exhibit higher attenuation throughout the optical path. Baseline incident power-per-pixel results were utilized for normalization of the thermal response (ΔT) for each configuration, as detailed in proceeding sections. The baseline configuration did not include an IR filtering element and therefore, was not considered for flight aboard a spacecraft. The four designs considered for spaceflight included two reflective and two refractive designs.

The gold-coated parabolic mirror is highly reflective in a wide range of wavelengths, including IR. Therefore, an IR filter was necessary in the mirror configurations to prevent infrared radiation reaching the THz-to-IR FPA. To prevent this, the first mirror design incorporated a copper multi-mesh filter introduced in the optical path prior to the FPA. The second mirror design utilized a 4 mm Tsurupica™ window for the same purpose. Each filter is described in Chapter III. The remaining configurations were refractive optics designs and utilized a 2-inch HDPE lens and a 3-inch Tsurupica^{TM} lens, respectively. Multi-lens designs were not considered in this section's development due to the compounding attenuation caused by multiple stacked elements.

A THz source with an output frequency matching the one of the design frequencies of the THz-to-IR FPA was required for experimentation and characterization due to the FPA's narrowband sensitivity. A 4.7 THz EasyQCL-1000 Turnkey Terahertz Source, manufactured by LongWave Photonics LLC, was used as the source. The QCL has a range of user adjustable settings that include bias voltage, pulse width, pulse repetition frequency, and gating. The bias voltage was set at either 17.5 or 18.5 V, depending on the experimental setup. A 2000 ns pulse width was used throughout. Average power output was adjusted by varying the pulse repetition frequency, which modulates the laser. The pulse repetition frequency was varied between 3 and 125 kHz throughout experimentation and tailored for each measurement, depending on the configuration. Gating at various periods was accomplished with a waveform generator. The QCL also requires vacuum and cryogenic cooling during operation. Vacuum was maintained at ~1.0×10-7 Torr with internal temperatures between 21.4 and 22.5 K during operation of the QCL.

1. QCL Frequency/Power Correlation

The THZ 20 pyroelectric detector is manufactured by Sensor- und Lasertechnik, and converts incident radiation in the 0.6 – 6 THz range to an output voltage signal [66]. This output signal is given in root square mean (RMS) voltage and is converted to power using Equation 11 [66].

$$P = V_{RMS}\left(\frac{2\sqrt{2}}{58.8\ {}^{V}\!/\!_{W}}\right) \tag{11}$$

where P is incident power, V_{RMS} is THZ 20 measured voltage, and 58.8 V/W is the detector's sensitivity [66].

Pulse repetition frequency was converted to power by taking voltage measurements for various modulation frequencies between 3 – 125 kHz at bias voltages of 17.5 and 18.5 V.

A gating frequency of 21 Hz was used, as recommended by the THZ 20 manufacturer [66]. Measurements at both biases were analyzed to develop a method for correlating subsequent measurements taken at either voltage. Measurements were taken with the pyroelectric detector abutting the QCL's polyethylene window. This setup is shown in Figure 33.

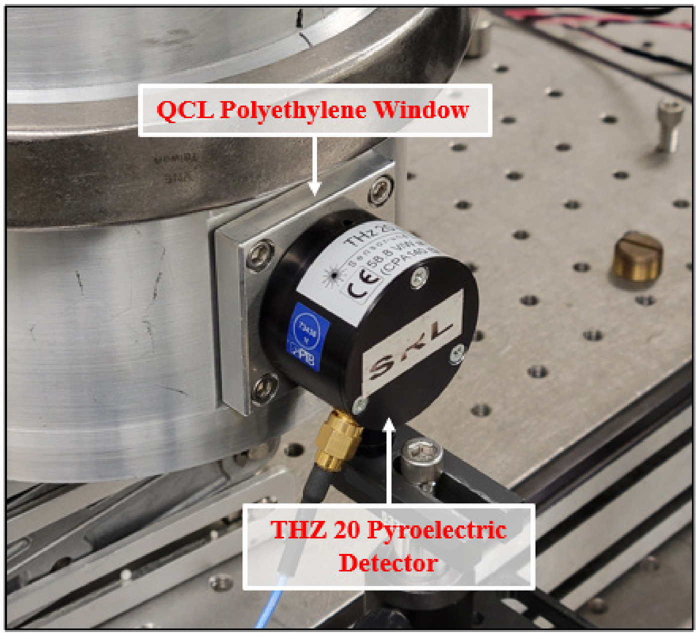

This setup shows the QCL polyethylene window (blocked) and the THZ 20 pyroelectric detector adjoining the window for measurement. VRMS measurements were used to correlate incident power between different QCL bias voltages.

Figure 33. QCL power measurement setup.

Noise floor measurements were recorded at incremental pulse repetition frequencies with a metallic plate covering the THZ 20's aperture to block radiation emitted by the QCL. The same incremental measurements were then taken with the metallic cover removed, exposing the detector's aperture to the incident THz radiation. The difference between the unblocked and noise measurements were considered the true response to the emitted radiation. The slope of a linear fit of each dataset yielded the correlation between incident power on the detector window and pulse repetition frequency. The fitted slopes of the 17.5 V and 18.5 V supply voltages were 144.6 and 177.6 µW/kHz, respectively. The ratio, $\varepsilon = 0.8138$, between the 17.5 V and 18.5 V fitted line slope was used to convert measurements taken at one voltage to another.

2. Collimation

As the emitted beam of the QCL is divergent, a convergent lens was required to collimate the energy output from the laser, assumed to be a point source emitter. A 1.5-inch 38.1 mm EFL silicon (Si) lens was used for collimation. Pyroelectric detector voltage measurements of the collimated THz beam were taken from various distances spanning 0.3 – 1.8 m from the lens to fine tune the collimation. Additionally, measurements were taken outside the borescope of the collimating lens at varying distances to ensure that beam divergence stayed within acceptable limits to approximate a far distant THz source.

3. Discussion of Experimental Setup

Two sets of measurements were required to evaluate the performance of each optical configuration. W. Melos-Guimaraes [15] conducted the first set of measurements with the baseline mirror configuration to determine incident power as a function of QCL pulse repetition frequency on an area the size of a single THz-to-IR FPA pixel. This corresponds to the sensing element area (~200×200 μm). The second set of measurements were conducted as part of this research using a Teledyne FLIR A6703sc thermal imaging camera to measure the thermal response of a single FPA pixel to various pulse repetition frequencies. These measurements were performed for the baseline configuration and configurations considered for spaceflight. These measurements were repeated for several pixels in the array, showing very good and consistent repeatability. The baseline power measurements and thermal response measurements were then combined to relate the ΔT of the THz-to-IR FPA to the single pixel incident power for each optical configuration, revealing the performance of each optical design.

4. Mirror Configuration FPA Sensitivity

RMS voltage was measured for various QCL modulation frequencies at the focal point of the mirror using an iris and the THZ 20 detector [15]. The mirror was fixed to an adjustable rotational platform within the collimated beam to focus the incident THz radiation. The THZ

20 detector was fixed on a three-axis adjustable platform at the mirror's focal point. The iris aperture diameter was set to 1 mm and placed on the same platform at a distance in front of the detector to effectively illuminate an area equivalent to that of a submatrix of 3×3 pixels of the THz-to-IR FPA. A reference QCL beam was generated while rotational adjustments of the mirror and lateral, vertical, and depth adjustments of the iris/THZ 20 platform were made to maximize the THZ 20 voltage measurement. This allowed for fine tuning of both the mirror focalization and positioning of the iris at the focal point. Voltage measurements for incremental QCL pulse repetition frequencies were then recorded [15]. The setup for these measurements is shown in Figure 34.

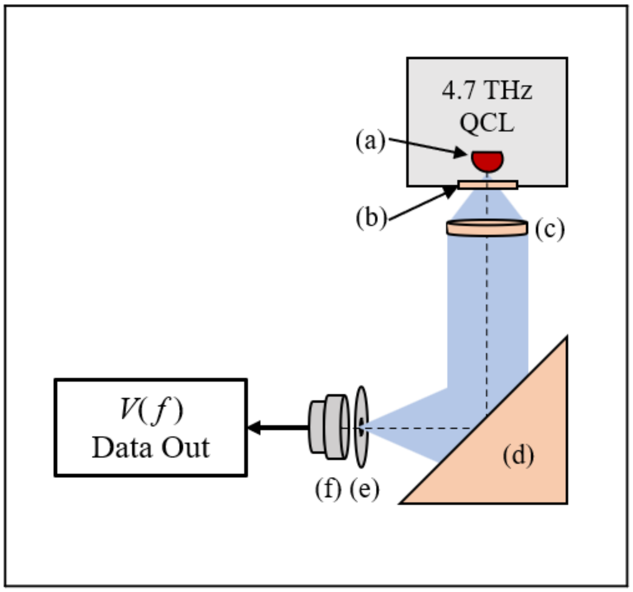

This block diagram shows the setup for measuring incident power on a 3×3 pixel submatrix of the THz-to-IR FPA. THz radiation is emitted (a), passing through a polyethylene window (b). The divergent beam is then collimated by a Si lens (c). The resultant collimated beam is reflected by the mirror (d), passing through a ~1 mm diameter iris (e), and is focused on the THZ 20 detector window (f). V_{RMS} data is passed by the THZ 20 and recorded as a function of QCL pulse repetition frequency. The blue shaded region shows the THz beam and the dotted line represents the optical axis.

Figure 34. THZ 20 power measurements setup.

The QCL settings for these measurements were 18.5 V, 2000 ns pulse width, pulse repetition frequencies between 3 and 30 kHz, and 21 Hz gating [15]. Two sets of measurements were performed for each QCL modulation frequency. The first set of measurements established the noise floor for each pulse repetition frequency, as previously discussed. The same procedure was repeated with the metallic cover removed to measure the incident power generated by the QCL. The resultant voltage difference was converted to power using Equation 11. The result was the calculated incident power on an area approximately the size of a 3×3 pixel submatrix.

A scaling factor was required to obtain incident power on a single pixel's sensing element, which has approximately one-ninth the area utilized for the power measurements. To obtain these results, ΔT was measured at various points within the 3×3 submatrix using the FLIR camera. Melos-Guimaraes [15] found that the thermal response across the illuminated area exhibits a Gaussian pattern. This indicates the focused THz energy, and thus the incident power, is more concentrated at the center of the focused beam and diminishes radially outward. Therefore, the data were fitted to a three-dimensional Gaussian function to evaluate the distribution of incident power. The portion of the measured power that is incident on a single sensing element (200×200 μm), at the center, was estimated to be around 17%. This ratio was then used to estimate the incident power on a single sensing element as a function of QCL pulse repetition frequency. The conversion factor, ε, yielded results for an QLC biased at 17.5 V. These results are shown in Figure 35.

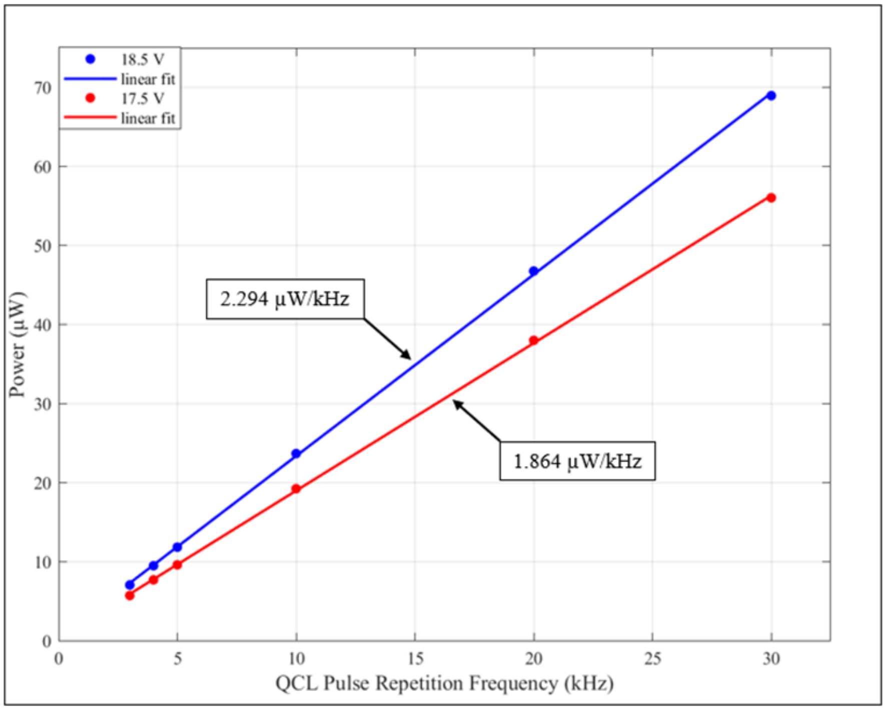

Measurement data are shown in solid circles. The solid lines are linear fits. The blue line corresponds to measurements at 18.5 V bias that yields a 2.294 µW/kHz slope. The red line corresponds to 17.5 V bias measurements and yields a 1.864 µW/kHz slope.

Figure 35. Incident power per pulse repetition frequency of a 200×200 µm pixel.

With this result, QCL pulse repetition frequencies can be converted to incident power in a single sensing element by multiplying the frequency (kHz) by Φ_p = 2.29 µW/kHz for an 18.5 V bias, and Φ_t = 1.86 µW/kHz for a 17.5 V bias.

5. THz-to-IR FPA Thermal Response

Measurement of the THz-to-IR FPA's thermal response to narrowband 4.7 THz radiation was achieved through the use of the QCL, collimation lens, FPA, FPA vacuum chamber, FLIR camera, and each of the five optical configurations. The QCL was set to 17.5 V bias voltage, 2000 ns pulse width, 300 mHz gating, and pulse repetition frequencies between 5 and 125 kHz. The collimation setup remained the same from the previous experiments. The FPA used in the experimental setup was the 2.06 and 4.75 THz interspersed circular resonator design developed by Guimarães [15]. The absorptance profile of this FPA and a diagram of a single pixel are shown in Figure 36.

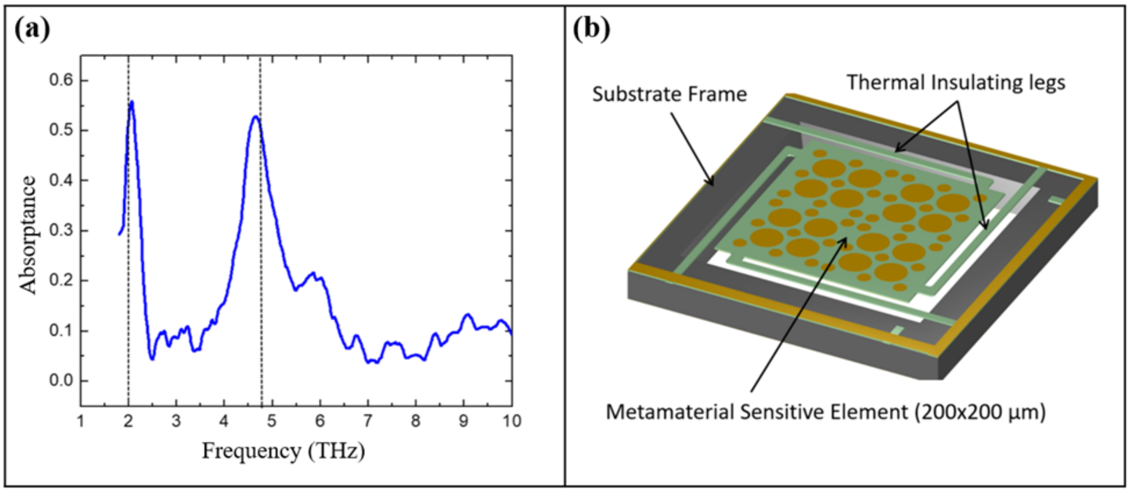

The absorptance of the dual-resonator FPA is shown (a) as a function of frequency. Greater than 0.50 absorptance is achieved at the absorption peak frequencies of 2.06 and 4.75 THz. (b) shows a diagram of a single pixel within the FPA. Both 2.06 THz and 4.75 THz resonators are shown with differing diameters.

Figure 36. Dual-resonator THz-to-IR FPA absorptance and pixel diagram. Adapted from [15].

The FPA was placed within a small vacuum chamber and depressurized to approximately 9.6 µTorr, mitigating heat loss due to convection. This enabled the THz-to-IR FPA to emit its THz-converted thermal energy primarily through radiation detectable by the FLIR camera. The THz-to-IR FPA was fixed to a three-axis adjustable platform for fine adjustments. The FLIR camera was placed on a mount and fixed at a distance which allowed focalization of the backside of the of the FPA. The temperature of the center pixel of the illuminated area was measured. These setups are shown in Figure 37.

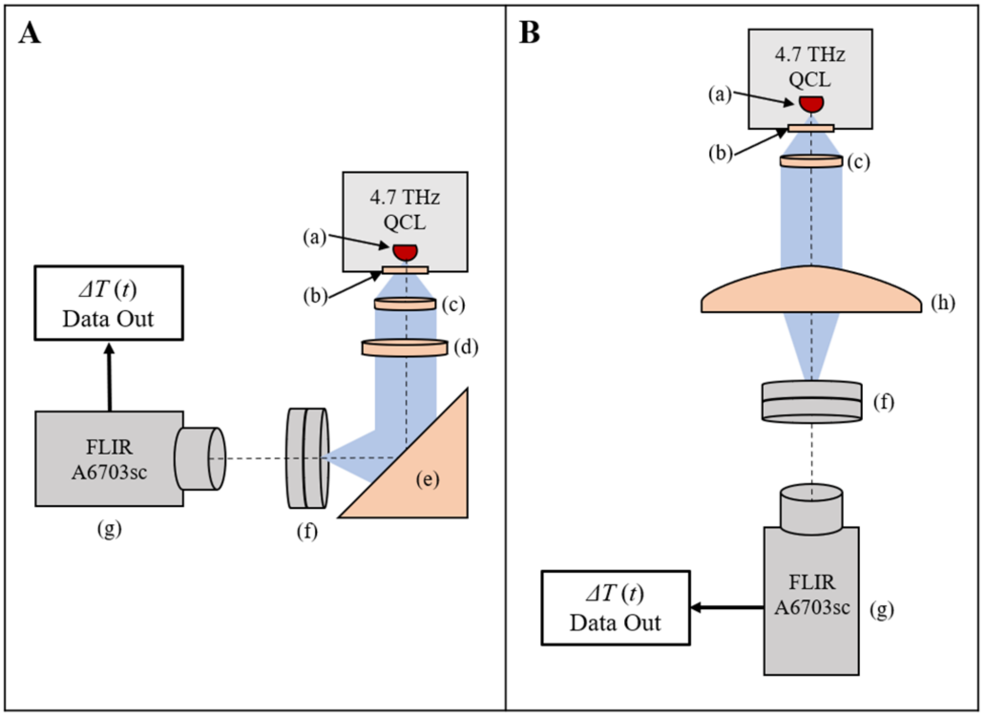

(A) Reflective design: THz radiation is emitted (a), passing through a polyethylene window (b). The divergent beam is then collimated by a Si lens (c) before passing through an optional metal mesh filter or 4 mm Tsurupica^{TM} window (d) (the filtering element was not used for the baseline configuration). The collimated beam is then focused by a gold-coated mirror (e) onto the THz-to-IR FPA. The FPA is shown here within a vacuum chamber (f) sandwiched by a Tsurupica^{TM} window on the incoming THz side and a ZeSe window on the outgoing IR side. The IR is focused by a FLIR A6703sc camera that outputs measured temperature as a function of time. The blue shaded region represents the THz beam and the dotted line represents the optical axis.

(B) Refractive design: The lens setup is much the same, except the filtering element is removed and a lens (h) replaces the mirror. This setup allows for a straight-line optical axis, identified by the dotted line.

Figure 37. Experimental setup for reflective and refractive designs.

The FLIR camera was first used to find the distance between the focusing element and FPA that achieved maximum focalization. This was achieved by minimizing the size of the focused beam footprint as it appeared on the FPA and then, more precisely, by finding the position that induced the maximum temperature response. Measurements of a single pixel's thermal response were then taken for each configuration at incremental pulse repetition frequencies. Data output was given in ΔT (K) as a function of time. Measurements of ~30 s were accomplished for each configuration and pulse repetition frequency, yielding ~10 irradiation cycles for each measurement. Four irradiation cycles were isolated, compiled, and plotted for each configuration, shown in Figure 38.

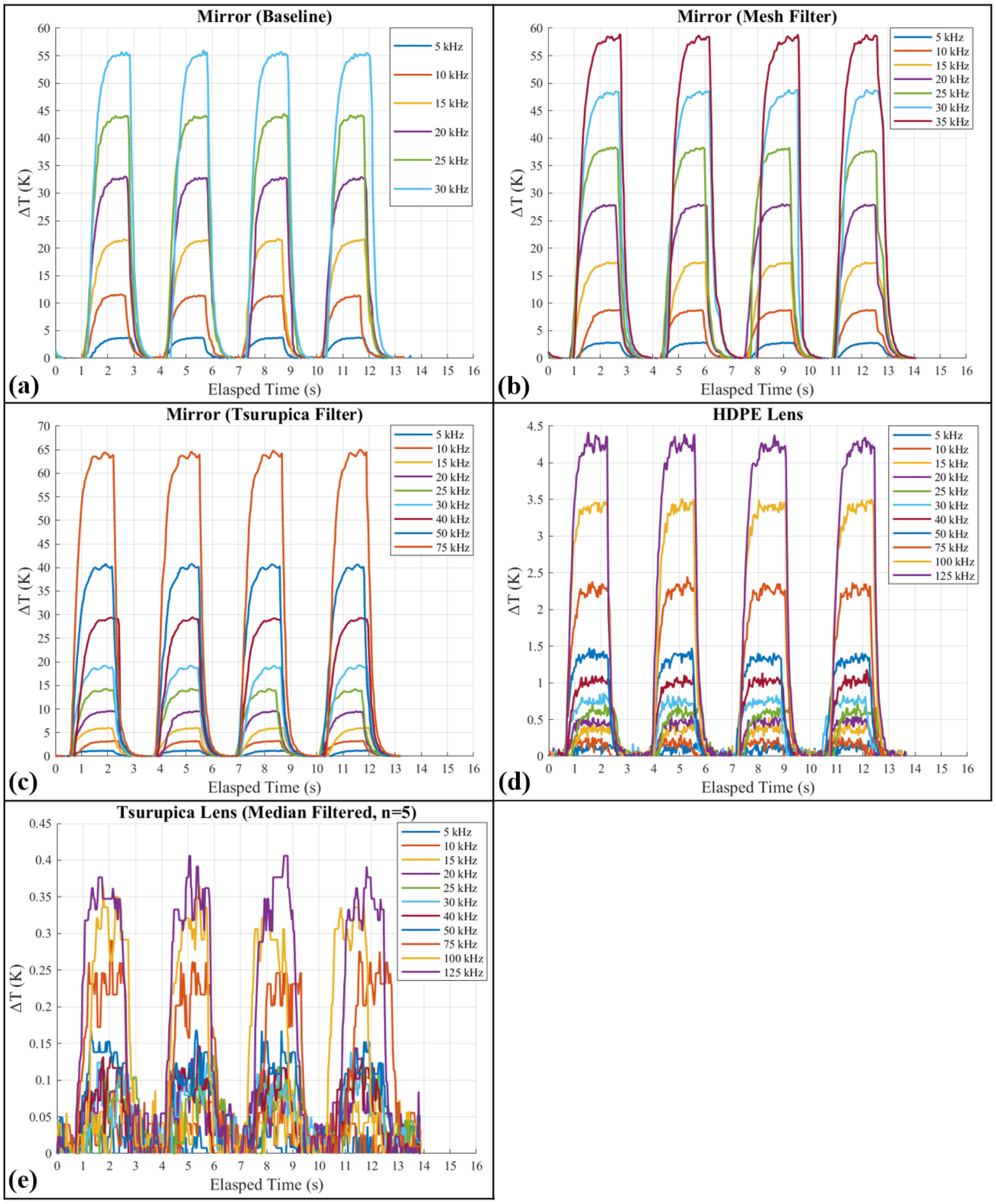
Mirror (Baseline)

Mirror (Mesh Filter)

Mirror (Tsurupica Filter)

HDPE Lens

Tsurupica Lens (Median Filtered, n=5)

(a) – (e) show the sensitivity of the THz-to-IR FPA for various optical configurations. Data is shown for four illumination cycles of the QCL with various pulse repetition frequencies. Temperature measurements were taken with a FLIR camera. The vertical scale varies substantially between each configuration.

Figure 38. Thermal response of various optical configurations.

Data in Figure 38(e) (Tsurupica^{TM} configuration) was smoothed for plotting and analysis purposes. Initial analysis of these results shows that the mirror design with a mesh filter performed best of the four configurations considered for spaceflight.

6. Results and Design Selection

The thermal response measurements and analyses were combined with the measurements and analyses conducted by Guimarães [15] to derive the sensitivity of the FPA (K/µW). These results were used for directly comparing each optical configuration. Conversion of the thermal response data, shown in Figure 38, from pulse repetition frequency to incident power was calculated by direct conversion using the conversion rate Φ_t (1.864 µW/kHz). The peak ΔT for each pulse repetition frequency in each configuration was averaged over their respective four irradiation cycles and plotted against the corresponding calculated incident power. These results are shown in Figure 39 for each optical configuration and consolidated in Figure 40 for comparison.

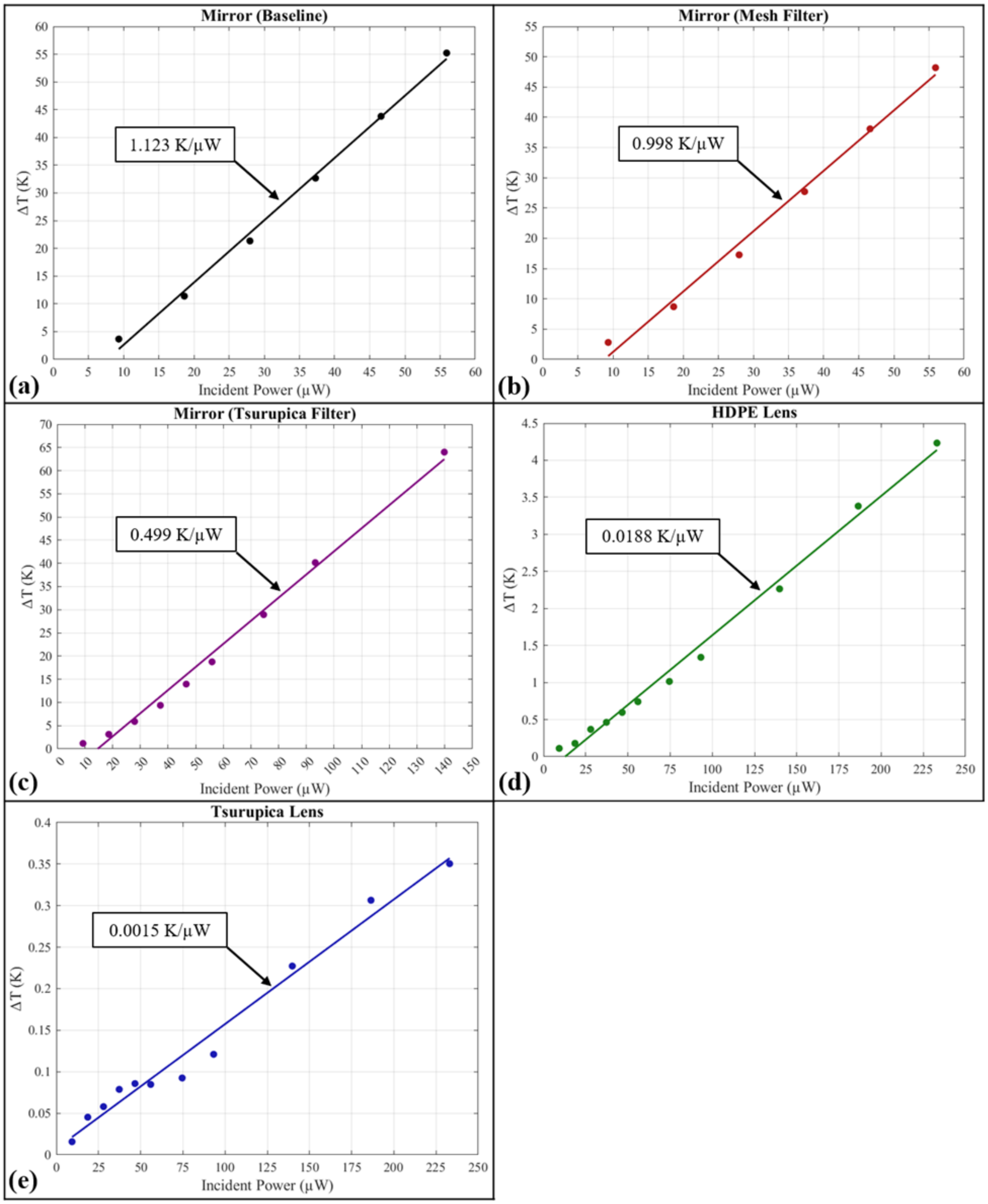

(a) – (e) show the sensitivity of the system per incident power for each optical configuration. As the same THz-to-IR FPA was used throughout, changes in sensitivity are the result of the effectiveness of the optics at transmitting/reflecting and focusing incident THz radiation. A linear fit was adapted for each plot using the data points shown (dots). The sensitivity shown (K/μW) is the slope of the linear fit.

Figure 39. Optical system sensitivity (K/μW) for various optical configurations.

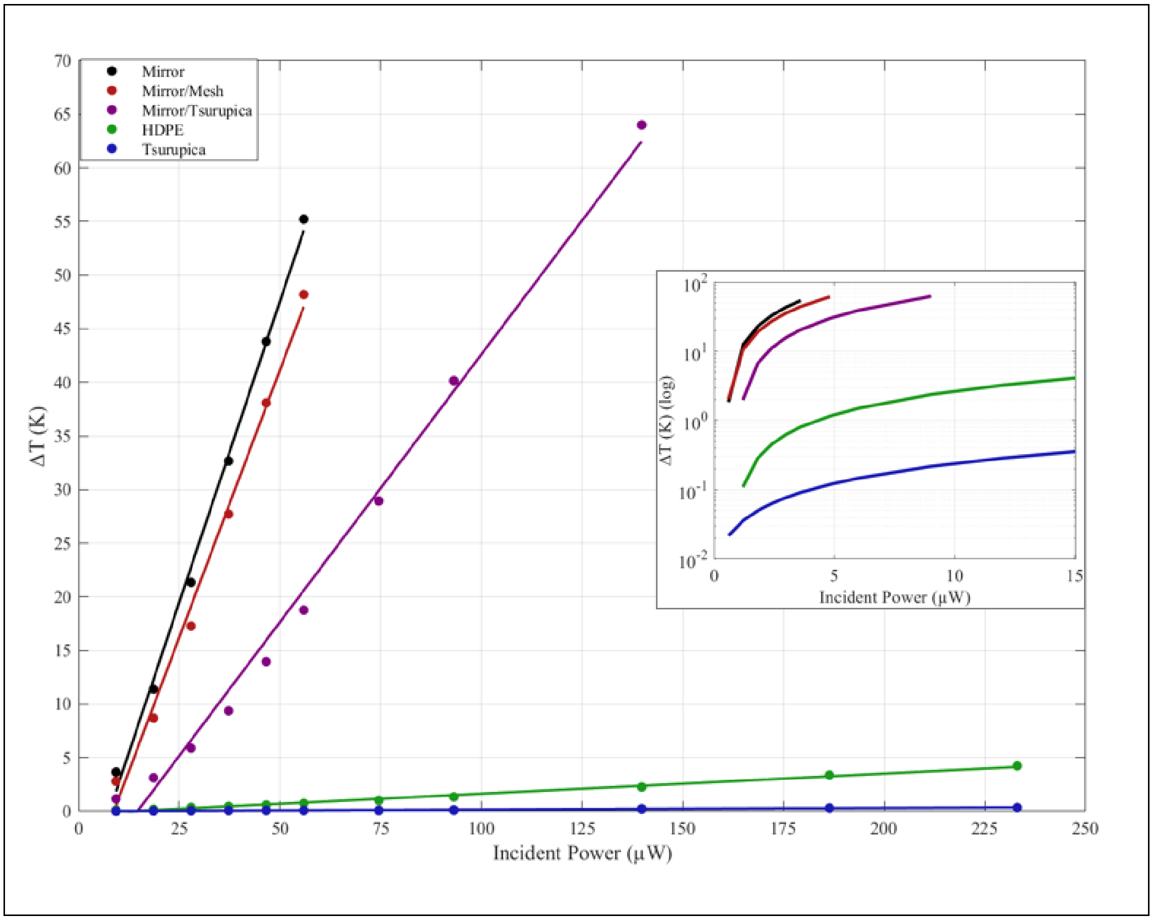

This figure shows the same data presented in Figure 39, but overlayed for direct comparison between the optical configurations. Additionally, a log scale inset is shown to better display Tsurupica^{TM} configuration with respect to the other configurations.

Figure 40. Consolidated optical system sensitivity (K/μW) with log scale inset.

The sensitivity of the FPA was found to be 1.23 K/ μW, given by Figure 39(a), and is comparable with the two FPAs fabricated and demonstrated by Alves et al. [12], 1.75 K/μW and 0.66 K/μW. The 1.75 K/μW FPA was designed with a carbonized aluminum backside, similar to the FPA used in this experimentation. However, it was a single resonator design with an absorption peak at about 95%, rather than the double resonator of the FPA used in this work with peak absorption of approximately 55% at the QCL frequency (see Figure 36).

Figure 40 clearly shows the influence of the optical elements on the sensitivity of the system. The attenuation caused by the refractive optics is very large when compared with the reflective optics, causing a reduction in sensitivity of approximately 2 orders of magnitude for the HDPE lens and 3 orders of magnitude for the Tsurupica^{TM} lens. A direct comparison of temperature fluctuations at 46.6 µW incident power were 55.2, 48.2, 18.8, 0.74, and 0.09 K for the mirror, mirror with mesh filter, mirror with Tsurupica^{TM} window, HDPE lens, and Tsurupica^{TM} lens, respectively. The reduction in performance due to the multi-mesh filter and Tsurupica^{TM} window agree well with their expected transmissions of 90% and 49% at 4.7 THz, respectively.

The poor performance of both lenses compared to the mirror is likely the result of high absorption due to lens thickness. For context, the thickness of the Tsurupica^{TM} lens at its apex is 30 mm. A transmissibility of 0.70 per 2 mm of material at 4.7 THz (see Figure 14) gives a 30 mm transmissibility of ~0.0047. As the gold-coated mirror exhibits a reflectivity of 0.99, applying the 0.0047 transmission to the ΔT of the mirror (55.21 K) at 46.6 µW gives a calculated ΔT of 0.262 K. This result is relatively comparable to the experimental result of 0.085 K. The losses in the HDPE lens can be evaluated similarly. A transmissibility of approximately 0.68 at 4.7 THz per 2 mm of material and a peak thickness of 18 mm gives a total transmissibility of 0.031. Applied to the same results for the mirror at 46.6 µW yields a calculated ΔT of 1.71 K. Again, the result is similar to the measured ΔT of 0.74 K.

Of the configurations considered for spaceflight, the highest sensitivity was achieved by the mirror configuration with a copper multi-mesh filter at 1 K/µW. This configuration was chosen as the final design for the THz section of the TIC. It yielded the best results for optical performance and met the requirements driven by the 6U CubeSat constraints of mass and volume presented in Chapter 3. The lengths of each THz section configuration are shown in Table 19.

Table 19. THz section configuration lengths.

Configuration	Length (mm)
3-inch Tsurupica^{TM} Lens	60
2-inch HDPE Lens	53
3-inch Gold-Coated Mirror	91.7

C. COMPLETED SYSTEM DESIGN

The final optical configuration selected for the TIC consists of a 3-inch 90° off-axis gold-coated parabolic mirror, a copper multi-mesh IR filter, THz-to-IR FPA, two 2-inch antireflective coated germanium aspheric meniscus lenses, and a Tamarisk® 640 longwave infrared uncooled microbolometer camera. The total length of the system is 319.2 mm, as measured from the termination of the primary mirror to the termination of the Tamarisk® 640 16-pin connector. The weight of the system is 860 g, not including the computing hardware and mounting system, both of which will be required for the flight-ready payload. As of writing, the mounting system is completing final fabrication and testing; however, a 3-D printed prototype of the mounting system was completed and is shown in Figure 41. The mounting system CAD model was designed by Gobrecht [67], and is also shown in Figure 41. Additionally, the optical components of the completed TIC are shown in Figure 41. The spacing between optical elements are included for reference by future researchers. The only measurement not shown in this figure is the elevation of the bottom of the optical tube above the base plate of the mirror, 4 mm.

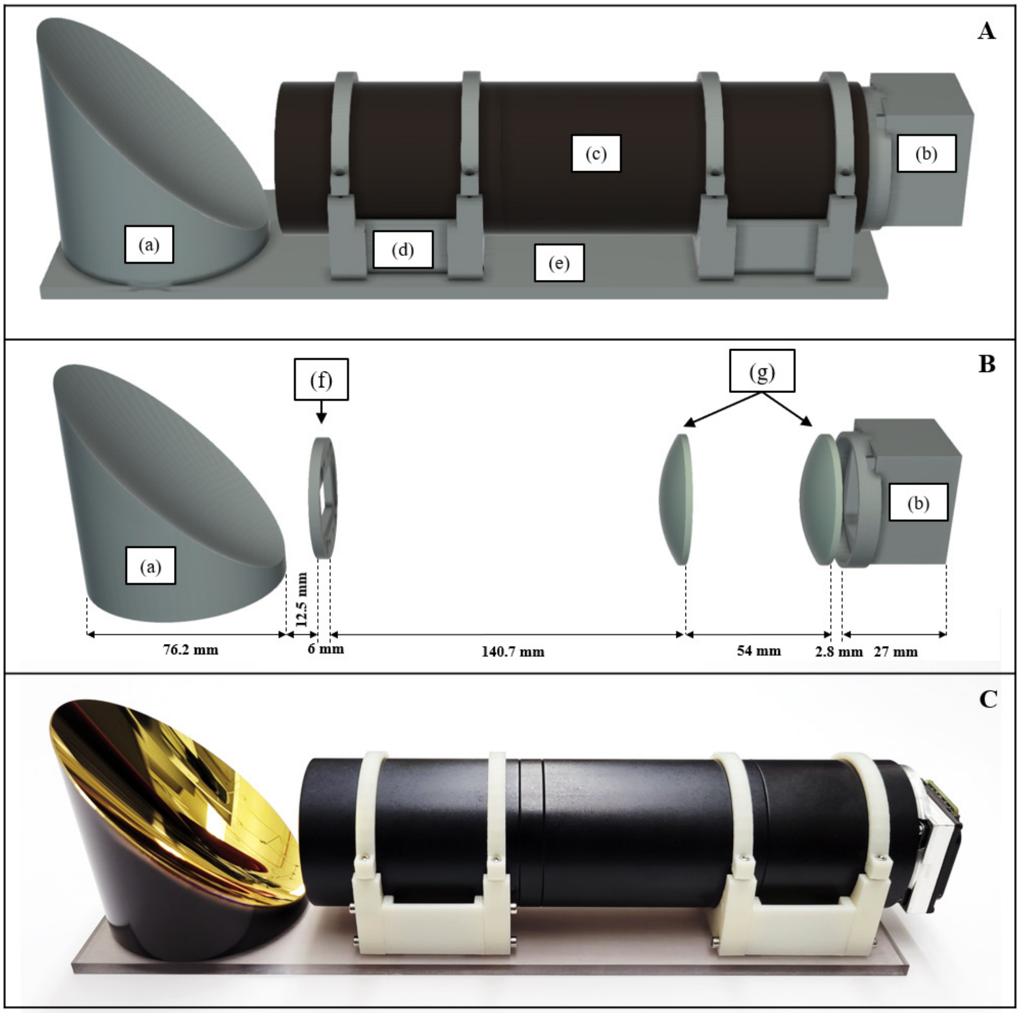

The top panel (A) shows the CAD model of the TIC and mounting system [67]. The mirror (a) is mounted directly to the base plate (e). The TIC assembly (c) with Tamarisk® 640 (b) is installed in two sets of brackets (d), which are bolted to the base plate. The middle panel (B) shows the interior optical components of the TIC and their associated placements [67]. The non-optics components have been omitted. The THz-to-IR custom mount (f) and IR lenses (g) are shown in their respective locations within the TIC. The bottom panel (C) shows the completed TIC with 3-D printed mounts. The mounts will be replaced with machined parts prior to spaceflight.

Figure 41. Terahertz Imaging Camera

Images were taken with the completed TIC following final assembly to demonstrate its functionality. Figure 42 shows two separate one-second timelapses of QCL-generated THz radiation being converted to IR and imaged by the Tamarisk® 640. The QCL was set to 17.5 V, 2000 ns pulse width, and 1 Hz gating. Two setups were employed for imaging, one with the THz-to-IR FPA under vacuum and one without vacuum. The first set of images were captured with the FPA placed in the vacuum chamber at ~10 µTorr. The QCL was set to a 20 kHz pulse repetition frequency for this setup, which corresponds to 37 µW incident power. The second set of images were captured using the spaceflight configuration of the TIC (see Figure 41). Vacuum was not applied because the FPA was installed into the custom FPA mount rather than the vacuum chamber, which was installed in a 2-inch optical tube affixed to the IR section. The QCL was operated at 125 kHz pulse repetition frequency for this setup, which corresponds to 233 µW incident power.

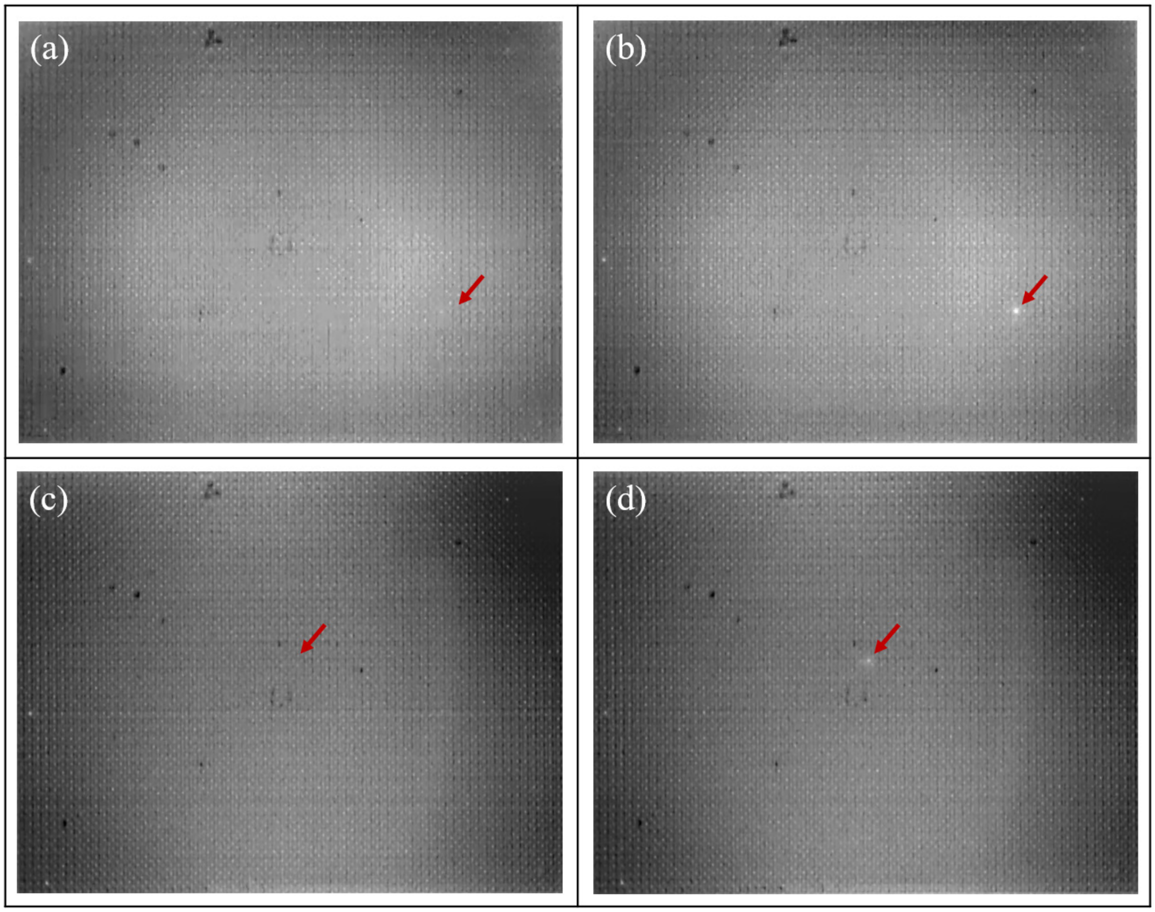

These images show the back of the THz-to-IR FPA during the progression of two separate 1 Hz cycles as terahertz radiation is emitted, focused, converted to infrared radiation, and imaged by the Tamarisk® 640. (a) and (b) correspond to the setup with vacuum applied to the FPA and the QCL operating at 20 kHz modulation. (c) and (d) correspond to the spaceflight configuration with no vacuum applied (due to lack of vacuum capability with the FPA installed in its custom mount) and the QCL operating at 125 kHz modulation. (a) and (c) are images with no incident terahertz. (b) and (d) are images with emissions by the QCL.

Figure 42. One second timelapse of TIC operation, with and without vacuum.

Changes to brightness are visible, a result of the optical element focalization and THz-to-IR FPA effectiveness. The difference in contrast of an illuminated pixel in vacuum at 37 μW was greater than an illuminated pixel in ambient air at 233 μW. The reduction in brightness in the non-vacuum setup was attributed to heat loss due to convection. This effect will be mitigated by the operation of the TIC in low Earth orbit at an altitude of 500 km, which is a near-vacuum environment.

THIS PAGE INTENTIONALLY LEFT BLANK

V. CONCLUSION

Space-based remote sensing of terahertz radiation offers a viable method for imaging various phenomena and activities of interest in the upper ionosphere, situated between 100 and 400 km altitudes. Most relevant for this research are natural phenomena and manmade activities that create (by dissociation of molecular oxygen) or excite electron transitions in atomic oxygen, OI, a naturally occurring constituent of the ionosphere. The subsequent deexcitation of OI from the $^3P_0$ – $^3P_1$ and the $^3P_1$ – $^3P_2$ electron states emit photons at frequencies of 2.06 and 4.75 THz, respectively. With sufficient concentrations of OI, the emitted radiation of these deexcitations can be imaged by space-based imagers sensitive to these frequencies from low Earth orbit. The resulting images can then be transmitted to ground processing stations for subsequent photo-interpretation and analysis.

Researchers at NPS have fabricated MEMs metamaterial focal plane arrays capable of simultaneously converting narrowband radiation centered on 2.06 and 4.75 THz, to longwave infrared radiation capable of being imaged by a COTS LWIR camera. The development of a small form factor, low-cost system becomes feasible with the inclusion of optics to focus ionospheric THz radiation at the THz-to-IR FPA, and separate optics to focus converted IR radiation at the LWIR camera. The objectives of this research were to design, characterize, and construct a space-based optical system that leverages the capabilities of the THz-to-IR FPA and to improve upon previous designs. This research capitalized on previous NPS-developed terahertz imagers and took an iterative approach to improving the performance of the optics. The resulting optical system achieved these objectives. Additionally, the TIC is not limited in future applications to detecting OI line emissions, and can be paired with any metamaterial-based focal plane array of compatible size.

A. METHODOLOGY

To accomplish this objective, the design and development of the optical system were constrained by the requirement to integrate the payload within a 6U CubeSat bus. Therefore, components compatible with this constraint were evaluated for suitability in the overall design. The instrument development comprised two stages. First, the IR section, beginning at the backside of the THz-to-IR FPA and ending at the LWIR camera, was designed, tested, and evaluated. Next, the THz section, starting at the primary aperture and ending at the FPA, was designed, tested, and evaluated. The configurations which exhibited the best performance commensurate with their respective functions were selected for the comprehensive optical system. Preliminary IR optical designs were modeled by the WinLens-3D raytracing software. Five configurations comprising lenses of distinct focal lengths were built and experimentally tested. The factors that determined ultimate selection were focalization, aberration, distortion, and optical path length.

Modeling of the THz section was not accomplished in WinLens-3D due to several limitations of the software and the lack of availability of key geometric characteristics of the candidate lenses. Therefore, THz section characterization was performed experimentally. Four distinct designs were considered for this section: 1) 90°-fold gold-coated parabolic mirror with a copper multi-mesh filter, 2) 90°-fold gold-coated parabolic mirror with a Tsurupica^{TM} window, 3) HDPE lens, and 4) Tsurupica^{TM} lens. A filter was necessary for the mirror designs to prevent infrared radiation from being focused on the THz-to-IR FPA, as the mirror is an efficient broadband reflector. Each design was characterized using a 4.7 THz quantum cascade laser, a pyroelectric detector sensitive to THz radiation, and a FLIR camera for precise thermal response measurements. The pyroelectric detector was used to relate a range of QCL pulse repetition frequencies (5 – 125 kHz) to incident power onto a sensing element of a single pixel of the FPA. The FLIR camera was used to measure the temperature difference due to THz stimulation (ΔT).

B. RESULTS AND ANALYSIS

The final configuration of the imager is a hybrid reflective and refractive design. The results of experimentation, further supported by modeling in WinLens-3D, concluded the optimal IR section design consists of two 50 mm EFL Ge aspheric meniscus lenses to focus the THz-to-IR FPA emitted IR radiation. An additional 1.25x zoom factor was incorporated into the design to allow for dynamic FOV adjustments in imaging the backside of the THz-to-IR FPA. This configuration yielded the best focalization and least aberration and distortion within the given size constraints. Experimental analysis of the THz section determined a 50.8 EFL 90°-fold gold-coated parabolic mirror paired with a copper multi-mesh IR filter is the ideal design. The resulting complete optical system is maintained within the defined constraints and measures 319.2 mm in length, weighing 860 g (mounts and computing hardware not included). The optics demonstrate a field of view of 23.6° by 18.0° with a diffraction limit of 8.37 arcsec for 2.06 THz and 3.63 arcsec for 4.75 THz, as defined by the Rayleigh criterion. By incorporating the THz-to-IR FPA and considering its pixel density (66×50), the achievable resolution of the system is 21.6 arcmin.

The design achieves a thermal response to incident power of 1.0 K/μW, as measured by the FLIR camera. These results are comparable to those achieved by previous experiments conducted by [12] and [48]. Combining the sensitivity of the optical and FPA interface with the 50 mK sensitivity of the Tamarisk® 640 camera (provided by the manufacturer) results in a minimum detectable incident power of 50 nW. This result also agrees with the results in [12], which found that a 46 nW incident power was still observable in imagery captured by the LWIR camera. In their case, the THz-to-IR FPA was optimized for single band detection of 4.7 THz; therefore, it was more sensitive in this particular band than the FPA used in this research.

Direct comparison of the TIC against the instruments presented in Chapter II is not easily achieved due to the profound differences in the detection methods. Most of the reviewed systems employ heterodyne detectors, which require a local oscillator, calibrated blackbody sources, and cryogenic cooling systems. As a result, these tend to be more sensitive detectors. However, imaging is obtained by scanning mechanisms and is not captured in real-time. The complexity and size of these systems translate to costs that are significantly higher compared to the imager presented in this research.

A more direct comparison can be made with the terahertz imager designed for the Mola mission, which shares many similarities. The design principles that governed the Mola design remained largely unchanged during the development of this system. However, due to the increased size and mass budget available for this system, several optical improvements were made that significantly increase its effectiveness. The increased SWaP budget allowed different combinations of optics to be explored, including reflective optics and longer focal length components. The inclusion of reflective optics in the THz section results in approximately 75% and 90% transmission at 2.06 and 4.75 THz, respectively, and is limited by transmittance through the multi-mesh filter. The Mola design achieves approximately 4% transmittance through the thickest part of its 18 mm-thick Tsurupica^{TM} lens at 4.7 THz [48]. This is a result of the 70% transmission per 2 mm of material (see Figure 14). However, transmission increases to approximately 50% towards the edge of the lens as it thins.

Another important difference from the Mola system is the aperture. The Mola system utilizes a 2-inch aperture whereas the system developed in this research utilizes a 3-inch aperture. This is another benefit to the increased size budget. This represents a 225% increase in capture area, and consequently the amount of incoming radiant flux. Finally, the increase in allowable size enabled the use of longer focal length components in the IR section, which dramatically reduces aberration in the LWIR imaging of the backside of the THz-to-IR FPA. The Mola system was severely constrained in its IR section length and the image quality suffers accordingly. The inclusion of 50 mm EFL lenses within the IR section of the current design results in imperceptible aberration/distortion in its imaging. Consequently, the full plane of the THz-to-IR FPA is easily interpretable as a result of the design presented in this research.

C. IMPACT TO THE DEPARTMENT OF DEFENSE

While the TIC was designed to meet the constraints of a 6U CubeSat bus, the current intention is to present this payload to the DOD Space Experiments Review Board (SERB). If selected, the TIC will be integrated into a multi-experiment satellite for orbital deployment. The current TIC design is anticipated to be compatible with the constraints imposed by the new host spacecraft. Spaceflight of this technology will benefit the DOD by providing a novel means of observing and imaging phenomena of interest in the upper atmosphere. According to available open sources, space-based terahertz imaging in support of DOD objectives has not been attempted. Therefore, as part of a larger ongoing project at NPS, the TIC presents a proof-of-concept platform for testing and evaluating the feasibility and effectiveness of employing orbital terahertz imaging systems with the goal of supplementing existing remote sensing architecture. Ultimately, if successful, a network of small satellites carrying this instrument could provide global coverage due to the low cost and compact size of the system.

D. FUTURE WORK

1. Current Iteration

There remain several avenues of research that need to be addressed before the Terahertz Imaging Camera can be integrated into a spacecraft and launched into orbit. First is the development of a suitable imaging processing unit to interface with the Tamarisk® 640 camera. There are currently no methods for extracting the native digital video output of the camera without using the manufacturer's proprietary video cable and third-party video capture software, both of which were unavailable at the time of this research. Instead, the analog video output was used throughout this research, as well as in the Mola mission's application. Future research should investigate a method for extracting the digital video data and a method for transmitting this data via satellite communications datalink.

Additionally, future work should include testing of the entire TIC system in vacuum with an adjacent vacuum chamber pumped with different gaseous mixtures, replicating conditions in the upper ionosphere. This would better characterize the imaging performance against the targets the TIC is designed to capture. Two vacuum chambers, adjoined and separated by a THz transmissive window, could achieve this objective. The TIC would be placed in one chamber and various gaseous mixtures present in the upper ionosphere placed in the other. The measured figures of performance would better inform stakeholders on the effectiveness of the TIC in achieving orbital objectives.

Lastly, environmental testing of the completed system, including mounts and the video interface hardware, need to be completed prior to launch. This should include thermal-vacuum and vibration testing to the standards required by the launch provider. Prior to testing, information about the launch provider and deployment spacecraft must be resolved.

2. Future Iterations

Several avenues of research and development should be pursued to improve the design of the TIC in further iterations. The increase in the allowable size, weight, and power of the TIC from the previous iteration significantly affected the system's performance. Even so, several compromises were made within the design trade-space, primarily with the overall length of the system. These restrictions limited the focal lengths of focusing elements, affecting system performance. This was particularly apparent in the THz section where the thickness of the lenses, a consequence of their short focal lengths, attenuated the incident radiation to such an extent that they were deemed unusable. An increase in size budget would make thinner lenses with longer focal lengths possible, making their use in future designs competitive. An increase in allowable volume would also permit more testing for incorporating a mirror in the IR section.

Additionally, the Tamarisk® 640 was selected as the IR camera primarily because legacy knowledge in translating analogue image data out of the camera into a usable format via the PiCapture and Raspberry Pi computing stack. Future iterations of the TIC should investigate alternative cameras and select the most suitable candidate based on its capabilities and functionality. Finally, work in conjunction with the Sensor Research Lab should continue to identify the most suitable THz-to-IR FPA candidates for future spaceflights. One possible future design would incorporate multiple FPAs for use in a single TIC, potentially through a filter-wheel type design, enabling detection of a variety of wideband and narrowband emissions. This type of design would take full advantage of the optical system's ability to focus wideband THz radiation, as the IR imaging section is not dependent on the absorption frequencies of the THz-to-IR FPA.

LIST OF REFERENCES

[1] R. D. Hunsucker and J. K. Hargreaves, *The High-Latitude Ionosphere and Its Effects on Radio Propagation*. Cambridge, England: Cambridge University Press, 2002.

[2] R. Hermann, "Hypersonic non-equilibrium flow and its thermodynamic relations," University of Alabama Research Institute, Huntsville, AL, USA, UARI Report No. 30, 1965. Available: https://ntrs.nasa.gov/api/citations/19660012369/downloads/19660012369.pdf

[3] National Aeronautics and Space Administration (NASA), "Earth's atmosphere: A multi-layered cake," February 2, 2019. Available: https://climate.nasa.gov/news/2919/earths-atmosphere-a-multi-layered-cake/

[4] T.E. Avery and G.L. Berlin, *Fundamentals of Remote Sensing and Airphoto Interpretation*, 5th Edition. Upper Saddle River, NJ, USA: Prentice Hall, 1992.

[5] Y.S. Lee, *Principles of Terahertz Science and Technology*, New York, NY, USA: Springer, 2009.

[6] National Aeronautics and Space Administration (NASA), "Cosmic Background Explorer." Accessed: September 12, 2023. Available: https://lambda.gsfc.nasa.gov/product/cobe/

[7] R.C. Olsen, *Remote Sensing from Air and Space*, 2nd Edition. Bellingham, WA, USA: Society of Photo-Optical Instrumentation Engineers (SPIE), 2016. Available: https://doi-org.libproxy.nps.edu/10.1117/3.2234477

[8] P.F. Goldsmith, "Modeling collisional excitation of [OI] fine structure line emission from PDRs. I. homogenous clouds," *The Astrophysical Journal*, vol. 887, no. 54. Dec. 2019. Available: https://doi.org/10.3847/1538-4357/ab535e

[9] E. Schlecht *et al*., "Terahertz Limb Sounder to measure winds and temperature above 100 km," in *2015 40th International Conference on Infrared, Millimeter, and Terahertz waves (IRMMW-THz)*. Available: https://ieeexplore.ieee.org/document/7327548

[10] P. Shumyatsky and R.R. Alfano, "Terahertz sources," *Journal of Biomedical Optics*, vol. 16, no. 3. Mar 2011. Available: https://doi.org/10.1117/1.3554742

[11] F. Alves, D. Grbovic, B. Kearney, and G. Karunasiri, "Microelectromechanical systems biomaterial terahertz sensor with integrated metamaterial absorber," *Optical Letters*, vol. 37, no. 11, pp. 1886–1888, 2012. Available: https://doi.org/10.1364/OL.37.001886

[12] F. Alves, L. Pimental, D. Grbovic, and G. Karunasiri, “MEMS terahertz-to-infrared band converter using frequency selective planar metamaterial,” *Scientific Reports*, vol. 8, no. 12466, Aug 2018. Available: https://doi.org/10.1038/s41598-018-30858-z

[13] A. Bhatt, “Development of a wideband THz focal plane array for space applications,” M.S. Thesis, Dept. of Physics, Naval Postgraduate School, Monterey, CA, USA, 2020.

[14] S. Lee, “SiNx/Al metamaterial-based terahertz-to-infrared converter for real-time imaging,” M.S. Thesis, Dept. of Physics, Naval Postgraduate School, Monterey, CA, USA, 2019. Available: https://calhoun.nps.edu/handle/10945/62811

[15] W. Melos-Guimaraes, Title to be determined, Ph.D. Dissertation, Dept. of Physics, Naval Postgraduate School, Monterey, CA, USA, to be published.

[16] W. Melos-Guimaraes, personal communication, Dec. 2023.

[17] Federal Communications Commission (FCC), “Millimeter wave propagation: Spectrum management implications,” Washington, DC, USA, Bulletin no. 70, 1997. Available: https://transition.fcc.gov/Bureaus/Engineering_Technology/Documents/bulletins/oet70/oet70a.pdf

[18] University of Arizona Radio Observatory, “What is submillimeter astronomy,” November 8, 2011. Available: https://aro.as.arizona.edu/~aro/docs/what_is_submillimeter.htm

[19] NASA, Science Mission Directorate, “Infrared waves,” September 2023. Available: https://science.nasa.gov/ems/07_infraredwaves/

[20] G. Schieven, “Observing with ALMA – A primer (Cycle 10),” European Southern Observatory (ESO), Munich, DE, Doc. 10, ver. 1, 2023. Available: https://almascience.nrao.edu/documents-and-tools

[21] Atacama Large Millimeter/Submillimeter Array (ALMA) Observatory, “ALMA factsheet,” April 17, 2011. Available: https://www.almaobservatory.org/en/factsheet/

[22] ALMA, “ALMA basics.” Accessed: Nov. 22, 2023. Available: https://almascience.eso.org/about-alma/alma-basics

[23] C. Belotti *et al*., “The Far-Infrared Radiation Mobile Observation System (FIRMOS) for spectral characterization of the atmospheric emission,” *Atmo. Meas. Tech.*, vol. 16, pp. 1511–2529, May 2008. Available: https://doi.org/10.5194/amt-16-2511-2023

[24] Satellite Evolution, "ESA awards Airbus FORUM Earth monitoring satellite contract, the first far-infrared EO satellite," June 28, 2022. Available: https://www.satelliteevolution.com/post/esa-awards-airbus-forum-earth-monitoring-satellite-contract-the-first-far-infrared-eo-satellite

[25] Palchetti *et al.*, "FIRMOS D8 final report: FIRMOS – technical assistance for a far-infrared radiation mobile observation system (EE9 Forum)," National Research Council, National Institute of Optics, Firenze, Italy, No. 4000123691/18/NL/LF, 2020. Available: https://earth.esa.int/eogateway/documents/20142/37627/FIRMOS-D8-final-report-v3.6.pdf

[26] C. Walker and C. Kulesa, "HEAT: the High Elevation Terahertz Telescope," in *Smithsonian at the Poles*, I. Krupnik, M. Lang, and S. Miller, Eds. Washington, D.C., USA: Smithsonian Institution Press, 2009, pp. 373–379.

[27] U.S. National Science Foundation, "Award abstract #0944335. High Elevation Antarctic Terahertz (HEAT) telescopes for Dome A and Ridge A," Jul. 20, 2013. Available: https://www.nsf.gov/awardsearch/showAward?AWD_ID=0944335&HistoricalAwards=false

[28] U.S. National Science Foundation, "Award abstract #1410896. Continuing operation of the High Elevation Antarctic Terahertz telescope at Ridge A, Antarctica," Jul. 19, 2014. Available: https://www.nsf.gov/awardsearch/showAward?AWD_ID=1410896&HistoricalAwards=false

[29] The University of Arizona, "The High Elevation Terahertz telescope. Instrumentation overview," 2013. Available: http://soral.as.arizona.edu/HEAT/instrument

[30] The University of Arizona, "The High Elevation Terahertz telescope. Current data release: DR4," 2013. Available: http://soral.as.arizona.edu/HEAT/data/index.html#squaremaps

[31] *Observer's handbook for cycle 10*, NASA/IPAC Infrared Science Archive (IRSA), Pasadena, CA, USA, 2022. Available: https://irsa.ipac.caltech.edu/data/SOFIA/docs/proposing-observing/proposal-documents/index.html

[32] NASA Office of Inspector General, "NASA's management of the Stratospheric Observatory For Infrared Astronomy program," Washington, D.C., USA, IG Report No. IG-20-022, 2020.

[33] NASA, "SOFIA," February 12, 2024. Available: https://science.nasa.gov/mission/sofia

[34] S. Heyminck, U. U. Graf, R. Gusten, J. Stutzki, H. W. Hubers, and P. Hartogh, "GREAT: the SOFIA high-frequency heterodyne instrument," *Astronomy & Astrophysics*, vol. 542, no. L1, May 2012. Available: https://doi.org/10.1051/0004-6361/201218811

[35] C. Risacher *et al.*, "The upGREAT dual frequency heterodyne arrays for SOFIA," Journal of Astronomical *Instrumentation*, vol. 7, no. 4, Dec. 2018. Available: https://doi.org/10.1142/S2251171718400147

[36] H. Richter *et al.*, "Direct measurements of atomic oxygen in the mesosphere and lower thermosphere using terahertz heterodyne spectroscopy," *Communications Earth & Environment*, vol. 2, no. 19, Jan. 2021. Available: https://doi.org/10.1038/s43247-020-00084-5

[37] C. Walker *et al.*, "Gal/Xgal U/ULDB Spectroscopic/Stratospheric THz Observatory: GUSTO," presented at *SPIE Astronomical Telescopes and Instrumentation*, Quebec, Canada, Aug. 31, 2022. Available: https://doi.org/10.1117/12.2629051

[38] E. Landau, "NASA's GUSTO prepares to map space between the stars," NASA, December 18, 2023. Available: https://science.nasa.gov/missions/scientific-balloons/nasas-gusto-prepares-to-map-space-between-the-stars

[39] C. Walker, C. Kulesa, M. Reinhart, R. Fitzgerald, H. Bailey, and D. Dolana, "Galactic/Extragalactic ULDB Spectroscopic-Stratospheric Terahertz Observatory (GUSTO) project update," NASA. Accessed: Nov. 24, 2023. Available: https://smd-cms.nasa.gov/wp-content/uploads/2023/04/Walker_GUSTO_APAC_no_video_TAGGED.pdf

[40] J. R. Wertz, D. F. Everett, and J.J. Puschell, *Space Mission Engineering: The New SMAD*. Torrance, CA, USA: Microcosm Press, 2011.

[41] K.U. Grossmann, M. Kaufmann, and E. Gerstner, "A global measurement of lower thermosphere atomic oxygen densities," *Geophysical Research Letters*, vol. 27, no. 9, pp. 1387–1390, May 2000. Available: https://doi.org/10.1029/2000GL003761

[42] European Space Agency (ESA) Earth Observation Portal (eoPortal), "Shuttle flight STS-85," June 14, 2012. Available: https://www.eoportal.org/satellite-missions/shuttle-flight-sts-85#crista-spas-2-free-flyer-platform

[43] K.U. Grossmann, D. Offermann, O. Gusev, J. Oberheide, M. Riese, and R. Spang, "The CRISTA-2 mission," *Journal of Geophysical Research*, vol. 107, no. D23, Oct. 2002. Available: https://doi.org/10.1029/2001JD000667

[44] D. Offermann, K.U. Grossmann, P. Barthol, P. Knieling, M. Riese, and R. Trant, "Cryogenic Infrared Spectrometers and Telescopes for the Atmosphere (CRISTA) experiment and middle atmosphere variability," *Journal of Geophysical Research*, vol. 104, no. D13, pp. 16,311–16,325, Jul 1999. Available: https://doi.org/10.1029/1998JD100047

[45] G.H. Grimshaw, *Supporting Shuttle: 35+ years of excellence at Dryden*, Washington, DC, USA: NASA, 2012. Available: https://www.nasa.gov/wp-content/uploads/2021/04/supporting_shuttle_dryden.pdf

[46] L. Palchetti et al., "FORUM: Unique far-infrared satellite observations to better understand how Earth radiates energy to space," *American Meteorological Society*, vol. 101, no. 12, pp. E2030–E2046, Dec. 2020. Available: https://doi.org/10.1175/BAMS-D-19-0322.1

[47] G. Bianchini, F. Castagnoli, G. Di Natale, and L. Palchetti, "A Fourier transform spectroradiometer for ground-based remote sensing of the atmosphere downwelling long-wave radiance," *Atmospheric Measurement Techniques*, vol. 12, no. 1, pp. 619–635, Jan. 2019. Available: https://doi.org/10.5194/amt-12-619-2019

[48] C. Brave, "Development of a terahertz imaging CubeSat," M.S. Thesis, Dept. of Physics, Naval Postgraduate School, Monterey, CA, USA, 2021.

[49] W. Lan, "TIC intro," presented at Naval Postgraduate School, Monterey, CA, USA, Jan. 9, 2024.

[50] Broadband, Inc., "Tsurupica THz Optics." Accessed: Dec. 1, 2023. Available: http://www.bblaser.com/bbl_item/bbli003_thz_lens.html

[51] Microtech Instruments, Inc., "THz lenses & windows," August 1, 2021. Available: https://mtinstruments.com/index.php?main_page=product_info&cPath=3&products_id=11

[52] M. Naftaly and R. Dudley, "Terahertz reflectivities of metal-coated mirrors," *Applied Optics*, vol. 50, no. 19, pp. 3201–3204, Jul. 2011. Available: https://doi.org/10.1364/AO.50.003201

[53] Edmund Optics Inc., "Gold off-axis parabolic mirrors." Accessed: May 5, 2023. Available: https://www.edmundoptics.com/f/gold-off-axis-parabolic-mirrors/39489/

[54] The CubeSat Program Cal Poly (SLO), *CubeSat Design Specification*, Rev. 14.1, San Luis Obispo, CA, USA, 2022. Available: https://www.cubesat.org/cubesatinfo

[55] QMC Instruments Ltd., “Multimesh filters.” Accessed: Feb. 21, 2024. Available: https://www.qmcinstruments.co.uk/multi-mesh-filters

[56] Edmund Optics Inc., “50mm dia x 50mm FL 3–12µm coated, Ge aspheric lens.” Accessed: May 5, 2023. Available: https://www.edmundoptics.com/p/50mm-dia-x-50mm-fl-3-12mum-coated-ge-aspheric-lens/32077/

[57] Edmund Optics Inc., “The correct material for infrared (IR) applications.” Accessed: May 5, 2023. Available: https://www.edmundoptics.com/knowledge-center/application-notes/optics/the-correct-material-for-infrared-applications/

[58] J. E. Greivenkamp, *Field Guide to Geometric Optics*, The Society of Photo-Optical Engineers (SPIE), Bellingham, WA, USA, 2004. Available: https://spie.org/Publications/Book/547461?&origin_id=x647&start_at=49#_=_

[59] Leonardo DRS, *Tamarisk thermal camera cores*. 2012. Available: https://www.leonardodrs.com/wp-content/uploads/2023/08/Tamariskfamily_datasheet_mr-2013-01-654_rev14.pdf

[60] DRS Technologies, *Tamarisk 640 17µm 640x480 Long Wave Infrared Camera: Camera Control Software User Guide*, Rev. B, DRS Technologies, Inc., Dallas, TX, USA, 2013.

[61] LINOS Photonics GmbH, *WinLens Optical Design Software*, LINOS Photonics GmbH, Gottingen, Germany, 2002.

[62] The CubeSat Program Cal Poly San Luis Obispo (SLO), “The CubeSat program.” Accessed Jan. 3, 2024. Available: https://www.cubesat.org/about

[63] B. Cooper, “Corvus-6 spacecraft platform,” Astro Digital, Santa Clara, CA, USA, 120 10485 001, 2019. Available: https://astrodigital.com/current-missions

[64] W. Lan, private communications, Feb. 2023.

[65] H. English, “Concept of operations, software development, and flight integration testing for a THz imaging camera payload,” M.S. Thesis, Space Systems Academic Group, Naval Postgraduate School, Monterey, CA, USA, 2020. Available: NPS Restricted Collection

[66] Pyroelectric Detectors for THz-Radiation, SLT Sensor- und Lasertechnik GmbH. Wildau, Germany, 2016.

[67] R.E. Gobrecht, computer aided design model, Feb. 2024.

INITIAL DISTRIBUTION LIST

1. Defense Technical Information Center
   Fort Belvoir, Virginia

2. Dudley Knox Library
   Naval Postgraduate School
   Monterey, California